AD-A275 443

REPORT DOCUMENTATION PAGE

1. AGENCY USE ONLY (Leave blank)	2. REPORT DATE 12/16/93	3. REPORT TYPE AND DATES COVERED Final / May 90 - 31 Oct 93 (2)

4. TITLE AND SUBTITLE

Carrier Collection and Scattering in Quantum Well and Superlattice Devices

5. FUNDING NUMBERS

DAAL03-90-G-0118

6. AUTHOR(S)

Robert M. Kolbas

7. PERFORMING ORGANIZATION NAME(S) AND ADDRESS(ES)

North Carolina State University
Dr. William L. Klarman, Vice Chancellor
103 Holladay Hall
Raleigh, NC 27695-7003

8. PERFORMING ORGANIZATION REPORT NUMBER

9. SPONSORING / MONITORING AGENCY NAME(S) AND ADDRESS(ES)

U.S. Army Research Office
P. O. Box 12211
Research Triangle Park, NC 27709-2211

10. SPONSORING / MONITORING AGENCY REPORT NUMBER

ARO 28070.1-EL-SDI

11. SUPPLEMENTARY NOTES

12a. DISTRIBUTION / AVAILABILITY STATEMENT

Approved for public release; distribution unlimited.

12b. DISTRIBUTION CODE

DTIC
ELECTE
FEB 0 8 1994
S A

13. ABSTRACT (Maximum 200 words)

The objective of this experimental program is to define the regimes in which scattering and carrier collection dominate the performance of quantum well and superlattice devices. The program consists of five thrusts: 1) materials growth; 2) carrier collection experiments; 3) utilization of ultra-thin monolayer thick quantum wells; 4) the undertanding, control and utilization of dissipative mechanisms for new device concepts, and; 5) the demonstration of devices. The results obtained are applicable to monolithic photonic devices and high speed optical interconnect technology. A new device called a Bias Induced Color-Tuned Emitter (BICE) based on the selective collection of carriers in a quantum well was demonstrated for the first time.

94 2 07 122

94-04268

14. SUBJECT TERMS

Electronic Devices, Optoelectronic Devices, Semiconductor Lasers, Quantum Wells, Optical Interconnects

16. PRICE CODE

17. SECURITY CLASSIFICATION OF REPORT UNCLASSIFIED	18. SECURITY CLASSIFICATION OF THIS PAGE UNCLASSIFIED	19. SECURITY CLASSIFICATION OF ABSTRACT UNCLASSIFIED	20. LIMITATION OF ABSTRACT UL

GENERAL INSTRUCTIONS FOR COMPLETING SF 298

The Report Documentation Page (RDP) is used in announcing and cataloging reports. It is important that this information be consistent with the rest of the report, particularly the cover and title page. Instructions for filling in each block of the form follow. It is important to *stay within the lines* to meet *optical scanning requirements*.

Block 1. Agency Use Only *(Leave blank)*.

Block 2. Report Date. Full publication date including day, month, and year, if available (e.g. 1 Jan 88). Must cite at least the year.

Block 3. Type of Report and Dates Covered. State whether report is interim, final, etc. If applicable, enter inclusive report dates (e.g. 10 Jun 87 - 30 Jun 88).

Block 4. Title and Subtitle. A title is taken from the part of the report that provides the most meaningful and complete information. When a report is prepared in more than one volume, repeat the primary title, add volume number, and include subtitle for the specific volume. On classified documents enter the title classification in parentheses.

Block 5. Funding Numbers. To include contract and grant numbers; may include program element number(s), project number(s), task number(s), and work unit number(s). Use the following labels:

C	- Contract	PR	- Project
G	- Grant	TA	- Task
PE	- Program Element	WU	- Work Unit Accession No.

Block 6. Author(s). Name(s) of person(s) responsible for writing the report, performing the research, or credited with the content of the report. If editor or compiler, this should follow the name(s).

Block 7. Performing Organization Name(s) and Address(es). Self-explanatory.

Block 8. Performing Organization Report Number. Enter the unique alphanumeric report number(s) assigned by the organization performing the report.

Block 9. Sponsoring/Monitoring Agency Name(s) and Address(es). Self-explanatory.

Block 10. Sponsoring/Monitoring Agency Report Number. *(If known)*

Block 11. Supplementary Notes. Enter information not included elsewhere such as: Prepared in cooperation with...; Trans. of...; To be published in.... When a report is revised, include a statement whether the new report supersedes or supplements the older report.

Block 12a. Distribution/Availability Statement. Denotes public availability or limitations. Cite any availability to the public. Enter additional limitations or special markings in all capitals (e.g. NOFORN, REL, ITAR).

DOD - See DoDD 5230.24, "Distribution Statements on Technical Documents."
DOE - See authorities.
NASA - See Handbook NHB 2200.2.
NTIS - Leave blank.

Block 12b. Distribution Code.

DOD - Leave blank.
DOE - Enter DOE distribution categories from the Standard Distribution for Unclassified Scientific and Technical Reports.
NASA - Leave blank.
NTIS - Leave blan'.

Block 13. Abstract. Include a brief *(Maximum 200 words)* factual summary of the most significant information contained in the report.

Block 14. Subject Terms. Keywords or phrases identifying major subjects in the report.

Block 15. Number of Pages. Enter the total number of pages.

Block 16. Price Code. Enter appropriate price code *(NTIS only)*.

Blocks 17. - 19. Security Classifications. Self-explanatory. Enter U.S. Security Classification in accordance with U.S. Security Regulations (i.e., UNCLASSIFIED). If form contains classified information, stamp classification on the top and bottom of the page.

Block 20. Limitation of Abstract. This block must be completed to assign a limitation to the abstract. Enter either UL (unlimited) or SAR (same as report). An entry in this block is necessary if the abstract is to be limited. If blank, the abstract is assumed to be unlimited.

A Final Report

To

THE ARMY RESEARCH OFFICE

CARRIER COLLECTION and SCATTERING
in
QUANTUM WELL and SUPERLATTICE DEVICES

Author: Robert M. Kolbas, Professor
December 1993

Robert M. Kolba

Robert M. Kolbas
Professor
(919) 515-5257
FAX: (919) 515-3027
SSN: 068-40-0875

Accesion For	
NTIS CRA&I	☑
DTIC TAB	☐
Unannounced	☐
Justification	
By	
Distribution /	
Availability Codes	
Dist	Avail and / or Special
A-1	

Department of Electrical and Computer Engineering
North Carolina State University
Raleigh, North Carolina 27695-7911

TABLE OF CONTENTS

Carrier Collection and Scattering in Quantum Well and Superlattice Devices: DAAL-03-90-G-0118
Robert M. Kolbas, North Carolina State University   (919) 515-5257   (FAX): 515-3027
email:kolbas@eos.ncsu.edu

Section 1: STATEMENT OF THE PROBLEM

The objective of this experimental program was to define the regimes in which scattering and carrier collection dominate the performance of quantum well and superlattice devices. The program consisted of five thrusts: 1) materials growth; 2) carrier collection experiments; 3) utilization of ultra thin monolayer thick quantum wells; 4) the understanding, control and utilization of dissipative mechanisms for new device concepts, and; 5) the demonstration of devices based on the concepts suggested by the results of thrusts 2,3, and 4.

Quantum well and superlattice devices are high payoff solutions to future high speed computer and communication systems. Knowledge and control of semiconductor heterojunctions are key to realizing the potential of advanced semiconductor devices and designing new structures. Heterojunctions are already a fundamental part of discrete electronic and optoelectronic components. They will become a necessity to realize monolithic photonic devices that combine electronic and optoelectronic components. These interfaces will address the high speed optical interconnect technology needed for distributed/parallel computing and the special functions needed to break the electrical-optical-electrical barrier that has prevented optical and electrical processing from achieving their full potential.

Section 2: SUMMARY OF THE MOST IMPORTANT RESULTS

in viewgraph form
(see next page)

MAJOR ACCOMPLISHMENTS
Carrier Collection and Scattering in
Quantum Well and Superlattice Devices
DAAL-03-90-G-0118

The most important accomplishments of this program and their relevance to the SDIO/IST goals are:

1) Demonstrated a vertical cavity surface emitting laser with a submonolayer thick InAs active region.

- Thinnest active region (3.25Å) to support stimulated emission even though the optical feedback was perpendicular to the plane of the gain region.
- Explained this unexpected result based on the spreading out of the electron and hole wave functions.

Relevance to SDIO/IST mission: Carrier confinement, current confinement and current confinement were already known to be important design parameters for low threshold high performance lasers. We have shown that carrier collection and the size of the wave functions are equally important design parameters for thin (<100Å) quantum based devices. These newly recognized design parameters must be considered to correctly design quantum well and mesoscopic devices. This work provides a concrete analytical basis to explain many of the empirical trends observed but not explained in the semiconductor laser literature.

2) Demonstrated a Bias Induced Color-tuned Emitter (BICE):

- First demonstration of a voltage controlled dual- (or multi-) wavelength semiconductor light emitter based on the preferential collection of electrons and holes.
- Wavelength was shifted 500Å with the application of low bias voltages (<5 volts)
- Device operation demonstrated at 77K and at room temperature.
- Growth and fabrication are relatively simple. Integration with GaAs based electronics should be possible.
- Selective carrier collection has other important photonic applications.
- **Note that BICE operates on a fundamentally different principle than Self Electro-optic Effect Devices (SEED).**

Relevance to SDI/IST mission: High speed optical sources that can be integrated with electronics are needed for optical interconnects and as interfaces with optical processors. Wavelength division multiplexing can be used to take advantage of the huge bandwidth afforded by fiber optic or free space communication. BICE is a new and easy to fabricate approach to wavelength division multiplexing. Selective carrier collection could also be used to develop semiconductor lasers that are tunable over a broad range of wavelengths. (See Appendix A and related figures.)

3) Phonon assisted stimulated emission:

- First confirming observation of phonon assisted stimulated emission (DAAL-03-87-K-0051)
- Demonstrated the thinnest quantum well to exhibit phonon assisted stimulated emission.
- First time resolved data of phonon assisted stimulated emission.

Relevance to SDI/IST mission: Phonons play an important role in thermalizing injected carriers in laser diodes and are often the limiting factor in high speed electronic devices. With respect to laser diodes we have the opportunity to harness the phonons rather than having them work against us as they do in existing devices. Also, Holonyak and co-workers have suggested that phonon assisted stimulated emission may involve stimulated phonon emission. If so, this would open up an entirely new class of electron-photon-phonon interactions in condensed matter.

4) Other accomplishments:

- Tutorial paper on the density of states function that explains many missing steps and clears up many misconceptions about quantum wells.
- Improved laser thresholds by reducing surface and bulk leakage currents.
- Reduced laser threshold in strained layer lasers by heavy silicon doping.
- Enhanced/suppressed intermixing of quantum wells for low loss waveguide applications.
- Optical matrix elements and the dielectric constant of partially intermixed quantum wells.

Relevance to SDI/IST mission: All of these accomplishment are consistent with the mission of high performance high density optoelectronic circuits. This work represents the discovery and application of new phenomena in practical device structures.

Carrier Collection and Scattering in Quantum Well and Superlattice Devices: DAAL-03-90-G-0118
Robert M. Kolbas, North Carolina State University (919) 515-5257 (FAX): 515-3027
email:kolbas@eos.ncsu.edu

Accomplishments that involved joint funding:

5) Low temperature (Al)GaAs for three dimensional Integrated Optoelectronic Circuits (Joint funding with the NSF center for Advanced Electronic Material Processing at NCSU.):

• At NCSU three important advances have been made using low temperature (LT) GaAs and AlGaAs. We have used LT (Al)GaAs as a surface passivation layer to double the breakdown voltage of GaAs (MESFET) transistors without sacrificing the (transconductance) or other device characteristics. Second, we have demonstrated that is possible to grow laser quality epitaxial layers on top of LT GaAs. Finally, we have demonstrated that it is possible to make LT GaAs conductive by the diffusion of Zn, opening the possibility of producing electrical interconnects through LT GaAs layers without having to etch via holes.

Relevance to SDI/IST mission: All three of these results have important implications to the development of three dimensional integrated optoelectronic circuits. Simply put LT GaAs could be the glue that finally allows us to 'stick together and stack on top' electrical and optical components on a single semiconductor substrate in a controlled and reproducible fashion. This should make it possible to produce multilevel (3 dimensional integration) integrated optoelectronic circuits that

would be a major advance in meeting the demands required for high speed optical interconnects (multi-processor computers) and reconfigurable parallel processing architecture.

Accomplishments that involved collaborative efforts:

6) Light emission from silicon nanoparticles: (Dr. Kingon's group grew the nanoparticles by gas phase synthesis with support from DAAL 03-89-K-0131.)

- Visible light emission from silicon nanoparticles (1-10nm in diameter) at room temperature. Radiative lifetime measured to be 1-2 ns at 77K and room temperature.
- Removal of hydrogen improves the luminescence (rather than killing it as reported for porous silicon).
- Addition of oxygen has little effect on the luminescence even when x-ray analysis indicates that the particles are amorphous.

Relevance to SDI/IST mission: It is necessary to understand origin of visible light emission from silicon to determine if the technology has potential for future applications. This will be very important for monolithic integrated optoelectronic circuits and high speed optical interconnects.

Section 3: PUBLICATIONS
DAAL 03-90-G-0018 PUBLICATIONS

"Visible Light Emission from Silicon and Oxygen-Doped Silicon Nanoparticles," D. Zhang, R. M.. Kolbas, P. D.. Milewski, P. Mehta, D. J.. Lichtenwalner and A.I. Kingon, accepted at the 1993 Electronic Materials Conference. Also, accepted for publication in the J. Electronic Materials.

"Two Terminal Bias Induced Dual Wavelength Semiconductor Light Emitter," D. Zhang, F. E. Reed, T. Zhang, N. V. Edwards and R. M. Kolbas, Appl. Phys. Lett. 63, No. 23, pp. (13 Dec 1993). to be published

"Vertical Cavity Surface Emitting Laser with a Submonolayer Thick InAs Active Layer," S. D. Benjamin, T. Zhang, Y. L. Hwang, M. S. Mytych and R. M. Kolbas, Appl. Phys. Lett. 60, No. 15, pp. 1800-1802 (13 April 1992).

"Time Resolved and Phonon Assisted Stimulated Emission in AlGaAs-GaAs Quantum Wells," S. D. Benjamin, J. H. Lee, Y. L. Hwang, T. Zhang and R. M. Kolbas, Appl. Phys. Lett. 59, No. 3, pp. 351-353 (15 July 1991).

"Visible Light Emission from Silicon Nanoparticles," D. Zhang, R. M. Kolbas, P. Mehta, A. K. Singh, D. J. Lichtenwalner, K. Y. Hsieh and A. I. Kingon, Materials Research Society, Fall Meeting, Dec. 2-6, 1991, Boston MA; "Light Emission from Silicon," Editors, S. S. Iyer, L. T. Canham and R. T. Collins (Proceedings of Materials Research Society, Pittsburgh, PA, 1991).

"A General Derivation of the Density of States Function for Quantum Wells and Superlattices," M. W. Prairie and R. M. Kolbas, Superlattices and Microstructures Vol. 7, No. 4, pp. 269-277 (1990).

"Surface and Bulk Leakage Currents in Transverse Junction Stripe Lasers," Y. K. Sin, K. Y. Hsieh, J. H. Lee and R. M. Kolbas, J. Appl. Phys. 69, pp. 1081-1090 (Jan. 1991).

"InGaAs-GaAs-AlGaAs Strained-Layer Lasers with Heavy Silicon Doping," Y. K. Sin, K. Y. Hsieh, J. H. Lee, Y. Hwang and R. M. Kolbas, J. Appl. Phys. 70, No. 2, pp. 568-573 (15 July 1991).

Carrier Collection and Scattering in Quantum Well and Superlattice Devices: DAAL-03-90-G-0118
Robert M. Kolbas, North Carolina State University (919) 515-5257 (FAX): 515-3027
email:kolbas@eos.ncsu.edu

"Enhanced/Suppressed Interdiffusion of Lattice Matched and Pseudomorphic III-V Heterostructures by Controlling Ga Vacancies," R. M. Kolbas, Y. L. Hwang, T. Zhang, M. W. Prairie, K. Y. Hsieh and U. K. Mishra, presented at the International Workshop on Multiple Quantum Well Mixing, September 1990; also, published in Optical and Quantum Electronics 24, pp. S805-S812 (1991).

"Enhanced/Suppressed Interdiffusion of InGaAs-GaAs-AlGaAs Strained Layers by Controlling Impurities and Gallium Vacancies, "K. Y. Hsieh, Y. L. Hwang, J. H. Lee, and R. M. Kolbas, presented at the 1989 Electronic Materials Conference. Published J. Electronic Materials Vol. 19, No. 12, pp. 1417-1423 (1990).

"Diffusion of Zinc into GaAs Layers Grown by Molecular Beam Epitaxy at Low Substrate Temperatures," Y. K. Sin, Y. L. Hwang, T. Zhang and R. M. Kolbas, J. of Electronic Materials, Vol. 20, No. 6, pp. 465-469 (1991).

"Monolayer Thick GaSbAs-GaAs Strained Layer Quantum Well Lasers," J. H. Lee, T. Zhang and R. M. Kolbas, presented at Conference on Lasers and Electro-Optics, Baltimore (May 1991); also published in the Technical Digest Series, Vol. 10, pp. 334-335.

"Optical Matrix Elements and the Dielectric Constant of Partially Intermixed Quantum Wells," M. W. Prairie and R. M. Kolbas, accepted with revisions, J. Appl. Physics.

"Effects of a Low Temperature GaAs Buffer Layer on the Interdiffusion of GaAs/AlGaAs Heterostructures During Thermal Annealing," presented at the 6th Conference on Semi-insulating III-V Materials, Toronto, May 13-16, 1990; also published in the proceedings of the 6th Conference on Semi-insulating III-V Materials.

"The Elimination of Carrier Compensation Caused by a Low Temperature MBE Grown GaAs Surface Layer in a GaAs MESFET Structure," Y. L. W. L. Yin, J. H. Lee, T. Zhang, R. M.. Kolbas and U. K. Mishra, presented at the 1990 Electronic Materials Conference.

"Improved Breakdown Voltage in GaAs MESFET's Utilizing Surface Layers of GaAs Grown at a Low Temperature by MBE," L. W. Yin, Y.

Hwang, J. H. Lee, R. M. Kolbas, R. J. Trew, and U. K. Mishra, Electron Device Letters 11, No. 12, pp. 561-563 (Dec. 1990).

"Evaluation of LT GaAs for High Speed Electronic and Analog Optoelectronic Applications," U. K. Mishra and R. M. Kolbas, Materials Research Society, Fall Meeting Dec. 2-6, 1991, Boston MA; "Low Temperature (LT) GaAs and Related Materials", Editors G. L. Witt, R. Calawa, U. Mishra and E. Weber (Proceedings of Materials Research Society, Pittsburgh, PA, 1991).

"Laser Quality AlGaAs-GaAs Quantum Wells Grown on Low Temperature GaAs," Y. Hwang, D. Zhang, T. Zhang, M. Mytych and R. M. Kolbas, Materials Research Society, Fall Meeting Dec. 2-6, 1991, Boston MA; "Low Temperature (LT) GaAs and Related Materials" Editors G. L. Witt, R. Calawa, U. Mishra and E. Weber (Proceedings of Material Research Society, Pittsburgh, PA, 1991).

"Dose Effects in Si FIB-Mixing of Short Period AlGaAs/GaAs Superlattices," A. J. Steckel, P. Chen, A. Choo, H. Jackson, J. T. Boyd, P. P. Pronko, A. Ezis and R. M. Kolbas, Materials Research Society, Fall Meeting Dec. 2-6, 1991, Boston, MA; "Advanced II-V Compound Semiconductor Growth, Processing and Devices," Editors S. J. Pearton, J. M. Zavada and D. K. Sadana, (Proceedings of Material Research Society, Pittsburgh, PA 1991).

"Optoelectronic Properties of GaN, AlGaN, and AlGaN-GaN Quantum Well Heterostructures," R. M. Kolbas and S. Krishnankutty, LEOS 1993 Summer Topical Meeting Digest on Visible Semiconductor Lasers, July 21-22, 1993, Santa Barbara, CA (IEEE Catalog Number 93TH0549-6, Library of Congress Number 93-77778).

"Monolithically Integrated SQW Laser and HBT Laser Driver Via Selective OMVPE Regrowth," D. B. Slater, Jr., P. M. Enquist, J. A. Hutchby, F. E. Reed, A. S. Morris, R. M. Kolbas, R. J. Trew, A. S. Lujan and J. W. Swart, Photonics Technology Letters 5, No. 7, pp. 791-794 (7 July 1993).

"Optical Absorption and Stimulated Emission from Monolayer Thick Single Quantum Wells," D. Zhang and R. M. Kolbas, to be submitted to the J. Appl. Physics.

DAAL 03-87-K-0051 PUBLICATIONS

"Stimulated Visible Light Emission from Ultra-thin GaAs Single and Multiple Quantum Wells Sandwiched Between Indirect Gap $Al_{0.49}Ga_{0.51}As$ Confining Layers," J. H. Lee, K. Y. Hsieh, Y. L. Hwang and R. M. Kolbas, Appl. Phys. Lett. 56, No. 20, pp. 1998-2000 (14 May 1990).

"Photoluminescence and Stimulated Emission from Monolayer Thick Pseudomorphic InAs Single Quantum Well Heterostructures," J. H. Lee, K. Y. Hsieh and R. M. Kolbas, Phys. Rev. B. 41, pp. 7678-7684 (15 April 1990).

"Stimulated Emission from Monolayer Thick $Al_xGa_{1-x}As$-GaAs Single Quantum Well Heterostructures," J. H. Lee, K. Y. Hsieh, Y. L. Hwang and R. M. Kolbas, Appl. Phys. Lett. 56, No. 7, pp. 626-628 (12 Feb. 1990).

"Stimulated Emission in Ultra-thin (20Å) $Al_xGa_{1-x}As$-GaAs Single Quantum Well Heterostructures," Y. C. Lo, K. Y. Hsieh, and R. M. Kolbas, Appl. Phys. Lett. 52, pp. 1853-1855 (30 May 1988).

"Phonon Assisted Stimulated Emission in Thin (<55Å) AlGaAs-GaAs-AlGaAs Single Quantum Wells," Y. C. Lo and R. M. Kolbas, Appl. Phys. Lett. 53, pp. 2266-2268 (5 Dec. 1988).

"Carrier Recombination Dynamics in Thin InGaAs-GaAs Single Quantum Well Heterostructures," S. D. Benjamin, N. G. Anderson, and R. M. Kolbas, Quantum Electronics and Laser Science Conference 1989 Technical Digest Series Vol. 12, 84 (1989).

"Laser Properties and Carrier Collection in Ultra-thin Quantum Well Heterostructures," R. M. Kolbas, Y. C. Lo, and J. H. Lee, IEEE Journal Quantum Electronics 26, pp. 25-31 (Jan. 1990).

"Time Resolved Phonon Assisted Stimulated Emission in Quantum Well Heterostructures," 1989 Device Research Conference, IEEE Trans. Electron Devices 36, No. 11, p. 2613 (Nov. 1989).

"Stimulated Emission from Monolayer Thick Quantum Well Heterostructures," J. H. Lee, K. Y. Hsieh, and R. M. Kolbas, 1989 Device Research Conference, IEEE Transactions of Electron Devices 36, No. 11, p. 2613 (Nov. 1989).

"Effects of a Low Temperature GaAs Buffer Layer on the Interdiffusion of GaAs/AlGaAs Heterostructures During Thermal Annealing," presented at the 6th Conference on Semi-insulating III-V Materials, Toronto, May 13-16, 1990; also published in the proceedings of the 6th Conference on Semi-insulating III-V Materials pp. 77-82 (1990).

Publications that got out the door while waiting for a contract number:

"High Efficiency Carrier Collection and Stimulated Emission in Thin (50Å) Pseudomorphic InGaAs Quantum Wells," N. G. Anderson, Y. C. Lo and R. M. Kolbas, Appl. Phys. Lett. 49, 758 (1986).

"Stimulated Emission from Ultra-thin (6.6Å) InAs/GaAs Quantum Well Heterostructures Grown by Atomic Layer Epitaxy," Appl. Phys. Lett. 50, 1266 (1987).

"Negative Differential Resistance in a Strained Layer Quantum Well Structure with a Bound State," G. S. Lee, K. Y. Hsieh, and R. M. Kolbas, J. Appl. Phys. 62, 3453 (1987).

Section 4: PERSONNEL SUPPORTED and DEGREES GRANTED

PERSONNEL	POSITION	DEGREE EARNED
Robert M. Kolbas	Principal Investigator	
Dahua Zhang	Research Assistant	MS June 1990, Ph. D. Dec. 1993
Rick Reed *	Research Assistant	
Will Rowland	Research Assistant	MS June 1993
Mark Mytych *	Research Assistant	MS June 1992
Nora V. Edwards *	Research Assistant	MS June 1993
Jay Sun	Research Assistant	transferred to Cal Tec
David Benjamin	Research Assistant	Ph. D July 1991
Michael Prairie	Research Assistant	Ph. D. Aug. 1991

* Also held an Electronic Materials Fellowship

Section 5: REPORT OF INVENTIONS

Bias Induced Color-Tuned Semiconductor Light Emitter. University has completed a patentability investigation and has concluded that the device is patentable. The University is currently looking for support to proceed with a patent application.

Section 6: REPRINTS OF PUBLICATIONS

(see next page)

Two-terminal bias induced dual wavelength semiconductor light emitter

D. Zhang, F. E. Reed, T. Zhang, N. V. Edwards, and R. M. Kolbas
*Department of Electrical and Computer Engineering, North Carolina State University.
Raleigh, North Carolina 27695-7911*

A new form of light emitting devices called BICE (bias induced color-tunable emitter) is reported. It is a voltage controlled multiwavelength semiconductor light emitter based on the bias dependent injection and collection of electrons and holes in quantum wells. In this letter, two-terminal dual wavelength BICE operation is demonstrated. It exhibits coaxial optical output, a large separation between emission wavelengths (> 500 Å) and an emission contrast ratio ranging from 4:1 to 1:33 at 77 K.

Quantum well heterostructures (QWH) have attracted significant interest because they offer improved performance and design flexibility.[1] QWH lasers and LEDs have grown and diversified into a whole range of sophisticated optoelectronic devices specifically designed for a variety of important applications.[2,3] However, additional advanced components are needed for future systems, which make strong demands on cost, functionality, and performance.

Future advances in optoelectronics require a better understanding of physical processes in semiconductor QWHs. For many years now, carrier collection processes in QWHs have been studied and are considered to be an important criterion for laser operation.[4–8] In this letter, a bias induced color-tunable emitter (BICE) based on selective carrier collection is reported.

BICE is a novel wavelength tunable light emitting device designed for multiwavelength emission along a single optical axis. The emission wavelength is selected by an applied voltage. The optical output power is controlled by an applied current (three-terminal BICE) or an applied optical pump (two-terminal BICE). In this letter, two-terminal BICE operation is demonstrated (using a three-terminal BICE device structure).

The BICE structure described in this work was grown by molecular beam epitaxy (Varian 360) on a Si-doped, (100)-oriented GaAs substrate. The growth of the structure proceeded as follows. First a 5000 Å n-GaAs (Si~5 $\times 10^{18}$ cm^{-3}) buffer layer was grown at 628 °C, then a 3000 Å n-Al$_{0.3}$Ga$_{0.7}$As(Si ~3$\times 10^{17}$ cm^{-3}) layer was deposited followed by a 2000 Å p-Al$_{0.15}$Ga$_{0.85}$As(Be ~8 $\times 10^{16}$ cm^{-3}) layer with the substrate temperature held at 686 °C. The undoped active region, consisting of a 200 Å GaAs single quantum well (SQW) and an Al$_{0.15}$Ga$_{0.85}$As-GaAs multiple quantum well (MQW, 12 periods of 17 Å GaAs and 30 Å Al$_{0.15}$Ga$_{0.85}$As) located 7000 Å apart (insert of Fig. 1), was then grown at a substrate temperature of 640 °C. Subsequently, a 1000 Å n-Al$_{0.15}$Ga$_{0.85}$As(Si ~5 $\times 10^{17}$ cm^{-3}) layer was deposited followed by a 3000 Å p-Al$_{0.3}$Ga$_{0.7}$As (Be ~5$\times 10^{18}$ cm^{-3}) layer with the substrate temperature held at 686 °C. Finally, a 500 Å p-GaAs (Be ~10^{19} cm^{-3}) cap layer used to improve the ohmic contact was then grown at 628 °C to complete the structure. A schematic diagram of the BICE structure is shown in Fig. 1.

The processing of the two-terminal surface emitting

BICE proceeded as follows. First a 160 μm $\times$ 160 μm mesa for device isolation was formed by wet chemical etching. A SiO$_2$ insulating layer was then deposited on top of the structure followed by HF etching to open a top contact window. Finally, to form ohmic contacts, a metal annulet (Cr/Au) was deposited on top of the mesa and AuGe/Au was deposited on the back side of the sample by electron beam evaporation.

To test the device, the sample was cooled to 77 K, photoexcited by an argon-ion laser ($\lambda = 5145$ Å) and biased with a variable dc voltage. The sample was considered to be forward biased when the top epilayer had a higher potential than the substrate, which reverse biased the central active region. Luminescence from the sample was collected and analyzed using a 0.5 m spectrometer and a S-1 photomultiplier.

The emission spectra obtained from the BICE sample described above are shown in Fig. 2 for various forward bias voltages. Note that the scales for all three curves are
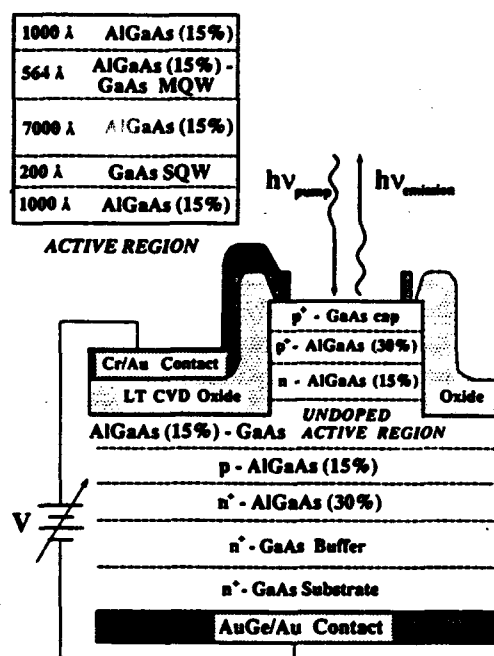

FIG. 1. Schematic diagram of the two-terminal BICE device. The active region of the structure is inserted in the upper left-hand corner of the diagram. Percentage value in parenthesis corresponds to the aluminum composition, x, in Al$_x$Ga$_{1-x}$As.
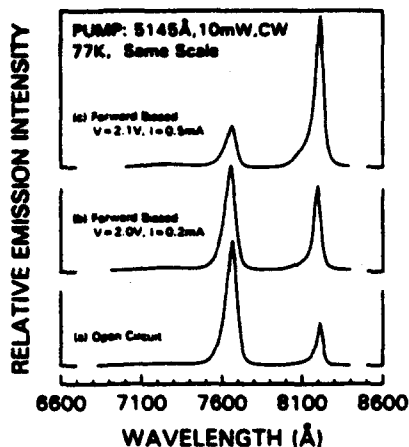
FIG. 2. Emission spectra of the BICE under various forward bias voltages. Note that all three curves are on the same scale. Forward bias corresponds to a positive potential applied to the top epitaxial layer relative to the substrate.

FIG. 3. Emission spectra of the BICE under various reverse bias voltages. Note that all three curves are on the same scale.

the same. The peaks at 7660 and 8200 Å correspond to $n=1$ electron-to-heavy hole transition of the MQW and the SQW, respectively. When there is no applied voltage on the sample (i.e., open circuit), the emission from the MQW dominates the spectrum [Fig. 2(a)]. Then, with a forward bias of 2.0 V, the short wavelength MQW peak remains relatively constant while the SQW peak increases and becomes comparable to the MQW peak [Fig. 2(b)]. By increasing the voltage ($\Delta V = 0.1$ V) to 2.1 V, the MQW emission decreases dramatically and the SQW emission continue to increase as shown in [Fig. 2(c)]. As will be shown later, the contribution of electroluminescence is negligible in this case.

The dramatic change in the emission spectrum is achieved by changing the relative carrier collection and recombination efficiency in the SQW and the MQW with the applied voltage. Since the undoped active region of the sample is slightly p-type ($N_a \approx 4 \times 10^{15}$ cm^{-3}), it is partially depleted near the top n layer without applied bias. The active region can be fully depleted with increased forward bias. When photoexcited, the net effect of photogenerated electron-hole pairs is to flatten the bands, which is equivalent to forward biasing the junctions. Electrons and holes can then inject efficiently into the active region from the bottom and the top pn junctions, respectively, under the electric field across the sample. Carriers can be collected by the MQW and the SQW and recombine to give rise to light emission. The carrier collection efficiency varies dramatically for the MQW and the SQW under different electric fields. Thus a large contrast of emission intensity at different wavelengths is achieved.

The emission spectra obtained from the BICE under reverse bias conditions are shown in Fig. 3. For comparison, the open circuit spectrum is included [Fig. 3(a)]. With increasing reverse bias, the SQW emission fades away and the MQW emission intensity increases just slightly. Note that reverse biasing of the sample forward biases the junctions of the active region. Therefore, the charge depletion on either side of the active region occurs only near the
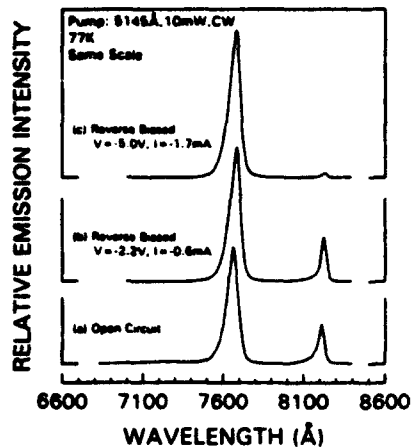
interfaces with the highly doped layers. Both the MQW and the SQW are then in a neutral region with little electric field. Since the MQW is closer to the top layers, photogenerated electrons from the top active region interface layer and holes from the large middle part of the active region (7000 Å) diffuse toward the MQW region. Thus the emission intensity of the MQW is much larger than that of the SQW.

To further investigate the physical mechanisms of two-terminal BICE operation, the device has been examined under the same bias conditions with and without optical pumping (Fig. 4). Under forward bias condition (2.1 V) without optical pumping, only a very small peak corresponding to the SQW emission is observed as shown in Fig. 4(c). Similarly, no emission signal is observed for the reverse bias case (data not shown). This result indicates that electroluminescence is negligible, and that carrier diffusion and collection are significant mechanisms in photoexcited BICE operation.

Defining the intensity contrast ratio, R, as $P_{\lambda 1} : P_{\lambda 2}$, or
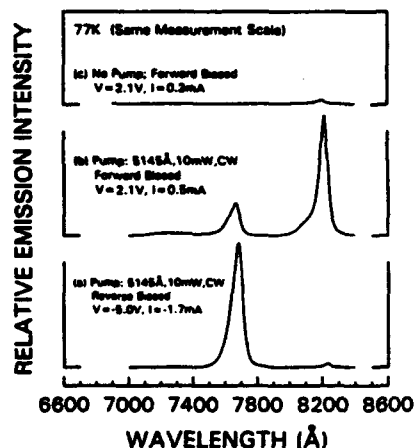

FIG. 4. Emission spectra of the BICE with and without optical pumping with a forward bias of 2.1 V and reverse bias of 5.0 V. No emission signal is observed for the reverse biased case without optical pumping (data not shown). Note that all three curves are on the same scale. The contrast ratios are measured based on (a) and (b).

$P_{SQW}:P_{MQW}$, $R \approx 1:33$ in reverse bias and $R \approx 4:1$ in forward bias [Figs. 4(a) and 4(b)]. Note that a large contrast ratio is achieved by applying only a few volts at very low currents and all applied voltages were below those necessary to obtain p-n-p-n switching action.[9] This device also works at room temperature, but the contrast ratio is reduced. Improved performance at 77 K and room temperature should be possible with an improved design and tighter control of the epitaxial material.

In conclusion, a novel optoelectronic device, BICE, has been demonstrated. A digital switching range of more than 500 Å was demonstrated. A larger tuning range (> 2000 Å) may be possible by adjusting the active region design. Because of its large tuning range, low operational voltage and coaxial output, the BICE concept has potential applications in wavelength division multiplexing and broadly tunable semiconductor lasers.

[1] N. Holonyak, Jr. and K. Hess, in *Synthetic Modulated Structures* (Academic, New York, 1985).
[2] N. Holonyak, Jr., R. M. Kolbas, R. D. Dupuis, and P. D. Dapkus, IEEE J. Quantum Electron. QE-16, 170 (1980).
[3] W. Streifer, P. D. Dapkus, and R. D. Dupuis, eds., IEEE J. Quantum Electron. QE-23, No. 6 (special issue on semiconductor lasers) (1987).
[4] H. Shichijo, R. M. Kolbas, J. N. Holonyak, R. D. Dupuis, and P. D. Dapkus, Solid State Commun. 27, 1029 (1978).
[5] N. Holonyak, Jr., B. A. Vojak, H. Morkoç, T. J. Drummond, and K. Hess, Appl. Phys. Lett. 40, 658 (1982).
[6] H. Shichijo and K. Hess, Phys. Rev. B 23, 4197 (1981).
[7] R. M. Kolbas, Y. C. Lo, and J. H. Lee, IEEE J. Quantum Electron. 26, 25 (1990).
[8] J. H. Lee, K. Y. Hsieh, Y. L. Hwang, and R. M. Kolbas, Appl. Phys. Lett. 56, 1998 (1990).
[9] F. E. Gentry, F. W. Gutzwiller, N. Holonyak, Jr., and E. E. Von Zastrow, *Semiconductor Controlled Rectifiers: Principles and Applications of p-n-p-n Devices* (Prentice-Hall, Englewood Cliffs, NJ, 1964).

Vertical cavity surface emitting laser with a submonolayer thick InAs active layer

S. D. Benjamin, T. Zhang, Y. L. Hwang, M. S. Mytych, and R. M. Kolbas
Department of Electrical and Computer Engineering, North Carolina State University, Raleigh, North Carolina 27695-7911

We report photopumped operation of a vertical cavity surface emitting laser where the active region consists of a single pseudomorphic InAs-GaAs quantum well that is less than one monolayer thick. This represents the thinnest active layer to support stimulated emission when the optical feedback is perpendicular to the layer. Lasing action supported across a submonolayer thick quantum well can be understood by considering the effects on the carrier collection process and the gain across an ultrathin quantum well due to the spreading out of the electron and hole wavefunctions. Pulsed lasing due to gain across the InAs quantum well is confirmed for photoexcitation energies above and below the band edge of the GaAs confining layers at 17 and 77 K.

Early work on single quantum well III–V semiconductor lasers indicated that the carrier collection in thin ($L_z < 100$ Å) undoped wells becomes ineffective and thus cannot support stimulated emission.[1,2] Recently single quantum wells as thin as 2 monolayers (ML) for AlGaAs-GaAs and 1 ML for GaAs-InAs have been shown to support low threshold laser operation[3,4] which indicates that ultrathin wells collect carriers very effectively despite the fact that the well is much thinner than the scattering path length of the excess carriers. These results can be understood by taking into account the spatial extent of the electron and hole wavefunctions which spread out for ultrathin wells, rather than the physical dimensions of the quantum well when considering the collection of carriers in an ultrathin well.[5]

In previous work on semiconductor lasers with conventional cleaved cavities, the optical feedback was parallel to the plane of the quantum well. A new configuration, the vertical cavity surface emitting laser (VCSEL)[6] places the optical feedback perpendicular to the plane of the active layer (quantum well) by incorporating 1/4 wave stack mirrors into the layers comprising the structure. In this letter we report stimulated emission from a VCSEL where the optical feedback is perpendicular to a submonolayer thick InAs quantum well active layer. Although this represents the thinnest active layer to support stimulated emission in this configuration, the results indicate that the electron and hole wavefunction spreading increases the effective gain region to many times the thickness of the quantum well.

The vertical cavity surface emitting laser (VCSEL) structure (Fig. 1) grown by molecular beam epitaxy in a Varian 360 MBE system consists of 1/4 λ stack GaAs-AlAs mirrors grown at 640 °C sandwiching a 10 λ GaAs spacer grown at 640 °C. The active layer in this structure, a single submonolayer InAs quantum well, is located at an antinode in the GaAs spacer 1/2 λ from the top mirror. The InAs quantum well was grown at 550 °C by ramping the growth temperature down to 550 °C before the growth and then back up to 640 °C immediately following the growth of the InAs quantum well. The all binary nature of this design would lend itself to growth by atomic layer

epitaxy which provides the precise control of layer thicknesses and uniformity that is required for VCSELs.

The mirrors are highly reflective over a broad wavelength range centered on the emission of the InAs quantum well and extending to wavelengths shorter than the GaAs band gap. This prevents photoexcitation of the quantum well from the surface of the sample due to the high degree of absorption and/or reflection of the pump laser in this wavelength range. To allow photoexcitation of the quantum well only (hv_{pump} above the quantum well emission but below the GaAs band gap) the sample was cleaved allowing photopumping in the plane of the InAs layer while observing the emission perpendicular to the InAs layer as shown in Fig. 1.

The input versus output power characteristics for this photopumping configuration is shown in Fig. 2 at 17 and 77 K for photoexcitation above and below the band gap of
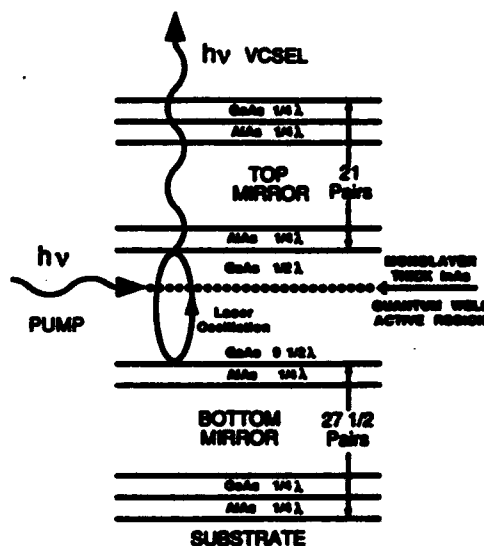

FIG. 1. Structure and photopumping scheme of a VCSEL with a submonolayer thick InAs quantum well active region. The 1/4 λ top and bottom mirrors sandwich a 10 λ GaAs spacer which contains a submonolayer thick InAs quantum well active region. The VCSEL is photopumped (hv PUMP) from a cleaved edge and the emission (hv VCSEL) is observed normal to the as-grown surface.
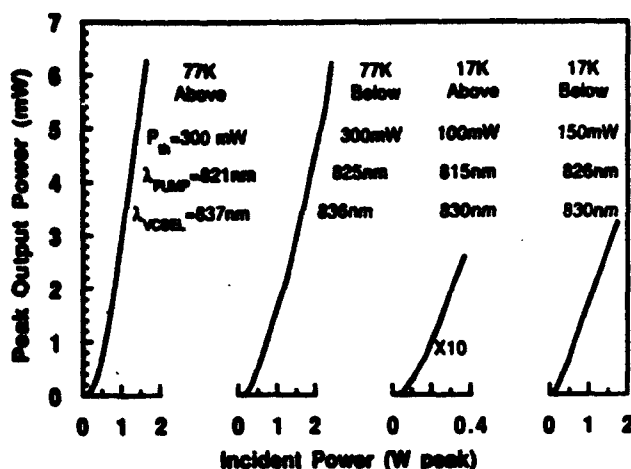
FIG. 2. Output power characteristics of a submonolayer InAs VCSEL for photoexcitation above and below the band gap of the GaAs confining layers (but above the InAs quantum well transition energy) at 77 and 17 K. Stimulated emission when photopumping below the GaAs band gap confirms that the InAs quantum well supports the laser action. To estimate the equivalent current density[13] in kA/cm² multiply incident powers given in watts by 13. The output of the sample at 17 K for above GaAs band gap pumping was limited by the pump power available at that wavelength.
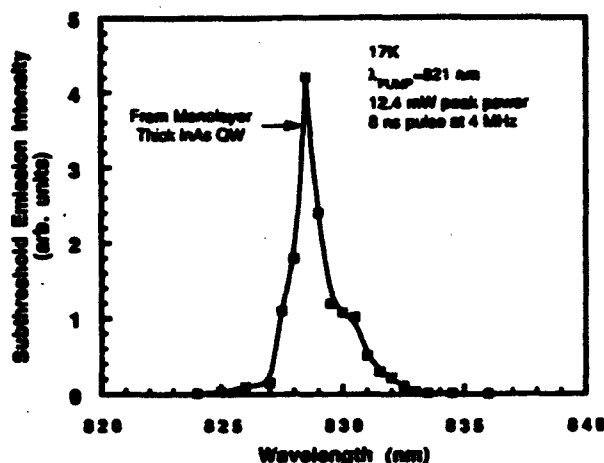
FIG. 3. Photoluminescence spectra of the InAs quantum well at 17 K obtained by translating the excitation spot along a cleaved edge of the wafer to locations with feedback at different wavelengths due to nonuniform layer thicknesses across the wafer. The narrow peak indicates the high quality of the InAs quantum well which is between 0.5 and 0.9 ML based on extrapolation of reports by other workers.

the GaAs confining layers, but above the lowest confined state in the quantum well. The photoexcitation source is a Spectra Physics argon ion laser pumped dye laser that is cavity dumped to obtain 8 ns pulses at a 4 MHz repetition rate. The emission from the surface of the VCSEL is detected with a calibrated United Detector Technology Optometer for power measurements or an ISA 0.32 m spectrometer and S1 photomultiplier tube for spectral measurements. For photoexcitation above the band gap of GaAs at 77 K the sample lases with up to 6.5 mW of peak output power for 1.7 W of peak input power[15] and has a minimum laser threshold of 300 mW peak input power when the sample lases at 837 nm. Photopumping at an energy below the GaAs band gap photoexcites carriers in the InAs quantum well only and provides further conformation that the lasing action is due to the InAs quantum well with a laser threshold around 300 mW peak power and up to 6.25 mW of peak output power for 2.4 W peak input power. The beam divergence is typically 10° which corresponds to a lasing spot diameter of 6 μm. From the two curves on the right-hand side in Fig. 2 the lasing thresholds are lower for laser operation at 17 K which is likely due to linewidth enhancement of gain and the capture/escape dynamics of carriers in monolayer thick wells.[5] The 17 K results will be discussed in detail below.

When a quantum well is placed close to a highly reflecting mirror the optical emission properties of the quantum well are altered[7] and when placed in a feedback cavity the observed emission must also satisfy the Fabry–Perot modes of the cavity. In order to examine the emission properties of the quantum well buried in this structure the central Fabry–Perot mode of the cavity is scanned over the wavelength range of interest by translating the pump beam along a cleaved edge of the sample while observing the photoluminescence from the surface of the sample. This is

possible due to nonuniform layer thicknesses across the sample which was not rotated during growth. The resulting photoluminescence peak shown in Fig. 3 is narrow indicating the high quality of the quantum well and the transition energy enables us to assign an InAs layer thickness of 0.5–0.9 monolayers based on extrapolation of the results of other workers.[8-11] A simple envelope function finite quantum well calculation for the confined particle energies[12] matches the observed emission energy for a layer thickness of 2.1 Å or 0.7 ML. This patchy monolayer can be described as a submonolayer quantum well since the lateral extent of the microscopic hills and valleys that make up the layer is expected to be less than the exciton radius.[8]

To verify that the lasing action is due to the InAs quantum well, the lasing threshold and maximum lasing intensity of the VCSEL are measured as the central Fabry–Perot mode of the cavity is scanned across the gain of the quantum well. For photoexcitation above the band gap of the GaAs confining layers as shown in Fig. 4(a) the minimum laser threshold and maximum VCSEL output occur on the long wavelength side of the InAs quantum well peak as expected for photopumped quantum well lasers.[13] When only the InAs quantum well is excited by photopumping below the band gap of the GaAs, similar laser threshold and output intensity curves are obtained as shown in Fig. 4(b). This is the most convincing evidence for the lasing action being due to gain across the InAs quantum well and not due to gain from the GaAs confining layers since the photoexcitation is far below (> 10 kT) the GaAs band edge allowing carriers to be generated in the quantum well only. The output powers are higher for sub-band-gap photoexcitation because more pump power was available at that wavelength. The lasing threshold is higher when pumping only the InAs quantum well as one might expect.

We have demonstrated that a submonolayer thick InAs quantum well placed in a VCSEL feedback cavity has sufficient gain to support stimulated emission when the
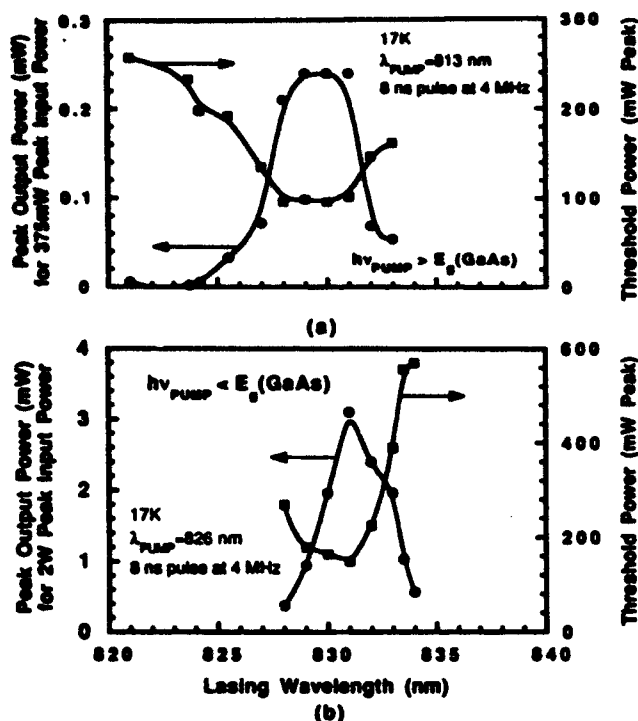
FIG. 4. VCSEL output and lasing threshold for photoexcitation (a) above and (b) below the band gap of the GaAs confining layers. Lasing wavelength was varied by translating the excitation spot along the cleaved edge of the wafer, thereby tuning the Fabry–Perot mode of the structure due to the nonuniform layer thickness across the wafer. (a) Minimum lasing threshold and maximum laser output correspond to the InAs quantum well photoluminescence. (b) the VCSEL lases even though the pump is > 10 kT below the GaAs band edge confirming that the laser action is supported by the InAs quantum well.

feedback axis is perpendicular to the quantum well layer. This laser action with the shortest active medium reported to date can be understood by considering the spatial extent of the wave functions of the confined carriers instead of the physical dimensions of the quantum well when describing the carrier collection and optical gain properties of ultrathin quantum wells. The spreading out of the wave functions would also increase the overlap of the field at the emitting electron-hole pair with the reflected part of the emitted photon, thereby enhancing self-stimulated photon

emission.[14] This additional increase in gain would help to explain laser action supported across ultrathin quantum wells.

These low-temperature results suggest that room-temperature laser action supported across an ultrathin quantum well would be possible provided that the carrier capture by the quantum well could compete favorably with the carrier emission from the well. This requirement is satisfied in a 2 ML InAs-GaAs quantum well since the electron bound state is several kT deep in the quantum well.[8,9] The advanced growth techniques[9,10] required to grow high quality 2 ML InAs-GaAs quantum wells must be incorporated into the growth of a VCSEL to realize room-temperature lasing action in a VCSEL with an ultrathin active layer.

[1] H. Shichijo, R. M. Kolbas, N. Holonyak, Jr., R. D. Dupuis, and P. D. Dapkus, Solid State Commun. 27, 1029 (1978).

[2] J. Y. Tang, K. Hess, N. Holonyak, Jr., J. J. Coleman, and P. D. Dapkus, J. Appl. Phys. 53, 6043 (1982).

[3] J. H. Lee, K. Y. Hsieh, Y. L. Hwang, and R. M. Kolbas, Phys. Rev. B 41, 7678 (1990).

[4] J. H. Lee, K. Y. Hsieh, Y. L. Hwang, and R. M. Kolbas, Appl. Phys. Lett. 56, 626 (1990).

[5] R. M. Kolbas, Y. C. Lo, and J. H. Lee, IEEE J. Quantum Electron. 26, 25 (1990).

[6] S. W. Corzine, R. S. Geels, R. H. Yan, J. W. Scott, L. A. Coldren, and P. L. Gourley, IEEE Photon Tech. Lett. 1, 57 (1989).

[7] T. J. Rogers, D. G. Deppe, and B. G. Streetman, Appl. Phys. Lett. 57, 1858 (1990).

[8] K. Taira, H. Kawai, I. Hase, K. Kaneko, and N. Wantanabe, Appl. Phys. Lett. 53, 495 (1988).

[9] J. M. Gerard and J. Y. Marzin, Appl. Phys. Lett. 53, 568 (1988).

[10] M. Sato and Y. Horikoshi, J. Appl. Phys. 66, 851 (1989).

[11] O. Brandt, L. Tapfer, R. Cingolani, K. Ploog, M. Hohenstien, and F. Phillip, Phys. Rev. B 41, 12599 (1990).

[12] R. Cingolani, O. Brandt, L. Tapfer, G. Scamarcio, G. C. La Rocca, and K. Ploog, Phys. Rev. B 42, 3209 (1990).

[13] R. C. Miller, R. Dingle, A. C. Gossard, R. A. Logan, W. A. Nordland, Jr., and W. Wiegmann, J. Appl. Phys. 47, 4509 (1976).

[14] D. G. Deppe, Appl. Phys. Lett. 57, 1721 (1990).

[15] S. D. Benjamin, *Phonon Assisted Stimulated Emission and Ultra Thin Active Layers in Cleaved Cavity and Vertical Cavity Surface Emitting Lasers* (UMI Dissertation Services, Ann Arbor, 1991).

Time-resolved phonon-assisted stimulated emission in AlGaAs-GaAs quantum wells

S. D. Benjamin, Y. C. Lo, and R. M. Kolbas
Department of Electrical and Computer Engineering, North Carolina State University, Raleigh, North Carolina 27695-7911

Time-resolved photoluminescence of phonon-assisted stimulated emission is reported for the first time. The temporal characteristics of the phonon-assisted stimulated emission are distinct from the stimulated emission from the quantum states. The phonon-assisted recombination is always delayed in time with respect to the confined particle transitions and has a larger full width at half maximum than the confined particle transitions. The dynamics of stimulated phonon emission along with the smaller transition probability for the phonon-assisted process may account for the distinct temporal characteristics. Data are presented on the emission intensity versus wavelength versus time from which the dependence of the delay on excitation intensity is extracted.

Several years ago Holonyak *et al.* reported that AlGaAs-GaAs quantum well heterostructures (QWHs) were capable of laser operation on phonon sidebands.[1-5] This phonon-assisted stimulated emission was characterized by emission one or more longitudinal optical phonon energies ($\hbar\omega_{LO} = 36$ meV) below the allowed quantum well electron-hole recombination transitions. For several years other researchers were unable to reproduce the same laser features and suggested that the 36 meV shift observed by Holonyak was due to impurities,[6] band-gap renormalization,[7] or optical absorption losses in the unexcited portions of the sample.[8] Recent independent work[9] has confirmed the original findings and simultaneously shown the new results to be inconsistent with impurities, bandgap renormalization, or absorption phenomena. Most recently Holonyak and coworkers[10-13] have pointed out why other workers may not have observed phonon-assisted stimulated emission in their experiments. Phonon-assisted stimulated emission has now been observed in AlGaAs-GaAs, InGaAs-GaAs[14,15] grown by either metalorganic chemical vapor deposition or by molecular beam epitaxy and in InAlGaP (Ref. 16) grown by metalorganic chemical vapor deposition. It has been observed in single quantum well heterostructures (SQWHs) and multiple quantum well heterostructures with a wide variety of thicknesses and confining layer compositions.

In this letter we present time-resolved photoluminescence of phonon-assisted stimulated emission in AlGaAs-GaAs single quantum well heterostructures. The temporal characteristics of the phonon-assisted stimulated emission are distinct from the confined particle transitions in that the phonon-assisted process is always delayed in time and typically has a wider temporal full width at half maximum than the other recombination processes. These results are consistent with a previous suggestion that stimulated phonon emission can occur in QWHs.[2]

The separate confinement single quantum well heterostructures used in this work were grown by molecular beam epitaxy at a rate of approximately 125 Å/min. Each sample consisted of a 0.5 μm Al$_{0.35}$Ga$_{0.65}$As cladding layer, a 500 Å Al$_{0.15}$Ga$_{0.85}$As confining layer, a GaAs quantum well (17, 34, or 54 Å), a 500 Å Al$_{0.15}$Ga$_{0.85}$As confining layer, and finally a 0.5 μm Al$_{0.35}$Ga$_{0.65}$As cladding layer. Additional details of the growth can be found elsewhere.[17] Note that these same SQWH samples have shown very efficient carrier collection and are capable of low threshold laser operation, in spite of the fact that the single quantum well is undoped and of dimensions that were previously thought to be too small to effectively collect carriers.[18]

Sample preparation for the photopumped lasers consisted of removing the GaAs substrate from the epitaxial layers by mechanical polishing and selective etching, cleaving the remaining film into rectangular platelets 20–200 μm in width, and pressing the platelets into indium under a sapphire window.[19] The rectangular geometry is important because the higher absorption loss in the unpumped lengthwise direction favors emission at lower energy, and thus facilitates identification of phonon-assisted stimulated emission.[10] The samples are photoexcited in the confining region and quantum well ($E_g < E_{PUMP}$) by a 5 ps ($\lambda_{PUMP} = 6500$ Å; 82 MHz repetition rate) optical pulse produced by synchronously pumping a dye laser excited with the output of a mode locked and frequency doubled Nd:YAG laser. Luminescence from the samples is collected and analyzed using a 0.32 m spectrometer and a streak camera system. The resolution of the system is approximately 15 ps and 10 Å, limited in both cases by the spectrometer.

The 77 K time-resolved stimulated emission spectra from a photopumped rectangular sample from the 54 Å single quantum well heterostructure is shown in Fig. 1. The dark and light markers on the wavelength axis indicate the calculated positions of the $n = 1$ electron to heavy hole ($e \to$ hh) and $n = 1'$ electron to light hole ($e \to$ lh) confined particle transitions. The zero on the time scale corresponds to the arrival of the 5 ps optical pulse and thus to carrier generation in the confining region of the sample. The two laser modes in the foreground correspond to stimulated emission from the $n = 1'$ $e \to$ lh transition. Lasing on these modes is delayed with respect to the lasing on the adjacent modes which are due to stimulated emission from the bandfilled $n = 1$ $e \to$ hh transition. This delay is expected
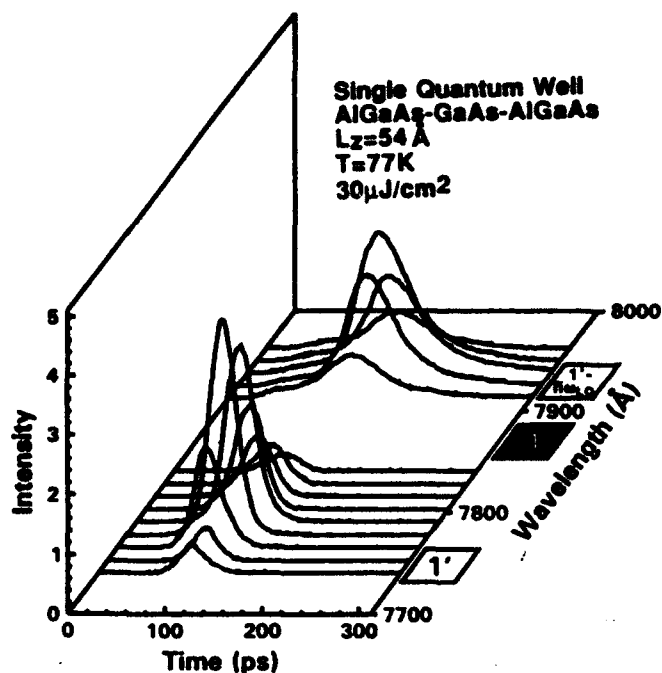
FIG. 1. 77 K time-resolved stimulated emission spectra from a photo-pumped, rectangular sample ($55 \times 250 \ \mu m$) with a 54 Å single quantum well. The zero on the time scale corresponds to the excitation of the sample by the 5 ps optical pulse. The laser modes in the foreground correspond to lasing from the $n = 1'$ $e \rightarrow lh$ and $n = 1$ $e \rightarrow hh$ confined particle transitions. The phonon-assisted stimulated emission (back-ground) which occurs about 36 meV below the $n = 1'$ e to lh transition is delayed with respect to the $n = 1$ and $n = 1'$ emission and has a larger full width at half maximum.
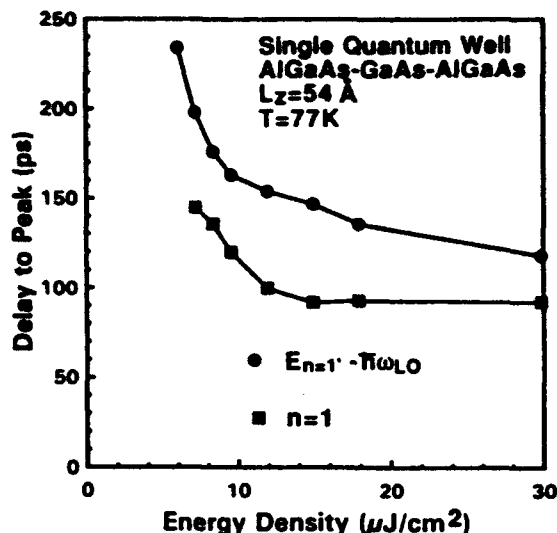

FIG. 2. Delay of the strongest lasing modes from the bandfilled $n = 1$ electron to heavy hole and the phonon-assisted stimulated emission vs excitation energy density per pulse for the same sample as in Fig. 1. The delay of both processes from the pump pulse at $t = 0$ decreases at higher pumping levels. The delay of the phonon-assisted process with respect to the $n = 1$ process also decreases at higher excitation densities.

since the gain at the bottom of the light hole band would be less than the gain well above the bottom of the heavy hole band. The absence of lasing near the bottom of the heavy hole band is not surprising in light of the tendency for samples heat sunk as in this work to lase at energies above the lowest confined particle state.[12] The peak in the photoluminescence lines up with the heavy hole marker at low excitation intensities,[17] confirming our calculation of transition energies.

The phonon-assisted stimulated emission from this sample is seen in the background of Fig. 1, located about one longitudinal optical phonon energy ($\hbar \omega_{LO} = 36$ meV) below the $n = 1'$ $e \rightarrow lh$ confined particle transition energy. This emission was due to lasing along the length of the sample with closely spaced modes not resolved by the streak camera system (but resolved in time-integrated photoluminescence[9]). The phonon-assisted stimulated emission is clearly delayed with respect to the lasing on the confined particle states and it has a larger full width at half maximum. Part of the delay could be caused by the fact that the laser cavity for phonon-assisted stimulated emission is longer and would thus have a higher Q. However we have studied a large number of samples and have not been able to correlate the delay to the length or width of the platelets. As well, preliminary results from a computer solution of the rate equations for this system[20] indicate that only a portion of the delay can be explained in terms of resonator cavity effects.

The delay time between the pump pulse and lasing from the bandfilled $n = 1$ $e \rightarrow hh$ confined state and the phonon-assisted process is correlated to the excitation energy density per pulse as shown in Fig. 2. These delay times were obtained from the strongest lasing modes in Fig. 1 and from similar data obtained at lower excitation densities. Note that the delay for both processes decreases at higher excitation density and also that the delay of the phonon-assisted lasing with respect to the $n = 1$ $e \rightarrow hh$ quantum well lasing also decreases slightly at higher excitation density. Part of the delay of the phonon-assisted lasing with respect to the $n = 1$ $e \rightarrow hh$ quantum well lasing may be due to the build up of stimulated phonon emission which then facilitates phonon-assisted stimulated emission. In addition the weaker matrix element expected for phonon-assisted recombination[21] would lead to lower gain and contribute to the delay of the phonon-assisted stimulated emission with respect to the stimulated emission from the $n = 1$ $e \rightarrow hh$ quantum well transition. This delay ranged from 20 to 100 ps for all of the samples and structures used in this work and should not be confused with the phonon emission time associated with the relaxation of photoexcited electrons which is two orders of magnitude shorter.[22]

The 77 K time-resolved stimulated emission spectra from a rectangular sample from the thinnest single quantum well structure (17 Å) studied in this work is shown in Fig. 3. Due to the increased confinement in this thin well the separation between the $n = 1$ $e \rightarrow hh$ and $n = 1'$ $e \rightarrow lh$ energy states is increased which causes the $n = 1$ lasing and the phonon-assisted lasing to occur closer in wavelength. This has made identification of the phonon-assisted process in this sample difficult using only time integrated photoluminescence spectra. However from the time-resolved photoluminescence spectra of Fig. 3 the long wavelength peak is delayed from and has a wider FWHM than
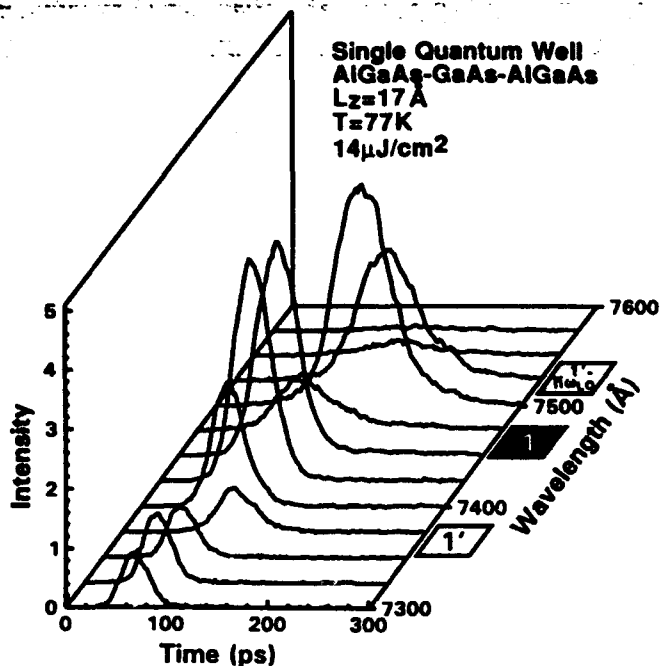
FIG. 3. 77 K time-resolved stimulated emission spectra from a photopumped, rectangular sample ($75 \times 288 \ \mu$m) with a 17 Å single quantum well. Lasing from the $n = 1'$ electron to light hole state (foreground), and the $n = 1$ electron to heavy hole state (middle) are clearly visible. The phonon-assisted process (background) is delayed and has a wider full width at half maximum than the other processes.

the lasing from the confined particle transitions, characteristic of the phonon-assisted process.

The dependence of the delays on the excitation density is shown in Fig. 4 for the 17 Å sample where data were taken only from the most intense of the $n = 1 \ e \rightarrow hh$ and phonon-assisted laser modes in order to obtain a larger
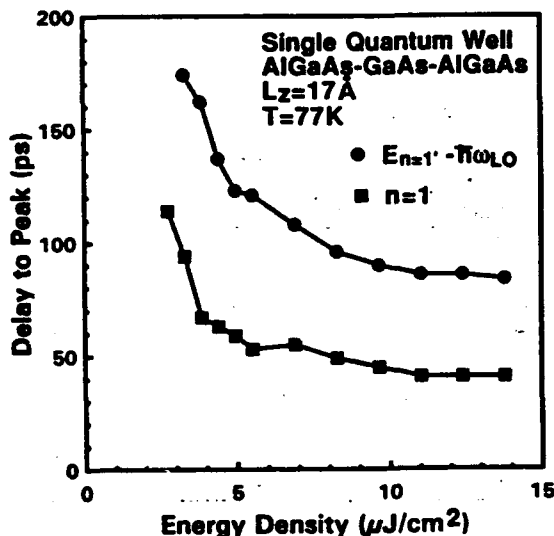
FIG. 4. Delay of $n = 1$ electron to heavy hole and phonon-assisted stimulated emission vs excitation density for the same sample as in Fig. 3. The delay of both processes from the pump pulse at $t = 0$ decreases at higher pumping levels. The delay of the phonon-assisted process with respect to the $n = 1$ process also decreases at higher excitation densities.

number of data points in a short time. As before the delays of both processes are shorter at higher excitation densities and the delay of the phonon-assisted lasing with respect to the $n = 1$ state lasing is also slightly shorter at higher excitation densities. Similar results were obtained for a 34 Å SWQH also studied in this work.

Time-resolved optical spectroscopy has aided in the identification of phonon-assisted stimulated emission which is delayed from lasing on the confined particle states in AlGaAs-GaAs photopumped lasers. The delay of the phonon-assisted process could be due to resonator cavity effects, stimulated phonon emission or from the weaker matrix element that would be expected for the phonon-assisted process. However, preliminary results from a computer solution of the rate equations for this system[20] indicate that only a portion of the delay can be explained in terms of resonator cavity effects.

[1] N. Holonyak, Jr., R. M. Kolbas, W. D. Laidig, M. Altarelli, R. D. Dupuis, and P. D. Dapkus, Appl. Phys. Lett. 34, 502 (1979).
[2] R. M. Kolbas, N. Holonyak, Jr., B. A. Vojak, K. Hess, M. Altarelli, R. D. Dupuis, and P. D. Dapkus, Solid State Commun. 31, 1033 (1979).
[3] N. Holonyak, Jr., R. M. Kolbas, W. D. Laidig, B. A. Vojak, K. Hess, R. D. Dupuis, and P. D. Dapkus, J. Appl. Phys. 51, 1328 (1980).
[4] N. Holonyak, Jr., R. M. Kolbas, R. D. Dupuis, and P. D. Dapkus, IEEE J. Quantum Electron. QE-16, 170 (1980).
[5] N. Holonyak, Jr., W. D. Laidig, M. D. Camras, H. Morkoc, T. J. Drummond, and K. Hess, Solid State Commun. 40, 71 (1981).
[6] J. E. Fouquet and R. D. Burnham, IEEE J. Quantum Electron. QE-22, 1799 (1986).
[7] S. Tarucha, M. Kobayashi, Y. Horikoshi, and M. Okamota, Jpn. J. Appl. Phys. 23, 874 (1984).
[8] S. Tarucha, Y. Horikoshi, and H. Okamoto, Jpn. J. Appl. Phys. 22, L482 (1983).
[9] Y. C. Lo and R. M. Kolbas, Appl. Phys. Lett. 53, 2266 (1988).
[10] N. Holonyak, Jr., D. W. Nam, W. E. Plano, E. J. Vesely, and K. C. Hsieh, Appl. Phys. Lett. 54, 1022 (1989).
[11] B. A. Vojak, and N. Holonyak, Jr., Appl. Phys. Lett. 54, 2518 (1989).
[12] N. Holonyak, Jr., D. W. Nam, W. E. Plano, and K. C. Hsieh, J. Phys. Chem. 94, 1082 (1990).
[13] N. Holonyak, Jr., D. W. Nam, E. J. Vesely, L. J. Guido, P. Gavrilovic, K. Meehan, W. Stutius, and J. E. Williams, Appl. Phys. Lett. 56, 60 (1990).
[14] D. W. Nam, N. Holonyak, Jr., and K. C. Hsieh, J. Appl. Phys. 66, 1347 (1989).
[15] K. Y. Hsieh, Ph.D. dissertation, North Carolina State University, (1990).
[16] D. W. Nam, N. Holonyak, Jr., K. C. Hsieh, C. P. Kuo, R. M. Fletcher, T. D. Osentowski, and M. G. Craford, Appl. Phys. Lett. 54, 2446 (1989).
[17] Y. C. Lo, K. Y. Hsieh, and R. M. Kolbas, Appl. Phys. Lett. 52, 1853 (1988).
[18] R. M. Kolbas, Y. C. Lo, and J. H. Lee, IEEE J. Quantum Electron. QE-26, 25 (1990).
[19] N. Holonyak, Jr. and D. R. Scifres, Rev. Sci. Instrum. 42, 1885 (1971).
[20] S. D. Benjamin and R. M. Kolbas (unpublished).
[21] B. Segall and G. D. Mahan, Phys. Rev. 171, 935 (1968).
[22] J. A. Kash, J. C. Tsang, and J. M. Hvam, Phys. Rev. Lett. 54, 2151 (1985).

VISIBLE LIGHT EMISSION FROM SILICON NANOPARTICLES

D. Zhang*, R. M. Kolbas*, P. Mehta**, A. K. Singh**, D. J. Lichtenwalner**,
K. Y. Hsieh** and A. I. Kingon**

*Department of Electrical and Computer Engineering, North Carolina State
  University, Raleigh, N.C. 27695-7911
**Department of Material Science and Engineering, North Carolina State
  University, Raleigh, N.C. 27695-7919

ABSTRACT

Orange-red light emission has been observed for the first time from
crystalline silicon nanoparticles produced by gas phase synthesis in a
non-thermal microwave plasma. The size and crystalline nature of the
particles have been confirmed by transmission electron microscopy and
X-ray diffraction. Photoluminescence at 300 K and 77 K has been
measured and analyzed. The emission spectra are consistent with
quantum mechanical calculations based on a quantum box.

INTRODUCTION

Recently there has been considerable interest in visible light
emission from silicon (Si) nanostructures.[1,2,3] Most recent reports have
concentrated on porous Si quantum wire structures, although the earliest
reports focused on microcrystalline Si:H.[3] In this paper, the
luminescence and structural properties of crystalline silicon
nanoparticles produced by gas phase synthesis are presented. Visible
orange-red light emission has been observed. The Si nanoparticles were
characterized by transmission electron microscopy (TEM), X-ray
diffraction (XRD), and both time-integrated and time-resolved
photoluminescence. A simple quantum mechanical calculation based on
a quantum box is presented.

EXPERIMENTAL PROCEDURE

The crystalline silicon nanoparticles examined were prepared
using a non-thermal microwave plasma reactor[4]. Electronic grade silane
(SiH_4) was used as the precursor gas, and ultrahigh purity argon (Ar)
served as a carrier gas and a diluent. A mixture of 10 sccm SiH_4 and 90
sccm Ar were used, with the system pressure held at 1 torr and a
plasma power of 150 watts. The gas flow was laminar, allowing the
particles produced in the plasma region to be carried downstream where

they were collected on a Teflon filter paper (10 μm pore size) mounted in the reactor tube. An advantage of this synthesis technique is that alternative semiconductor materials can also be prepared as nanocrystalline particles.

The microstructural properties of the Si particles were analyzed using TEM (Hitachi H-800, 100 kV electron energy) and XRD (Rigaku diffractometer, Cu(Kα) radiation, λ=1.5418Å). Preparation for photoluminescence consisted of pressing the silicon particles into indium on a copper plug as a heat sink. The samples were then photoexcited using an argon ion laser (λ=5145Å, pulsed). Luminescence from the sample was collected and analyzed using a 0.5-m spectrometer and a cooled S-1 phtomultiplier. The radiative lifetime measurements were performed using a 5 ps (λ_{pump} = 6586 Å, 82 MHz repetition rate) optical pulse from a synchronously pumped DCM dye laser excited with a mode locked and frequency doubled Nd:YAG laser. Luminescence from the sample was measured using a 0.32-m double subtractive monochromator and a streak camera system. The temporal resolution of the system was approximately 15 ps.

RESULTS AND DISCUSSION

Bright field and dark field TEM images of the collected Si particles are shown in Figs. 1(a) and 1(b). The bright field image reveals the

(a)   (b)
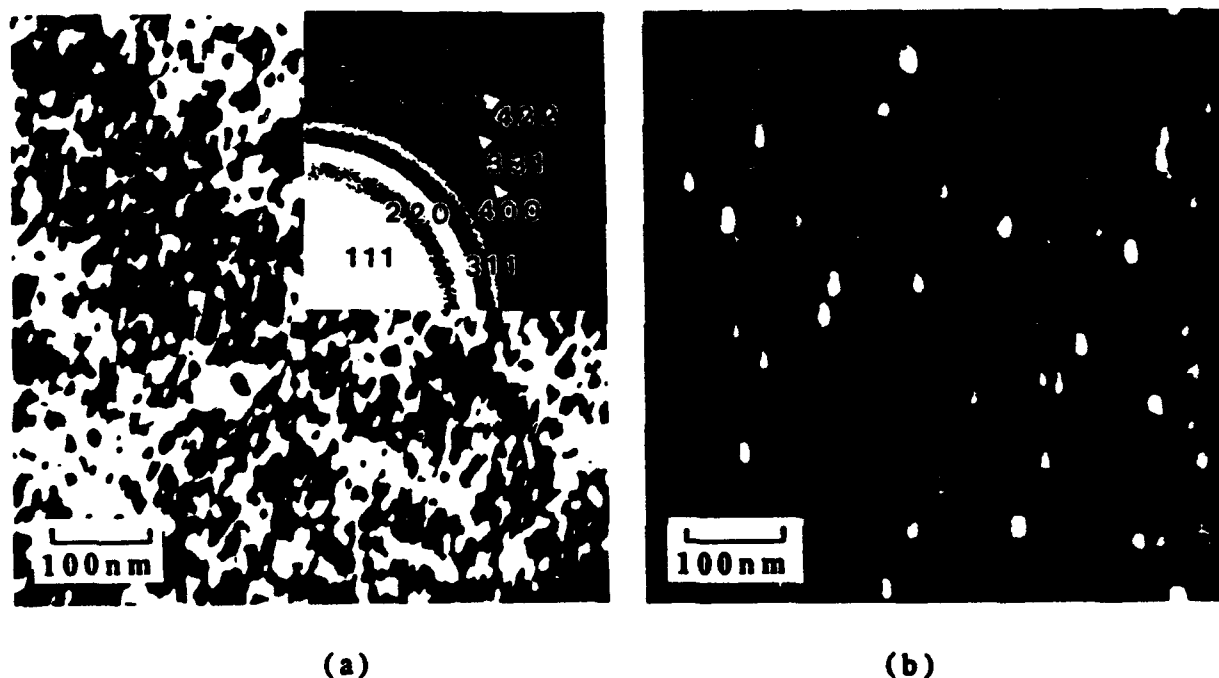
Fig. 1   TEM micrographs of Si particles. (a) Bright field image, with the electron diffraction pattern inserted at the top right corner. (b) Dark field image, in which only electrons diffracted from crystal of a given orientation are observed.

small particle size, and the electron diffraction pattern (top corner of Fig. 1(a)) reveals that the particles are indeed crystalline silicon. The diffraction rings are fairly broad and diffuse because of the small particle size.[5] The dark field image in Fig. 1(b) provides a measure of the particle sizes and indicates that each particle is single crystal. In dark field, the image is formed by electrons which have been diffracted from particles of a given orientation only. The particles observed range from 5 to 20 nm in diameter with an average size of about 12 nm. The particles appear elongated in one direction due to sample vibration during photographic exposure.

The crystallinity and small particle size are also confirmed by the X-ray diffraction pattern shown in Fig. 2. The peak positions reveal a lattice parameter of 5.434(± .007) Å which is virtually identical to the 5.430 Å for bulk Si. The width of the diffraction peaks can be used to obtain a rough estimate of particle size, neglecting the effects of stacking faults and non-uniform strain.[5] Using Warren's method[5], the particle size calculated from the three largest diffraction peaks ranges from 12 to 18 nm, which is in general agreement with the TEM results.
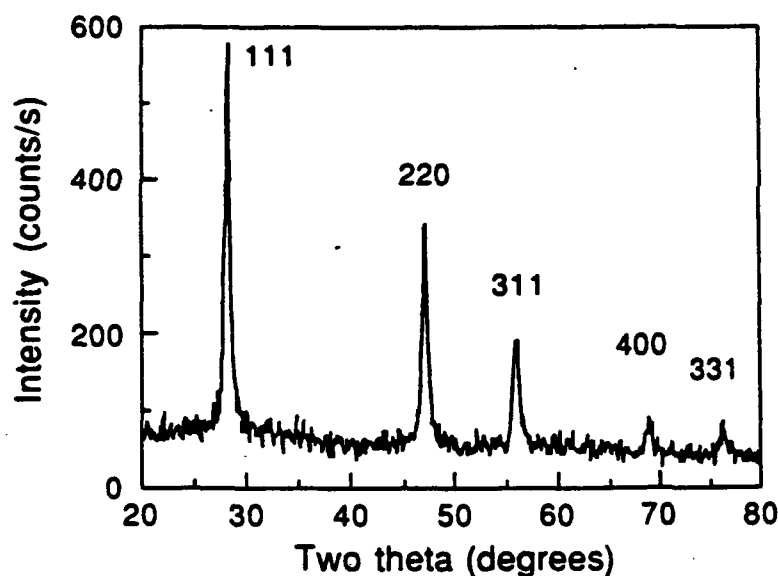
Fig. 2 X-ray diffraction pattern of Silicon particles.

Photoluminescence from the crystalline silicon nanoparticles at 300 K and 77 K is shown in Fig. 3. Bright orange-red light emission can been seen from the sample when viewed through a long-pass optical filter that blocks the pump laser. The broad range of the luminescence and the numerous peaks are believed to be due to the non-uniform distribution of particle sizes. Since the focused laser beam is about 10 μm in diameter, thousands of particles are being excited simultaneously. Note that the peak shifts to a shorter wavelength at 77 K, which is due to the increase in the band gap of silicon at low temperatures.[6]
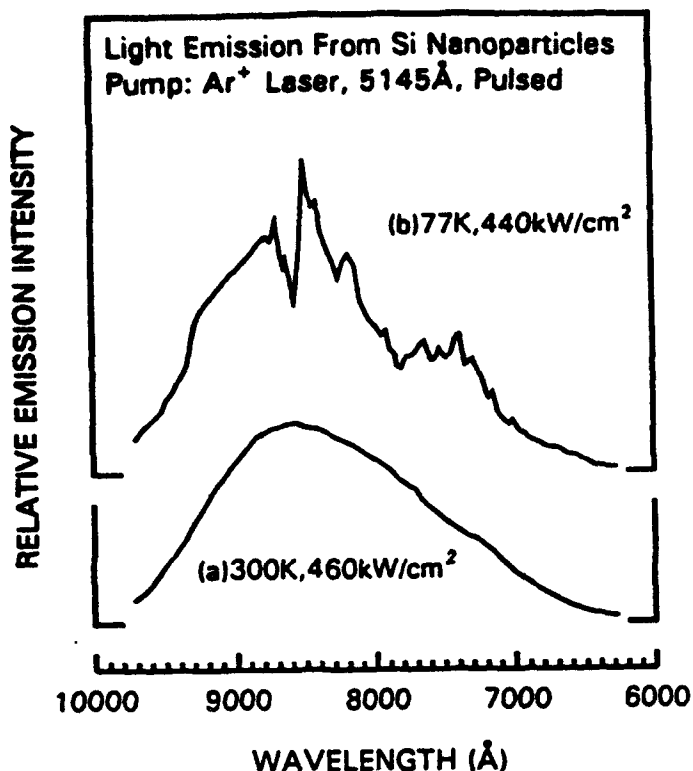
Fig. 3 Time-integrated photo-luminescence of the crystalline silicon nano-particles at 300 K and 77 K. Note that the non-uniform distribution in particle sizes is partially resolved at 77 K.
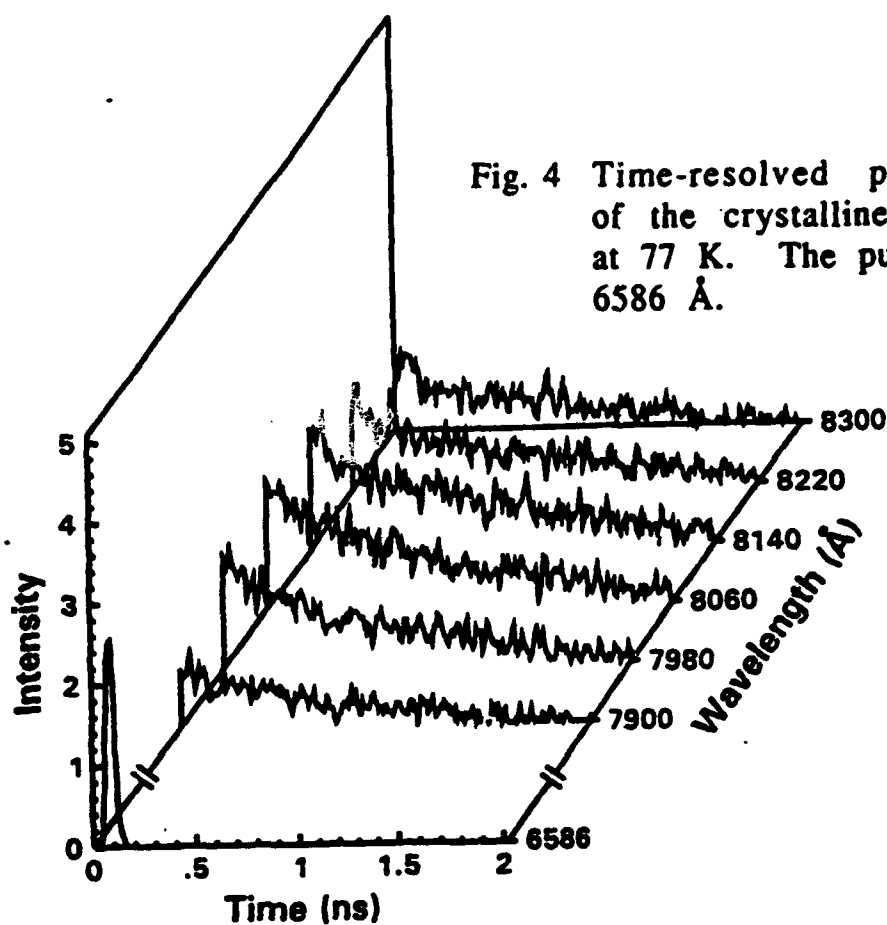
Fig. 4 Time-resolved photoluminescence of the crystalline Si nanoparticles at 77 K. The pump wavelength is 6586 Å.

Time-resolved photoluminescence at 77 K from the same sample is shown in Fig. 4. The radiative lifetime was determined to be approximately 1 ns by measuring the exponential decay time of the light emission. It is interesting to note that the radiative lifetime is very close to the lifetimes of direct band gap materials. This characteristic suggests that the radiative recombination mechanism in these nanoparticles is much different than that in indirect band gap materials like bulk silicon. The ultra-small size of the silicon particles should quantum confine the electrons and holes. This strong quantum confinement may enhance scattering or phonon processes that make efficient radiative recombination possible in these silicon nanoparticles.

The transition energies resulting from quantum confinement or quantum size effects were calculated based on spherical and cubic symmetries. Since it was mathematically easier to include the anisotropic effective mass for the case of cubic symmetry (in contrast to spherical symmetry), the calculated emission wavelength versus size for a quantum box is shown in Fig. 5. The equivalent ball diameter is the diameter of a sphere with the same volume of the cube. The model assumes an infinite potential outside the quantum cube. The quantized energy states can be obtained for both the conduction and valence bands by solving the Schrödinger wave equation. The difference in emission
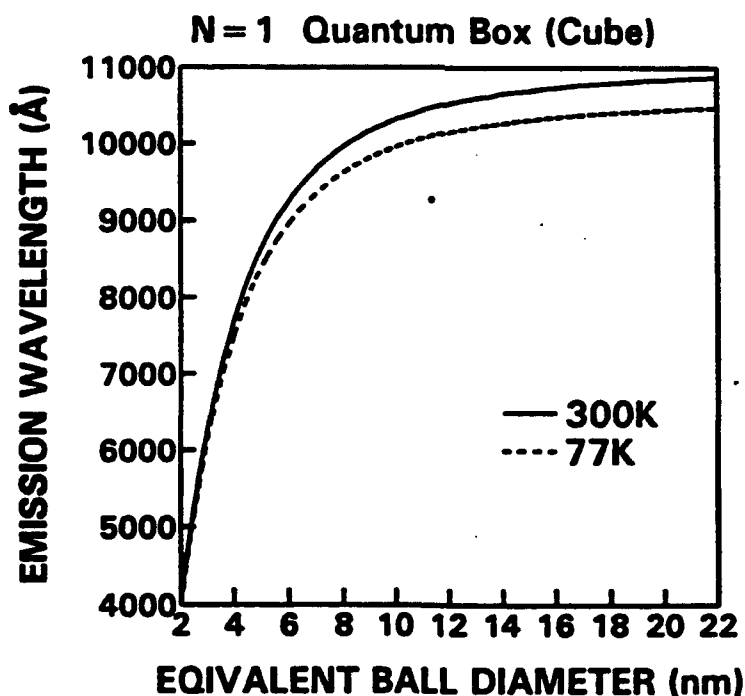

N = 1 Quantum Box (Cube)

Fig. 5 Quantum mechanical calculation of the emission wavelength versus particle size for a quantum box, with the box dimension converted to an equivalent sphere diameter of the same volume.

wavelengths at 300 K and 77 K is due to the increase in the band gap of Si at low temperatures.[6] Based on the measured emission spectrum, the simple model predicts a particle size in the range of 4–6.5 nm, which corresponds to the lower end of the size range revealed by TEM. The difference between the predicted particle size and the "average" size observed by TEM and XRD could be due to: (1) impurities (e.g. H, C, O), (2) a thin oxide layer covering each particle, (3) too simplistic a model, (4) that only the smallest nanoparticles have a high enough radiative recombination rate (oscillator strength) to contribute to the optical emission.

CONCLUSION

We have demonstrated that crystalline silicon nanoparticles can emit bright visible light at 300 K and 77 K. The emission spectra are consistent with a quantum mechanical calculation for a quantum box. These results should be helpful in understanding the physical mechanisms of light emission from silicon nanostructures.

ACKNOWLEDGEMENTS

REFERENCES

1. L. T. Canham, Appl. Phys. Lett. 57, 1046 (1990).
2. S. Gardelis, J. S. Rimmer, P. Dawson, B. Hamilton, R. A. Kubiak, T. E. Whall, and E. H. C. Parker, Appl. Phys. Lett. 59, 2118 (1991)
3. S. Furukawa and T. Mijasato, Phys. Rev. B 38, 5726 (1988).
4. A. K. Singh, P. Mehta, and A. I. Kingon, in Ceramic Trans., 21, Microwaves: Theory and Application in Materials Processing, edited. by D. E. Clark, F. D. Gac, and W. H. Sutton (American Ceramic Society, Westerville, OH, 1991), p. 421.
5. B. D. Cullity, Elements of X-ray Diffraction (Addison-Wesley Pub. Co., Inc., Reading, MA, 1978).
6. Landolt-Börnstein, Numerical Data and Functional Relationships in Science and Technology, Vol. 17, Subvol. a, edited by O. Madelung (Springer-Verlag Berlin, Heidelberg, New York, 1982), p. 43.

A GENERAL DERIVATION OF THE DENSITY OF STATES FUNCTION FOR QUANTUM WELLS AND SUPERLATTICES

M. W. Prairie and R. M. Kolbas

Department of Electrical and Computer Engineering
North Carolina State University, Raleigh, North Carolina 27695-7911

The intent of this paper is to provide the reader with a detailed summary of the development of the density of states (DOS) functions for two-dimensional systems. Specifically, the DOS is derived for an infinite quantum well, a finite well, and a periodic array of coupled wells (a superlattice). Many authors state that the DOS is "simply ..." without references, yet many who are new to the subject of two-dimensional systems may not see the "simplicity," for instance, of the derivation of the DOS for a superlattice. We also show the relationships between the expressions for each case when the appropriate limits are taken. This comparison shows the consistency that such a general derivation furnishes to each expression.

Introduction

The distribution of carriers (electrons or holes) per unit energy interval in a semiconductor is determined by the density of states (DOS) and the Fermi-Dirac distribution functions. The DOS function tells us how many electron or hole states are in an interval of energy, while the Fermi-Dirac function tells us the probability of finding a carrier for each of those states. For instance, in the case of a superlattice, the distribution of electronic states, or the DOS, is somewhere between that of a quantum well and the bulk semiconductor, and the absorption and emission lineshapes are greatly affected due to the form of the DOS function.[1] This suggests that an understanding of the distribution of states is crucial in the development of optoelectronic devices employing two-dimensional systems.

In this review, the DOS function is first derived for the simple case of the ideal (infinite), two-dimensional (2D) square well. This pure 2D analysis is found to be inadequate and is improved with the incorporation of the third dimension (the well width). The next section considers the DOS function for thin or shallow wells with the bound states of interest near the top of the well. In this case, the ideal analysis breaks down, and the bound states must be found numerically and inserted into the DOS function. The effects of coupling between an array of finite quantum wells is considered next in the derivation for superlattices. Finally, the equivalence between each case is shown as the appropriate limits are taken. First is an example of the equivalence of the single well DOS to that of the bulk semiconductor as the well width is allowed to go to infinity. Next, a conceptual analysis is used to show that the superlattice DOS reduces to the single quantum well case as the barrier width gets large, and the

three-dimensional (3D) DOS is achieved when the barrier width goes to zero, or the well width goes to infinity.

The Infinite Potential Well

The density of states (DOS), $g(E)$, is defined such that the number of orbital states per unit volume with energy between E and dE is[2,3]

$$g_i(E)dE = \sum_{spin}\sum_{min}\sum_{other} \int \frac{d\vec{k}}{(2\pi)^i}$$

where i is the number of dimensions, $d\vec{k}$ is the differential volume (3D), area (2D) or length (1D) element for a surface of constant energy, and the summations are taken over spin, degenerate band minima, and any other mechanism resulting in a degeneracy of electronic states. For energy surfaces with a high degree of symmetry (spherical, parabolic, etc.), the differential volume element can be coverted to a differential function of energy, and the DOS is obtained by taking the derivative of both sides of the above equation with respect to E. However, since such symmetry is not always the case, we will use the general expression for the DOS, which is given by[2,3]

$$g_i(E) = \sum_{spin}\sum_{min}\sum_{other} \int \frac{1}{(2\pi)^i} \frac{dS}{|\nabla_k E|} \quad (1)$$

where dS is the differential surface area of the constant energy surface in 3D, while we use a differential length for the 2D case.

The energy, E, of an electron near the minima of the conduction band in the free particle approximation is given by

$$E = \frac{\hbar^2 k^2}{2m^*}$$ (2)

where $\hbar$ is Plank's constant divided by 2π, k is the wavevector of the particle, and m^* is the effective mass.

For the pure 2D case with only spin degeneracy, spherical energy surface, and $k^2 = k_x^2 + k_y^2$, Equation (1) becomes

$$g_2(E) = 2 \int \frac{dS}{(2\pi)^2 |\nabla_k E|}$$

$$= \int_0^{2\pi} \frac{2k\, d\phi}{4\pi^2 |\nabla_k [\hbar^2 (k_x^2 + k_y^2)/2m^*]|}$$

$$= \frac{2\pi k}{2\pi^2 \hbar^2 k/m^*}$$

$$= \frac{m^*}{\pi \hbar^2}.$$ (3)

Equation (3) is the DOS for the pure 2D case where there is no z dimension, and bound states higher than $n=1$ are neglected. In reality, there is a z dimension, which in fact is responsible for the quantum size effects in a real device. To find the DOS using the more general approach, we must solve the problem in three dimensions. The energy is then

$$E = \frac{\hbar^2}{2m^*}(k_x^2 + k_y^2 + k_z^2)$$

$$= \frac{\hbar^2}{2m^*}(k^2 + k_z^2),$$ (4)

where the electron is free in the x and y directions (k_x and k_y are continuous), while it is bound in the z direction (k_z is discrete). With the help of Figure 1, the differential surface area is

$$dS = k\, d\phi \sqrt{(dk)^2 + (dk_z)^2}.$$ (5)

Since the differential change in energy along a constant energy surface is zero,

$$dE = \frac{\hbar^2}{m^*}(k\, dk + k_z\, dk_z) = 0,$$
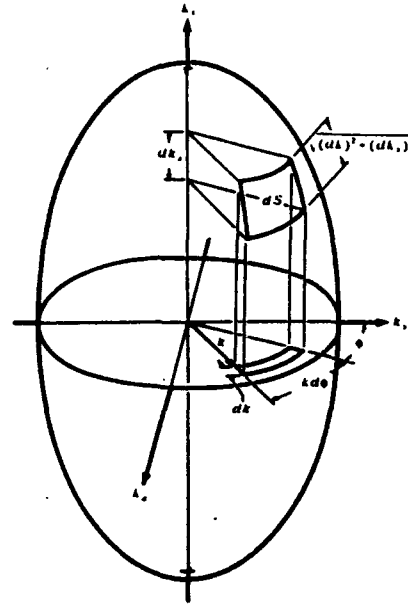
so

$$dk = -\frac{k_z}{k}dk_z.$$ (6)

Figure 1. Differential surface area of a constant energy surface in cylindrical coordinates. The x-y cross section is circular, but the x-z (or y-z) cross section is not necessarily circular.

Substituting this expression into dS, we get

$$dS = k\, d\phi \sqrt{\left(-\frac{k_z}{k}dk_z\right)^2 + (dk_z)^2}$$

$$= \sqrt{k^2 + k_z^2}\, dk_z\, d\phi.$$ (7)

The 3D single quantum well (SQW) DOS is then

$$g_3^{SQW}(E) = \int_{-k_z}^{k_z} \int_0^{2\pi} \frac{2\sqrt{k^2 + k_z^2}\, d\phi\, dk_z}{8\pi^3 \left|\nabla_k \left[\frac{\hbar^2}{2m^*}(k^2 + k_z^2)\right]\right|}$$

$$= \int_{-k_z}^{k_z} \frac{\sqrt{k^2 + k_z^2}\, dk_z}{2\pi^2 \frac{\hbar^2}{m^*}\sqrt{k^2 + k_z^2}}$$

$$= \frac{m^*}{\pi^2 \hbar^2}k_z.$$ (8)

Recall from the solution of the infinite square well problem that k_z is quantized, and is given by $k_z = n\pi/L_z$ where L_z is the width of the well.[4] Inserting this into Equation (8) gives

$$g_3^{SQW}(E) = \frac{m^*}{\pi \hbar^2}\frac{n}{L_z}.$$ (9)

Comparing this result to Equation (3), we see that

$$g_3^{SQW}(E) = g_2(E)\frac{n}{L_z} \qquad n = 1,2,3,\ldots \quad (10)$$

This same result can also be obtained starting with the 3D DOS. Using Equation (1), the 3D DOS for a bulk semiconductor is given by the well-known expression[5]

$$g_3(E) = \frac{\sqrt{2}(m^*)^{\frac{3}{2}}}{\pi^2 \hbar^3}\sqrt{E}. \qquad (11)$$

The solution to the infinite square well (ideal case) results in quantized energies, and for both k_x and k_y equal to zero, is given by[6]

$$E_n = \frac{\pi^2 \hbar^2 n^2}{2m^* L_z^2} \qquad n = 1,2,3,\ldots \quad (12)$$

Using this form of the energy in Equation (11), the 3D DOS becomes

$$g_3^{SQW}(E) = \frac{\sqrt{2}(m^*)^{\frac{3}{2}}}{\pi^2 \hbar^3}\frac{\pi \hbar n}{\sqrt{2m^*}L_z}$$

$$= \frac{m^*}{\pi \hbar^2}\frac{n}{L_z} \qquad (13)$$

which is identical to Equations (9) and (10). Equations (10) and (12) are shown graphically in Figure 2 below. Note for each step in n, a constant $g_2(E)/L_z$ is added to the 3D DOS function, which results in a set of steps that follow the bulk DOS curve.
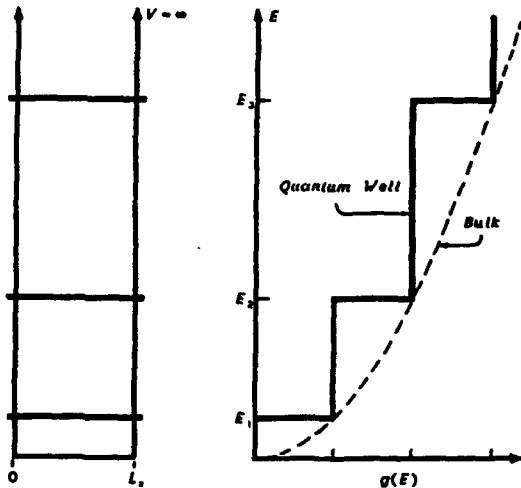
Figure 2. The DOS of an infinite quantum well as it corresponds to the bound-state energies. In this case, the bound-state energy is inversely proportional to the well width, while the DOS is inversely proportional to the *square* of the width, so a well that is half as thick as the original one will have a bound state twice as high, and a DOS *four times* the original value.

The Finite Potential Well

We have seen so far that the DOS of an infinite potential well is a step-like function, where a constant $g_2(E)/L_z$ is added to $g_3^{SQW}(E)$ for each quantized step in energy. For the finite well, however, the wave-functions near the top of the well are less confined, resulting in lower bound state energies compared to those of the infinite well, resulting in different size steps in the DOS. This can be seen by solving Schrödinger's Equation and numerically or graphically finding the values for the bound states.[7]

The finite potential well is shown in Figure 3. Taking the bottom of the well as zero potential and the top of the well as V_0, we can define the following variables:

$$\alpha^2 = \frac{2m^*(V_0 - E)}{\hbar^2}$$

$$k^2 = \frac{2m^*E}{\hbar^2}$$

$$\gamma^2 = \frac{2m^*V_0}{\hbar^2}.$$

For even wavefunctions, the solution is

$$\alpha = k\tan\left(k\frac{L_z}{2}\right), \qquad (14)$$

while the odd solution is

$$\alpha = -k\cot\left(k\frac{L_z}{2}\right). \qquad (15)$$

Also, notice that from the defined variables,
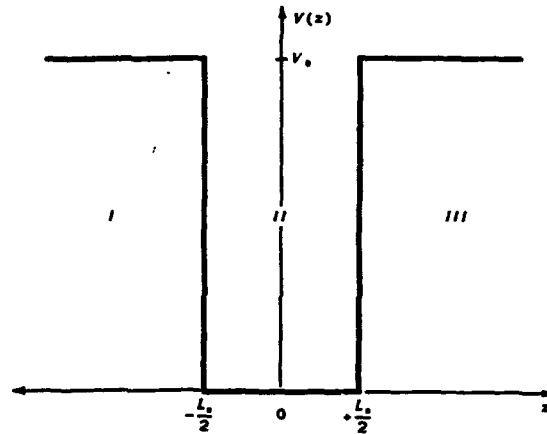
$$\gamma^2 = \alpha^2 + k^2, \qquad (16)$$

Figure 3. Finite potential well. The width is L_z, and the potential depth is V_0.

which is the equation for a circle with radius γ. Graphing equations (14-16) as in Figure 4, we can find the set of allowed values k_n, which give us the values of the energy eigen states

$$E_n = \frac{\hbar^2}{2m^*} k_n^2 .$$ (17)

Using Equation (17) in (11), we find the DOS for the finite quantum well (FQW) to be
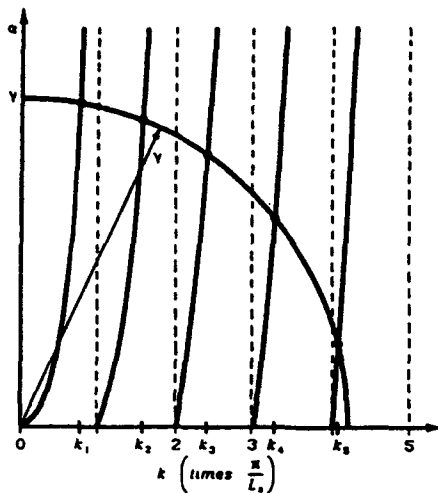
$$g_3^{FQW}(E) = \frac{m^* k_n}{\pi\hbar^2 \pi} .$$ (18)

Figure 4. Graphical solution for bound states in a finite potential well. As the well gets thinner, the circular curve of radius γ will contract. In this case (symmetric well), there will always exist at least one bound state.

Notice that $\Delta k = k_{n+1} - k_n$ is no longer a constant. In fact, Δk gets smaller as n gets bigger for the same reason that each bound state of the finite well is lower than the corresponding eigen energy of the infinite well by an increasing amount as n increases as shown in Figure 5.

Notice that the highest bound state of the finite quantum well is very near the top of the well. Referring back to Figure 4, the intersection on the circle for this state occurs at a point where a tangent to the circle will be almost vertical. This means that if the width of the well were changed, the shift in the bound state would be very small. If the well was very thin such that $\pi/L_z \gg \gamma$, we would only have one bound state in the well and the energy of that state would be near the top to the well. In this case, a large change in L_z would only produce a small shift in the energy, as shown in Figure 6.
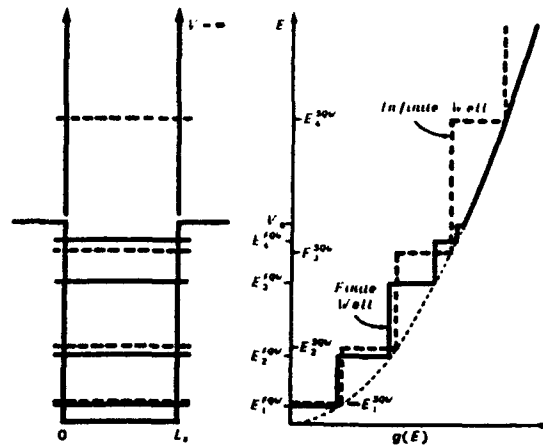
Figure 5. Comparison of energy states and DOS for an infinite single quantum well (SQW) and a finite quantum well (FQW). Notice that the energies of the states in the finite well are no longer inversely proportional the well width, and the DOS is not inversely proportional to the square of the width.

Note that in this case, the DOS for a thin well has nearly the same DOS as a well twice as big as the first. This is contrary to the infinite well case, where the DOS of the first state of the thinner well is four times as great as the DOS of a well that is twice as wide! The consequence is that in a real system with very thin wells, calculations which depend on the density of states, such as the capture or emission of charge carriers, become less dependent on the width of the well. In this case, other factors such as the spatial extent of the wavefunction become more important.[8]

Superlattices

When two finite quantum wells are placed near each other such that the barrier between them is small enough to allow interaction between the wells, the degenerate states split into two bound states of nearly the same energy. If this multiple quantum well arrangement were extended to many wells placed together, then the energy levels broaden into bands, much like the energy bands of the host crystal which are due to the periodicity of the atomic lattice. The differences are that the quantum well lattice is one dimensional with a period several times greater than that of the crystal, and the energy bands due to the coupled wells are superimposed onto the allowed energy bands of the host.

Such a structure, first proposed by Esaki and Tsu in 1969, is called a superlattice due to the periodic potential superimposed on the crystal's periodic potential, which gives rise to a new band structure.[9] The new potential is due to an array of square wells of width L_z, separated by barriers of width L_b and height U_0.

Applying the tight-binding approximation to the new periodic potential, the superlattice energy bands can be calculated. For the periodic superlattice potential
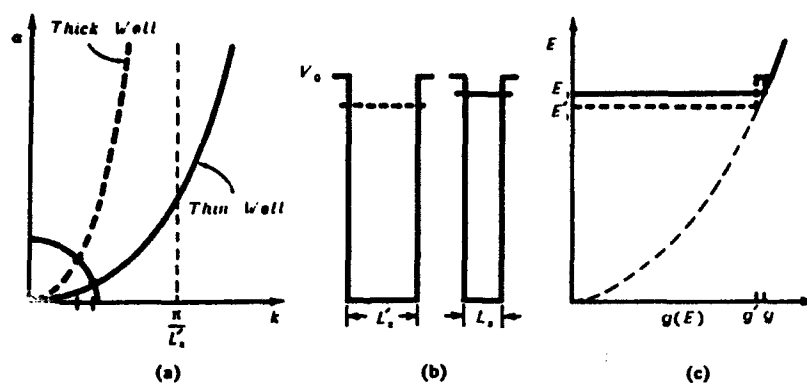
Figure 6. (a) Graphical solution for well with $2L_x = L'_x$, $\gamma \ll \pi/L'_x$, (b) Single bound state for both wells, and (c) The DOS for the corresponding wells. Notice that the DOS of the thin well is *not* four times that of the thick well. In fact, for ultra-thin wells, the DOS of both wells may be nearly equal.

$U(z) = U(z - nd)$, where d is the period of the superlattice, $L_x + L_b$, and n is an integer, the energies can be found using[10]

$$E = E^{SL} = \frac{\langle \psi_n | \mathcal{H}^{SL} | \psi_m \rangle}{\langle \psi_n | \psi_m \rangle} \qquad (19)$$

where

$$\mathcal{H}^{SL} = \left\{ -\frac{\hbar^2}{2m} \frac{\partial^2}{\partial z^2} + U(z) \right\} \qquad (20)$$

and

$$\psi_{n(m)}^{SL} = \sum_{n=1}^{N} e^{ik_z d} \psi^{FQW}(z - nd) \qquad (21)$$

for N wells. Solving (19) yields

$$E^{SL} = E^{FQW} - \alpha - \beta(e^{ik_z d} + e^{-ik_z d})$$

$$= E^{FQW} - \alpha - 2\beta \cos(k_z d) \qquad (22)$$

where

$$\alpha = \int_z (\psi^{FQW}(z))^* U(z) \psi^{FQW}(z) dz \quad , \quad (23)$$

which is the shift from E^{SQW} due to the coulombic interaction of the coupled wells, and β is the exchange energy which determines the extent of the band broadening, and is given by

$$\beta = \int_z (\psi^{FQW}(z - d))^* U(z) \psi^{FQW}(z) dz \quad . \quad (24)$$

assuming appreciable interaction from adjacent wells only. The important thing to note about α and β is that as the barrier width decreases, the interaction

between wells should increase, and thus α and β should increase.

The energy bands of a superlattice, as shown in Figure 7(a), can be found using Equation (19) with the total energy written as

$$E = E^{SL} + \frac{\hbar^2}{2m^*}(k_x^2 + k_y^2)$$

$$= E_0 - 2\beta \cos(k_z d) + \frac{\hbar^2}{2m^*}(k_x^2 + k_y^2) \qquad (25)$$

where $E_0 = E^{FQW} - \alpha$. The divergence of the total energy with respect to the wavevector is

$$\nabla_k E = 2d\beta \sin(k_z d)\hat{z} + \frac{\hbar^2}{m^*}(k_x \hat{x} + k_y \hat{y}) \quad ,$$

so the magnitude is then

$$|\nabla_k E| = \sqrt{4d^2\beta^2 \sin^2(k_z d) + \left(\frac{\hbar^2}{m^*}\right)^2 (k_x^2 + k_y^2)} \qquad (26)$$

The differential surface area of the constant energy surface is given by Equation (5). Recall that the differential change in energy of a *constant* energy surface is zero, so we can relate dk to dk_x. Let $k^2 = k_x^2 + k_y^2$, then $dE = 0$ becomes

$$dE = 0 = 2\beta d \sin(k_z d) dk_z + \frac{\hbar^2}{m^*} k dk \quad ,$$

so

$$dk = -\frac{2m^*\beta d}{\hbar^2 k} \sin(k_z d) dk_z \quad . \qquad (27)$$

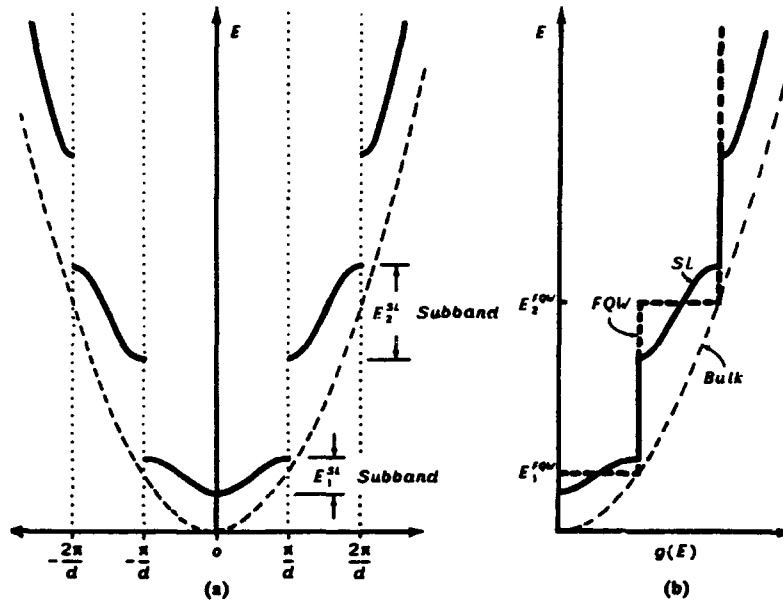The differential surface area of Equation (5) then becomes

Figure 7. (a) Dispersion relation for a superlattice, and (b) DOS for a superlattice versus single well and bulk. Because the interaction between wells causes the bound states to broaden into bands, the DOS is no longer constant as with the finite well, but it does retain a step-like nature.

$$dS = kd\phi \sqrt{\left(\frac{2m^*\beta d}{\hbar^2 k}\right)^2 \sin^2(k_z d)(dk_z)^2 + (dk_z)^2} \quad (28)$$

which, using Equation (26), can be re-written as

$$dS = d\phi dk_z \frac{m^*}{\hbar^2}\sqrt{4d^2\beta^2\sin^2(k_z d) + \left(\frac{\hbar^2}{m^*}\right)^2 k^2}$$

$$= d\phi dk_z \frac{m^*}{\hbar^2}|\nabla_k E| \quad (29)$$

Putting this in the DOS Equation (1), we get

$$g_3^{sl}(E) = \frac{1}{4\pi^3}\int \frac{dS}{|\nabla_k E|}$$

$$= \frac{1}{4\pi^3}\frac{m^*}{\hbar^2}\int_{-k_z}^{k_z}\int_0^{2\pi}\frac{|\nabla_k E|}{|\nabla_k E|}d\phi dk_z$$

$$= \frac{m^*}{4\pi^3\hbar^2}2\pi\int_{-k_z}^{k_z}dk_z$$

$$= \frac{m^*}{2\pi^2\hbar^2}\;2\int_0^{k_z}dk_z$$

$$= \frac{m^*}{\pi^2\hbar^2}k_z, \quad (30)$$

which is the same as Equation (8). The next step is to solve for k_z, but normalize the problem first by defining a dimensionless energy that is zero below the bottom of a subband, and has a value of one for energies above the subband. Using Equation (25), and adding and subtracting 2β,

$$E = E_0 + \frac{\hbar^2 k^2}{2m^*} - \frac{1}{2}4\beta\cos(k_z d) + \frac{4\beta}{2} - 2\beta. \quad (31)$$

Rearranging,

$$\frac{E - E_0 - \frac{\hbar^2 k^2}{2m^*} + 2\beta}{4\beta} = \frac{1}{2}(1 - \cos k_z d) = \xi \quad (32)$$

where ξ is the new dimensionless energy. Now solving for k_z, we get

$$k_z = \frac{1}{d}\arccos(1 - 2\xi) \quad (33)$$

The DOS for a superlattice is then

$$g_3^{sl}(E) = \frac{m^*}{\pi^2\hbar^2 d}\begin{cases} 0 & : \xi < 0 \\ \arccos(1-2\xi) : & 0 \le \xi \le 1 \\ \pi & : \xi > 1 \end{cases} \quad (34)$$

which is shown in Figure 7(b). To express $g_3^{sl}(E)$ as $g_3^{sl}(\xi)$, we must note that

$$g_3^{SL}(E)dE = g_3^{SL}(\xi)d\xi \qquad (35)$$

and

$$d\xi = \frac{1}{4\beta}dE \qquad (36)$$

So Equation (35) becomes

$$g_3^{SL}(\xi)d\xi = g_3^{SL}(E)4\beta d\xi$$

or,

$$g_3^{SL}(\xi) = \frac{4\beta m^*}{\pi^2\hbar^2 d}arccos(1-2\xi): \quad 0\le\xi\le1 \qquad (37)$$

Recall that this analysis was for *each* subband, so we must modify the equation to represent the general case. From the superlattice dispersion relation (Figure 7(a)) we see that, along with Equation (33), that the general form of the wavevector is

$$k_z = \frac{n\pi}{d} + \frac{1}{d}arccos(1-2\xi_i) \qquad (38)$$

where n is the number of filled subbands, and ξ_i is the dimensionless energy of the ith subband where $i = n+1$ (recall that each ξ_i is unique since ξ_i depends on E^{FQW}, α and β, all of which change for different subbands). The total superlattice DOS is then

$$g_3^{SL}(E) = \frac{m^*}{\pi^2\hbar^2 d}[n\pi + arccos(1-2\xi_i)] \qquad (39)$$

for $0 < \xi_i < 1$. For energies that fall between the nth and i^{th} subband, we have

$$g_3^{SL}(E) = \frac{m^*}{\pi\hbar^2}\frac{n}{d}$$

$$= g_2(E)\frac{n}{d} \qquad (40)$$

which looks a lot like Equation (10) ($g_3^{SQW}(E)$), except that we have the factor of $1/d$ instead of $1/L_z$. This is because the superlattice DOS depends on the interaction of coupled wells in a periodic potential of period d, while the single quantum well DOS depends only on L_z since there is no interaction from other wells.

Equivalence of DOS Expressions

The single quantum well DOS derived earlier should reduce to the 3D DOS if the well width is allowed to go to infinity. As an example of this, let us find the number of electrons per unit volume in a quantum well of a non-degenerate semiconductor (i.e., let the conduction band energy, E_c, be greater than a few k_BT above the Fermi energy, E_f). The solution should be equivalent to the electron density found

when the 3D DOS is used for the bulk semiconductor case. The expression for the electron density is[11]

$$\frac{N}{V} = n_e = \int_{E_c}^{E_{max}} g_3^{SQW}(E - E_c)f_{FD}(E)dE \qquad (41)$$

where $f_{FD}(E)$ is the Fermi-Dirac distribution function, which can be approximated by the Maxwell-Boltzmann distribution function, $f_{MB}(E)$, for a non-degenerate semiconductor where $E_c - E_f$ is greater than a few k_BT, or

$$f_{FD}(E) = \frac{1}{1 + e^{(E-E_f)/k_BT}}$$

$$= e^{-(E-E_f)/k_BT} = f_{MB}(E) \qquad (42)$$

So the electron density, n_e, is then

$$n_e = \int_{E_c}^{E_{max}} \frac{m^*}{\pi\hbar^2}\frac{n}{L_z}e^{-\frac{(E-E_f)}{k_BT}}dE$$

$$= \frac{m^*}{\pi\hbar^2 L_z}e^{\frac{E_f}{k_BT}}\int_{E_c}^{E_{max}} ne^{-\frac{E}{k_BT}}dE \qquad (43)$$

Notice that n is a function of E that increases by one for each additional bound state. For the bottom of each step in the DOS curve, let $E - E_c = E_n$, and let $(E_{max} - E_c) \gg k_BT$, and take the contribution of each bound state separately, as in Figure 8,

$$n_e = A + B + \dots$$

$$= \frac{m^*}{\pi\hbar^2 L_z}[e^{\frac{E_f}{k_BT}}\int_{E_1}^{\infty} e^{-\frac{E}{k_BT}}dE$$

$$+ e^{\frac{E_f}{k_BT}}\int_{E_2}^{\infty} e^{-\frac{E}{k_BT}}dE + \dots]$$

$$= \sum_n \frac{m^*}{\pi\hbar^2 L_z}e^{\frac{E_f}{k_BT}}\int_{E_n}^{\infty} e^{-\frac{E}{k_BT}}dE \qquad (44)$$

or

$$n_e = \sum_n \frac{m^* k_BT}{\pi\hbar^2 L_z}e^{-\frac{(E_n-E_f)}{k_BT}}$$

$$= \left[\frac{m^* k_BT}{\pi\hbar^2 L_z}\sum_n e^{-\frac{(E_n-E_c)}{k_BT}}\right]e^{-\frac{(E_c-E_f)}{k_BT}}$$

$$= N_c^{SQW}e^{-\frac{(E_c-E_f)}{k_BT}} \qquad (45)$$

where N_c^{SQW} is the effective DOS for the conduction band electrons in a quantized system. As L_x grows large, the bound states will drop toward E_c, and will eventually form an energy band, as in the bulk material. When this happens, we can say that the number of bound states in the band is large (note in Equation (10) that $L_x \propto n$), so as L_x goes to infinity, n also goes to infinity, and we should get the same N_c as for the 3D bulk case. In the limit of the sum going to an integral,

$$\sum_n e^{-\frac{(E_n - E_c)}{k_B T}} = \int_0^\infty e^{-\frac{(E_n - E_c)}{k_B T}} dn$$

$$= \int_0^\infty e^{-\frac{\pi^2 \hbar^2}{2m^* L_x^2 k_B T} n^2} dn$$

$$= \sqrt{\frac{\pi}{2}} \cdot \sqrt{\frac{2m^* L_x^2 k_B T}{\pi^2 \hbar^2}} . \qquad (46)$$

Substituting Equation (46) into N_c^{SQW} gives

$$N_c^{SQW} = \left(\frac{m^* k_B T}{\pi \hbar^2 L_x}\right) L_x \sqrt{\frac{m^* k_B T}{2\pi \hbar^2}}$$

$$= 2\left(\frac{m^* k_B T}{2\pi \hbar^2}\right)^{\frac{3}{2}} , \qquad (47)$$

which is exactly the value for the bulk case, where[11]

$$N_c^{BULK} = 2\left(\frac{m^* k_B T}{2\pi \hbar^2}\right)^{\frac{3}{2}} . \qquad (48)$$

Since Equations (47) and (48) are equivalent, $N_c^{SQW} = N_c^{BULK}$ in the limit as L_x goes to infinity. This is equivalent to saying that the general 2D DOS is the same as for the bulk case in this limit since the only difference between these expressions is the DOS functions used at the start of their derivations.

To see how Equation (40) for the superlattice DOS relates to the single quantum well case, $g_3^{SQW}(E)$, we must move the wells of the superlattice apart ($L_b \to \infty$), which removes their interaction. This results in α and β both going to zero, so Equation (25) becomes

$$E = E^{SQW} + \frac{\hbar^2 k^2}{2m^*}$$

$$= \frac{\pi^2 \hbar^2 n^2}{2m^* L_x^2} + \frac{\hbar^2 k^2}{2m^*}$$

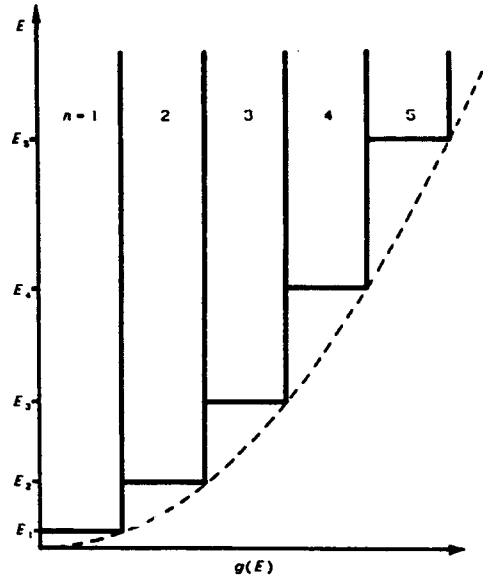$$= \frac{\hbar^2}{2m^*}\left(\frac{\pi^2 n^2}{L_x^2} + k^2\right)$$

Figure 8. The DOS near the bottom of a wide quantum well. The contribution of electrons from each bound state is found when each element of the DOS is integrated with the distribution function, giving the total number of electrons as the sum of each contribution.

$$= \frac{\hbar^2}{2m^*}(k_z^2 + k^2) , \qquad (49)$$

which means that $k_z = n\pi/L_x$ in the limit of large barriers. Using this wavevector in Equation (31), we get

$$\lim_{L_b \to \infty} g_3^{SL}(E) = \frac{m^*}{\pi^2 \hbar^2} \frac{n\pi}{L_x}$$

$$= \frac{m^*}{\pi \hbar^2} \frac{n}{L_x}$$

$$= g_3^{SQW}(E) \qquad (50)$$

Similarly, to show how the superlattice DOS relates to the bulk case, $g_3(E)$, we can either let L_b vanish, or let L_x go to infinity. If L_b gets small, the coupling between the wells get stronger, and the subbands broaden until the steps in the E vs $g_3^{SL}(E)$ curve merge and form a continuous parabolic curve. Note that the symmetrical shape of the steps in Figure 7(b) are arc cosine functions, which is due to the assumption that only nearest-neighbor interactions contribute in the tight-binding theory. For very strong coupling, however, wells beyond the nearest neighbors must be considered since the spatial extent of the electron wavefunctions become large. This apparent failure of the tight binding method[12] will result in the loss of the arc cosine symmetry of the steps, and should allow the

shape of the steps to conform more to the parabolic bulk case.

If, however, we let L_z get large, the carrier wavefunction will be more confined in the wells, which reduces the coupling and causes the subbands to narrow. But increasing L_z also has the effect of moving the subbands down in energy (remember that the subbands are nearly centered on the bound states of the single quantum well), which would cause then to stack up at the bottom of the wells. For a large well width, the steps in the E vs $g_3^{SL}(E)$ curve will become so small and numerous that they will form a quasi-continuous curve that will approach the bulk DOS case. In either case, the energy band would approach the bulk case, where $E(k)$ can be approximated by a parabolic curve, and k_z would become $k_z = \sqrt{2m^*E}/\hbar$. Using this intuitive analysis in Equation (38), we get

$$k_z = \frac{n\pi}{d} + \frac{1}{d}\cos^{-1}(1 - 2\xi_i) \approx \frac{\sqrt{2m^*E}}{\hbar} ,(51)$$

and Equation (39) becomes

$$g_3^{SL}(E) = \frac{m^*}{\pi^2\hbar^2} \cdot \frac{\sqrt{2m^*E}}{\hbar}$$

$$= \frac{\sqrt{2}(m^*)^{\frac{3}{2}}}{\pi^2\hbar^3}\sqrt{E} \qquad (52)$$

which is the 3D DOS given in Equation (11).

Conclusions

The derivation of the DOS function for quantum wells and superlattices is straight forward when approached with some insight into the physical constraints of these structures. The pure 2D infinite well case proved to be inadequate for the treatment of actual quantum well systems because it ignores the well width and higher-order bound states of the quantum well. The finite well case was obtained when the appropriate boundary conditions were applied. Special

care must be taken when analyzing very thin wells because the energy levels may or may not be strongly dependent on the well width. The superlattice DOS was then derived by considering the interaction of an array of finite quantum wells. Finally, we showed that each of the above cases is consistent with the others when the appropriate limits of well or barrier width are taken into account.

References

1. M. Krahl, J. Cristen, D. Bimberg, D. Mars, and J. Miller, "Impact of Well Coupling on the Spontaneous Emission Properties of GaAs/AlGaAs Multiple-Quantum-Well Structures," *IEEE J. Quantum Elect.*, QE-25, pp. 2281-8 (1989).
2. C. Kittel, *Introduction to Solid State Physics*, 6th ed., John Wiley and Sons, New York (1986), pp. 111-2.
3. R. H. Bube, *Electronic Properties of Crystalline Solids*, Academic Press, New York (1974), pp. 87, 172.
4. J. P. McKelvey, *Solid State and Semiconductor Physics*, Robert E. Krieger Publishing Company, Inc., Malabar, FL (1966), p. 85.
5. C. Kittel, *ibid.*, p. 133.
6. *ibid.*, p. 128.
7. J. P. McKelvey, *ibid.*, pp. 88-91.
8. R. M. Kolbas, Y. C. Lo and J. H. Lee, "Laser Properties and Carrier Collection in Ultrathin Quantum-Well Heterostructures," *IEEE J. Quantum Elect.*, QE-26, pp. 25-31 (1990).
9. L. Esaki and R. Tsu, "Superlattice and Negative Differential Conductivity in Semiconductors," *IBM J. Res. Develop.*, 14, 61 (1970).
10. C. M. Wolf, N. Holonyak, Jr., and G. E. Stillman, *Physical Properties of Semiconductors*, Prentice Hall, Englewood Cliffs, NJ (1989), pp. 47-9.
11. C. Kittel, *ibid.*, p. 202.
12. N. W. Ashcroft and N. D. Mermin, *Solid State Physics*, Saunders, Orlando, FL (1976), pp. 184-5.

Surface and bulk leakage currents in transverse junction stripe lasers

Yongkun Sin, K. Y. Hsieh, J. H. Lee, and R. M. Kolbas
Department of Electrical and Computer Engineering, North Carolina State University, Raleigh, North Carolina 27695-7911

This paper presents two ways to reduce leakage currents in transverse junction stripe (TJS) lasers: by reducing surface leakage current and by reducing bulk leakage current. The surface leakage is reduced by treatment with $(NH_4)_2S$, while the bulk leakage current is reduced by isoelectronic doping with indium. We report the first detailed experimental investigation on the effect of the chemical treatments on the electrical characteristics and laser thresholds of TJS lasers. Surface treatments of $(NH_4)_2S$ are demonstrated that reduce surface leakage currents in current injection lasers. After the chemical treatments, a 20-fold reduction in current has been achieved with GaAs/AlGaAs lattice-matched multiple-quantum-well TJS lasers. The laser thresholds of lattice-matched TJS lasers are reduced by 12 mA (or 16%) after the chemical treatments. In addition, InGaAs-GaAs-AlGaAs strained-layer single-quantum-well lasers are treated chemically and a reduction in the laser threshold (10 mA or 14%) is observed. The surface treatments are still effective after 7 days. We also report the first experimental investigation on the effect of isoelectronic In doping on the current-voltage characteristics of Zn-diffused lateral *p-n* junctions. The trap density in an In-doped AlGaAs layer is reduced by more than one order of magnitude compared to that in an AlGaAs layer without In doping. Bulk leakage currents (shunting currents) in TJS lasers can be reduced by using isoelectronic In doping, which should reduce threshold currents and improve the temperature dependence of TJS lasers.

I. INTRODUCTION

Transverse junction stripe (TJS) lasers have several desirable characteristics which include low threshold currents,[1] good output beam characteristics,[2] and a single growth step on a semi-insulating substrate suitable for integration with electrical components.[3,4] In addition to a conventional AlGaAs active region, TJS lasers have been demonstrated with single and multiple quantum wells of lattice-matched AlGaAs-GaAs and pseudomorphic InGaAs-GaAs-AlGaAs.[5,6] Unfortunately, many laboratories have had difficulty fabricating and reproducing high-quality TJS lasers.

Leakage currents can significantly degrade the performance of TJS lasers compared to other semiconductor lasers owing to the required (but often not achieved) forward-biased blocking junction in the wide-gap confining layers. In this paper the role of surface and bulk leakage currents are identified, measured, and modified to improve the performance of TJS lasers. Section II discusses experiments on reduction of surface leakage current, while Sec. III discusses reduction of bulk leakage currents.

II. SURFACE LEAKAGE CURRENTS

A. Introduction

The presence of a large density of surface and interface states has been an obstacle to the development of GaAs devices with desirable performance. The Fermi-level pinning greatly increases the nonradiative recombination rate at surface recombination centers, and this surface recombination current limits the performance of minority-carrier devices such as lasers, light-emitting diodes, and heterojunction bipolar transistors (HBTs). Several approaches have been suggested to remove or reduce surface/interface states in GaAs/AlGaAs.[7-9] One novel way is to use Na_2S or $(NH_4)_2S$ chemical treatments. This technique was employed to dramatically improve the performance of a HBT (a 60-fold increase in the current gain was observed with the Na_2S-$9H_2O$ treatment).[10] Reductions by a factor of 3.2 in edge recombination currents using the Na_2S and $(NH_4)_2S$ chemical treatments were obtained for GaAs vertical *p-n* homojunctions.[11] A significant improvement in metal-insulator-semiconductor (MIS) capacitance-voltage (*C-V*) characteristics with the $(NH_4)_2S$-treated GaAs was observed,[12] and the same treatment caused a remarkable dependence of the Schottky barrier height on the work function of the deposited metals.[13] Characterizations of bulk and epitaxial GaAs treated with Na_2S or $(NH_4)_2S$ by photoluminescence (PL),[14] surface conductivity technique,[15] deep-level transient spectroscopy (DLTS),[16] and Raman scattering[17] have been reported. Dramatic results from such treatments have been demonstrated including an increase in GaAs PL efficiency at 300 K of 2800 times using Na_2S-$9H_2O$,[14] and a reduction in surface recombination velocity from $\sim 10^6$ to 500 cm/s.[18]

In this section, we demonstrate that a dramatic surface leakage current reduction is possible with $(NH_4)_2S$ chemical treatments for TJS lasers. $(NH_4)_2S$ was chosen to avoid some problems associated with using Na_2S (e.g., fast aging in ambient air and the introduction of surface conduction[11]).
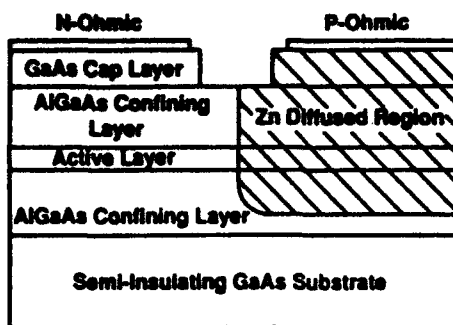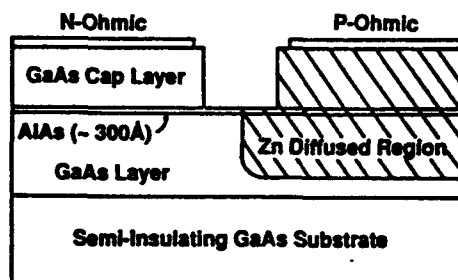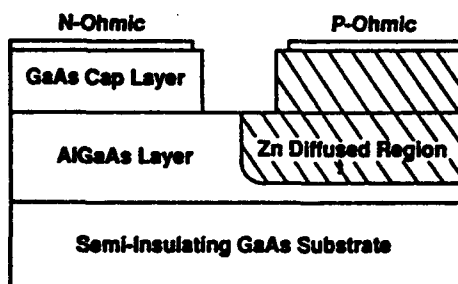
FIG. 1. Schematic cross section of a transverse junction stripe (TJS) laser. A two-step diffusion and annealing process (Zn diffusion followed by high-temperature annealing) is employed and a portion of the GaAs cap layer is etched for electrical isolation.

B. Experimental procedures

After examining several samples, four were selected to summarize the results of the surface passivation. The samples consist of leakage current test structures [(LCTS) which are lateral p-n junctions] and TJS laser structures. Schematic cross sections of the completed devices (both TJS and LCTS) are shown in Figs. 1 and 2(a) and 2(b), respectively. LCTS No. 1, No. 2, and TJS No. 1 were grown by molecular-beam epitaxy (MBE) and TJS No. 2 was grown by metalorganic chemical vapor deposition (MOCVD). LCTS No. 1 consists of GaAs:Si (2×10^{18}/cm^3, 1.5 μm, 627 °C), an AlAs stop etch layer (undoped, 300 Å, 627 °C), and a GaAs:Si cap layer (2×10^{18}/cm^3, 0.5 μm, 627 °C) de-

posited on a semi-insulating GaAs:Cr substrate. LCTS No. 2 consists of Al$_{0.35}$Ga$_{0.65}$As:Si (10^{17}/cm^3, 3 μm, 686 °C) and a GaAs:Si cap layer (2×10^{18}/cm^3, 0.5 μm, 627 °C) deposited successively on a semi-insulating GaAs:Cr substrate. TJS No. 1, a strained-layer laser, is shown schematically in Fig. 3(a) and the growth and processing details can be found in Ref. 6. TJS No. 2, grown by MOCVD, consists of an Al$_{0.38}$Ga$_{0.62}$As lower cladding layer (Te: ~2×10^{17}, 3.2 μm), a multiple-quantum-well (MQW) active region GaAs (Te: 2.5×10^{18})/Al$_{0.2}$Ga$_{0.8}$As (Te: ~2×10^{17}) (14 periods, both layers~150 Å), an Al$_{0.38}$Ga$_{0.62}$As (Te: ~2×10^{17}/cm^3, 1.1 μm) upper cladding layer, and a GaAs (Te: 2.5×10^{18}, 0.36 μm) cap layer on a semi-insulating

FIG. 2. (a) Schematic cross section of a GaAs leakage current test structure (LCTS). The sample undergoes the same processing steps as a TJS laser. The 300-Å-thick AlAs is used as a stop etch layer. (b) Schematic cross section of an AlGaAs LCTS. Unlike the GaAs LCTS sample, an AlAs stop etch layer is not necessary for this sample. Both samples are grown on semi-insulating GaAs substrates.

FIG. 3. (a) Schematic diagram of the layer structure and composition of InGaAs-GaAs-AlGaAs strained-layer MQW TJS laser. The 0.2-μm-thick active layer consists of four QWs and three Al$_{0.7}$Ga$_{0.3}$As barriers. Each of the 50-Å-thick In$_{0.15}$Ga$_{0.85}$As QWs is sandwiched by 125 Å of GaAs. (b) Schematic diagram of the layer structure and composition of lattice-matched GaAs-AlGaAs MQW (14 QWs) TJS laser. The 0.4-μm-thick active layer consists of 14 (150-Å-thick) GaAs QWs sandwiched by 15 (150-Å-thick) Al$_{0.2}$Ga$_{0.8}$As barriers.

GaAs:Cr substrate. A schematic diagram of the as-grown lattice-matched laser (TJS No. 2) is shown in Fig. 3(b).

The diffused p-n junction was formed as follows. Silicon nitride (about 1500 Å thick, refractive index of approximately 2.1) was deposited by plasma-enhanced chemical vapor deposition (PECVD). Standard photolithography was employed to define stripe patterns. Zinc was diffused into the region (Si_3N_4 uncovered) by a sealed ampoule technique ($ZnAs_2$ as a Zn diffusion source, As overpressure). The diffusion temperatures were fixed at 650 °C for all of the samples. After the Zn diffusion the Si_3N_4 was removed and a new Si_3N_4 layer was deposited as an annealing encapsulant. High-temperature annealing was done under As overpressure with the same sealed ampoule technique. Table I summarizes processing conditions used for the samples employed to study surface leakage currents. Subsequently, the Si_3N_4 was etched away and a portion of GaAs cap layer (about 6 μm wide) was etched for electrical isolation. Next, the ohmic contacts were deposited. For LCTS No. 1 and No. 2, Au-Sn-Au (100 Å-200 Å-1000 Å) and Cr-Au (200 Å-1000 Å) were thermally evaporated for n-ohmic and p-ohmic, respectively, while for TJS No. 2, AuGe-Au (350 Å-1500 Å) and Cr-Au (200 Å-1500 Å) were thermally evaporated for n-ohmic and p-ohmic, respectively. Finally, the samples were thinned down to about 100 μm and cleaved into bars (cavity length of approximately 250 μm).

The $(NH_4)_2S$ surface passivation was applied using the following procedure. First, the samples were cleaned in a HCl solution for 20 s, rinsed in de-ionized (DI) water for 20 s, etched in a mixture of NH_4OH + DI water (1:10) for 15 s, and rinsed in running DI water for 20 s. Then the samples were soaked in the $(NH_4)_2S$ solution for up to 10 min. The samples were then rinsed with DI water and blown dry with N_2.

C. Results and discussion

Schematic cross sections of the completed devices (both TJS and LCTS) are shown in Figs. 1 and 2(a) and 2(b), respectively. Current-voltage characteristics were measured at room temperature (and extreme care was taken to minimize the measurement error to within ± 5 mV throughout this experiment). Plots of current [log(I)] versus voltage (V) both before and after the chemical treatments for LCTS
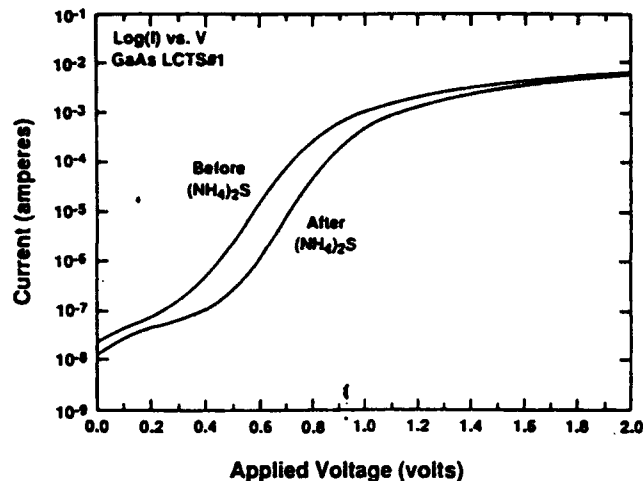

FIG. 4. Current-voltage characteristics of a GaAs leakage current test structure (LCTS No. 1) before and after the $(NH_4)_2S$ chemical treatments. An order of magnitude less current flows at 0.7 V after the treatment.

No. 1, LCTS No. 2, TJS No. 1, and TJS No. 2 are shown in Figs. 4, 5, 6, and 7, respectively.

The total forward current density for a p-n junction can be approximated by summing the ideal diffusion current density and recombination current density:

$$J = J_{01}(e^{qV/kT} - 1) + J_{02}(e^{qV/2kT} - 1), \qquad (1)$$

where J_{01} and J_{02} are the saturation current densities associated with carrier recombination in the quasi-neutral and space-charge regions, respectively. The second term of the above equation accounts for contributions from both bulk and surface recombination. Since an intense nonradiative recombination occurs at the perimeters of p-n junctions such as cleaved and etched surfaces, surface recombination must play an important role in determining the electrical characteristics and threshold currents of TJS lasers. In our samples, surface recombination occurs where a portion of the GaAs cap layer is removed for electrical isolation as well as where the cleaved mirrors are exposed to the air. These are the two major surface leakage sources for TJS lasers.

Surface recombination current per unit length at the perimeter of a p-n junction (I_s) can be described as follows[19]:

TABLE I. Processing conditions (Zn diffusion temperature and time, annealing temperature and time, and metal combinations for ohmic contacts) used for both leakage current test structure (LCTS) samples and transverse junction stripe (TJS) laser samples (strained-layer MQW TJS, lattice-matched MQW TJS, and conventional TJS) employed to study surface leakage currents.

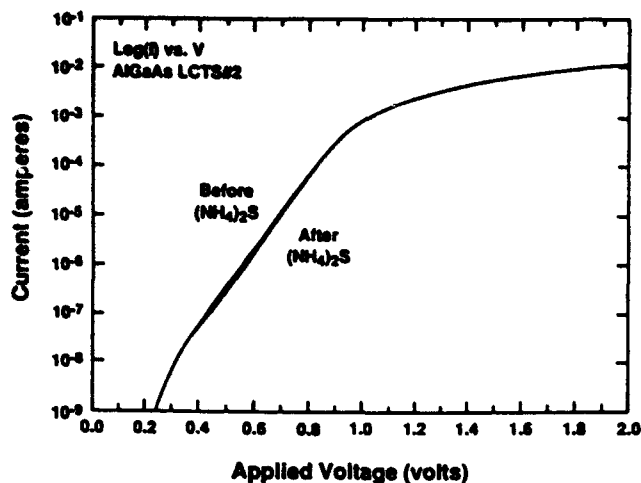| Structures | Zn diffusion | | Annealing | | Metallization | |
	Temp. (°C)	Time (h)	Temp. (°C)	Time (h)	n-ohmic	p-ohmic
GaAs LCTS No. 1	650	1.6	900	2.0	Au-Sn-Au	Cr-Au
AlGaAs LCTS No. 2	650	1.6	900	2.0	Au-Sn-Au	Cr-Au
SL MQW TJS No. 1	650		900	0.3	Au-Sn-Au	Au-Cr-Au
MQW TJS No. 2	650	2.0	900	0.3	AuGe-Au	Cr-Au
Conventional TJS No. 3	650	11.0	850	0.4	AuGe-Au	Cr-Au

FIG. 5. Current-voltage characteristics of an AlGaAs leakage current test structure (LCTS No. 2) before and after the $(NH_4)_2S$ chemical treatments. Note that there is almost no difference in the I-V curves.

$$I_s = q(S_0 L_s)n_i \exp(qV/2kT), \qquad (2)$$

where n_i is intrinsic carrier concentration, S_0 the intrinsic surface recombination velocity, and L_s the surface diffusion length. Note in Figs. 4 and 5 that LCTS No. 2 $(Al_{0.35}Ga_{0.65}As)$ shows almost no change with surface treatment [also no change observed with the MOCVD-grown LCTS sample $(Al_{0.34}Ga_{0.66}As)$ (data not shown here)], while an order of magnitude reduction (from 8.5×10^{-5} to 8.5×10^{-6} A) was measured with LCTS No. 1 (GaAs) after the treatment (at bias $= 0.7$ V). From Eq. (2), I_s is proportional to the intrinsic carrier concentration, so we can roughly calculate the amount of surface leakage current of LCTS No. 2 assuming (1) $N_D = 2 \times 10^{18}$ and $N_A \approx 10^{19}$ for LCTS No. 1 and $N_D = 10^{17}$ and $N_A \approx 10^{19}$ for LCTS No. 2, (2) the same $S_0 L_s$ and bias levels, and (3) I_s
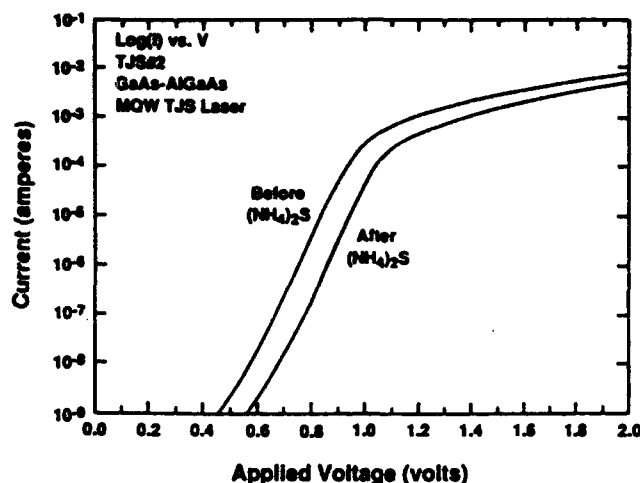

FIG. 6. Current-voltage characteristics of an InGaAs-GaAs-AlGaAs strained-layer MQW TJS laser (TJS No. 1) before and after the $(NH_4)_2S$ chemical treatments. An eightfold reduction in current occurs at 1.1 V after the treatment.

FIG. 7. Current-voltage characteristics of lattice-matched GaAs-AlGaAs MQW TJS laser (TJS No. 2) before and after the $(NH_4)_2S$ chemical treatments. 20 times less current flows at 0.9 V after the treatment.

$(GaAs) = 8.5 \times 10^{-5}$ A $- 8.5 \times 10^{-6}$ A $= 7.75 \times 10^{-5}$ A at 0.7 V.

Since $n_i(Al_{0.35}Ga_{0.65}As)/n_i(GaAs) \approx 3.5 \times 10^{-4}$, $I_s(Al_{0.35}Ga_{0.65}As) \approx (3.5 \times 10^{-4}) \times I_s(GaAs) \approx 2.7 \times 10^{-8}$ A. This value is so small that surface leakage currents in $Al_{0.35}Ga_{0.65}As$ can be neglected as can be seen from the data in Fig. 5. From this comparison, the majority of the improvement likely occurs at the cleaved interface since the surface passivation is most effective on the GaAs and LCTS No. 1 has a top p-n junction surface of AlAs.

Surface leakage current reductions were also observed with TJS No. 1 and TJS No. 2. After the treatment, an eight-fold reduction (from 8×10^{-5} to 10^{-5} A at 1.1 V, Fig. 6) and around a 20-fold reduction (from 5×10^{-5} to 2.5×10^{-6} A at 0.9 V, Fig. 7) in current were measured for TJS No. 1 and TJS No. 2, respectively. The greater reduction in leakage current for TJS No. 2 (~ 2.5 times) compared to TJS No. 1 correlates with the effective perimeter of the p-n junctions (only accounting for the lower-energy band-gap materials such as GaAs and InGaAs) given that the perimeter of TJS No. 2 (GaAs QW ~ 150 Å, 150 Å $\times 14 = 2100$ Å) is approximately twice the perimeter of TJS No. 1 (GaAs + $In_{0.15}Ga_{0.85}As \sim 300$ Å, 300 Å $\times 4 = 1200$ Å).

The $(NH_4)_2S$ was also applied to the conventional MOCVD-grown TJS lasers (TJS No. 3) to determine its effect on laser thresholds. The laser structure with about a 4000-Å-thick GaAs active layer ($n^+ \approx 3 \times 10^{18}/cm^3$) underwent Zn diffusion for 11 h at 650 °C and annealing for 25 min at 850 °C (see Table I). The GaAs cap and $Al_{0.35}Ga_{0.65}As$ upper confining layer thicknesses of this structure were 2.4 and 2.2 μm, respectively. The light-current curves for device No. 4 of TJS No. 3 before and after the chemical treatment are shown in Fig. 8. A reduction of 15 mA (from 79 to 64 mA) in laser threshold was observed. Other devices from the same wafer were also surface treated and similar trends were obtained. Table II summarizes the experimental results for TJS lasers. The average reduction in laser threshold was 12 mA (or 16%) for the seven devices
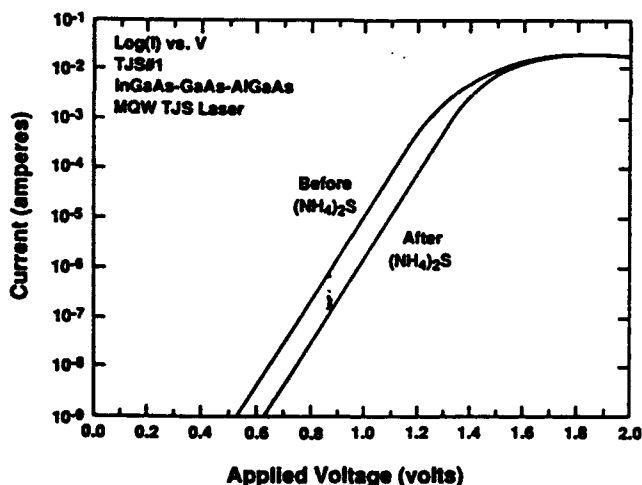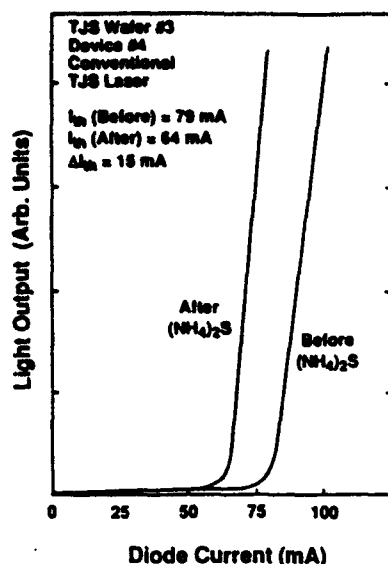
FIG. 8. Light-current characteristics of a conventional TJS laser (TJS No. 3, device No. 4) before and after the $(NH_4)_2S$ chemical treatments. A reduction in laser threshold of 15 mA is obtained.

tested. The light output versus current (L-I) curves for device No. 7 of TJS No. 3 measured before and after the surface treatments at two different times ($T_2 - T_1 = 7$ days, T_1 is several hours after the treatment) are shown in Fig. 9(a). Note that the chemical treatment is still effective after 7 days. The effects of stripping the chemical treatment are shown in Fig. 9(b) for the same device (device No. 7). Curve 1 is before the chemical treatment, curve 2 is after the treatment, and curve 3 is after stripping the chemical simply by dipping the device in acetone for about 10 min. When the chemical was removed from the treated device, almost the same laser threshold of the untreated device was obtained. The effects of retreating device No. 7 are shown in Fig. 9(c). Curve 1 is before stripping the chemical from the device, curve 2 is after stripping the chemical, and curve 3 is after retreating the device. When the device that had been stripped was treated again, the same reduction in laser threshold was observed. This experiment confirms that the reduction in laser threshold after the surface treatments is really due to reduced or removed surface leakage currents

from laser diodes. Also, note that a reduction in laser threshold of an AlGaAs laser diode by the same chemical treatments was observed by another group.[20]

In addition, strained-layer laser diodes were also surface treated chemically. A separate confinement heterostructure single-quantum-well (SCH SQW, 40-Å-thick $In_{0.2}Ga_{0.8}As$ QW sandwiched between 450-Å-thick GaAs) laser structure was grown by MBE, and a spin-on-glass film was employed to define stripes (stripe width $\sim 6\,\mu m$). The size of the completed devices was $200 \times 250\,\mu m^2$. The L-I curves for device No. 6 before and after the chemical treatment are shown in Fig. 10. A reduction of 8 mA in laser threshold was obtained. Curves 1 and 2 are before the surface treatments at two different times ($T_2 - T_1 = 2$ days), and curve 3 is after the treatment. The fact that almost the same L-I curves were obtained before the treatments at two different times demonstrates that the data obtained here were not due to reproducibility errors. The experimental results for the strained-layer laser diodes are summarized in Table II. The average reduction was 10 mA (or 14%) for the six devices tested. L-I data for devices No. 1, No. 3, and No. 4 were measured after the treatments at two different times ($T_2 - T_1 = 6$ days, T_1 is several hours after the treatment, data not shown here). Again, as in the case of the lattice-matched TJS lasers [see Fig. 9(a)], the L-I curves remained unchanged after 6 days. The effects of aging and the effects of stripping and retreating a strained layer laser (device No. 2) are shown in Figs. 11(a) and 11(b). Again, the reduction in laser threshold (this time using a strained-layer laser) is due to surface leakage current reduction or removal, and after dipping the surface treated device in acetone for around 30 min, the threshold current returned to nearly the untreated value.

III. BULK LEAKAGE CURRENTS

A. Introduction

The presence of bulk leakage currents is recognized as a significant factor in the initial performance and in the subsequent deterioration in the performance of both electronic and optoelectronic devices. The electrical and optical properties of GaAs and AlGaAs epitaxial layers are critical for

TABLE II. Improvements (ΔI_{th} and %) in laser thresholds of conventional TJS lasers and strained-layer SQW lasers by the $(NH_4)_2S$ treatments. I_{th} (Before) and I_{th} (After) denote threshold currents before and after the chemical treatments, respectively.

Laser types	Threshold current	No. 1	No. 2	No. 3	No. 4	No. 5	No. 6	No. 7
Conventional TJS lasers	I_{th} (Before)	68	76	75	79	79	79	77
(TJS No. 3)	I_{th} (After)	53	66	64	64	71	68	64
	$\Delta I_{th}{}^a$	−15	−10	−11	−15	−8	−11	−13
	%[b]	22	13	15	19	10	14	17
InGaAs-GaAs-AlGaAs	I_{th} (Before)	68	73	65	71	70	60	
SQW strained-layer	I_{th} (After)	57	63	55	62	60	52	
laser diodes	ΔI_{th}	−11	−10	−10	−9	−10	−8	
	%	16	14	15	13	14	13	

$^a \Delta I_{th} = I_{th}$ (After) $- I_{th}$ (Before).
$^b \% = [|\Delta I_{th}|/I_{th}$ (Before)] $\times 100$.

(a)

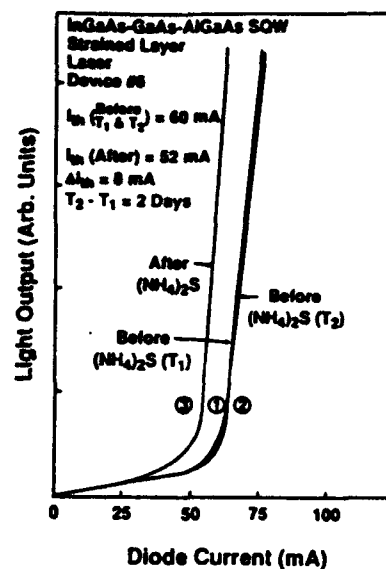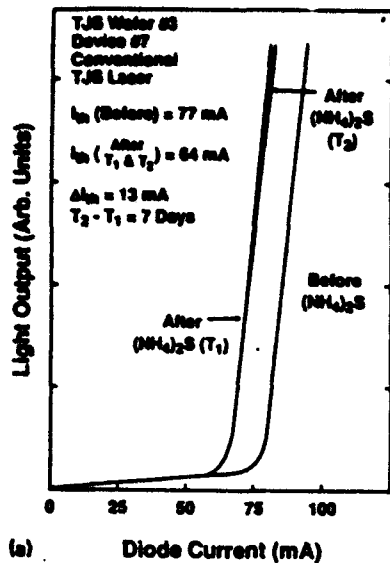Diode Current (mA)

Diode Current (mA)

FIG. 10. Light-current curves for InGaAs-GaAs-AlGaAs SQW strained-layer laser diode (device No. 6). The fact that the same laser thresholds are obtained at two different times ($T_2 - T_1 = 2$ days) before the treatment demonstrates that the reduction in laser threshold is not due to measurement errors. A reduction of 8 mA in laser threshold is obtained after the treatment.
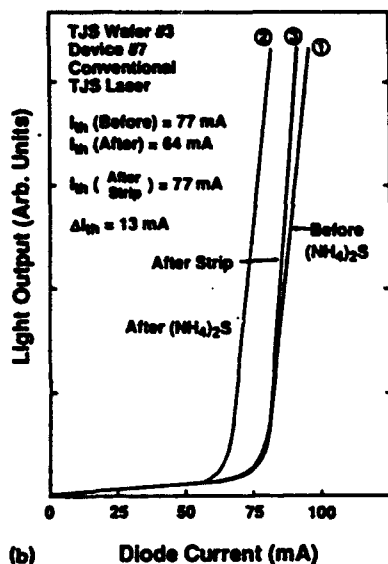

(b)

Diode Current (mA)

FIG. 9. (a) Light-current characteristics overlapped for conventional TJS laser (TJS No. 3, device No. 7) before and after the $(NH_4)_2S$ chemical treatments. A reduction of 13 mA in laser threshold is obtained. There is almost no difference in laser thresholds measured at two different times ($T_2 - T_1 = 7$ days) after the treatments. (b) Light-current characteristics for the same device as shown in (a). After stripping the chemical in acetone for ~10 min, the same laser threshold of the untreated device is obtained. (c) Light-current characteristics for the same device. After stripping and retreating, the same reduction is obtained.
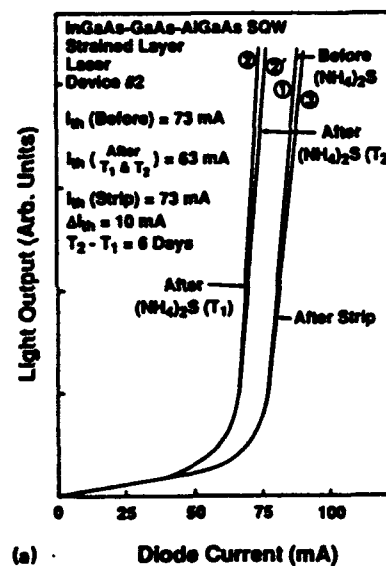

(a)

Diode Current (mA)

FIG. 11. (a) Light-current curves for a strained laser (device No. 2). The chemical reduces laser threshold by 10 mA. The same laser thresholds are measured at two different times ($T_2 - T_1 = 6$ days) after the treatment. After stripping the chemical in acetone for ~30 min, the same laser threshold of the untreated device is obtained. (b) Light-current curves for the same device (device No. 2). After stripping and retreating, the same reduction is obtained.

(c)

Diode Current (mA)

(b)

Diode Current (mA)
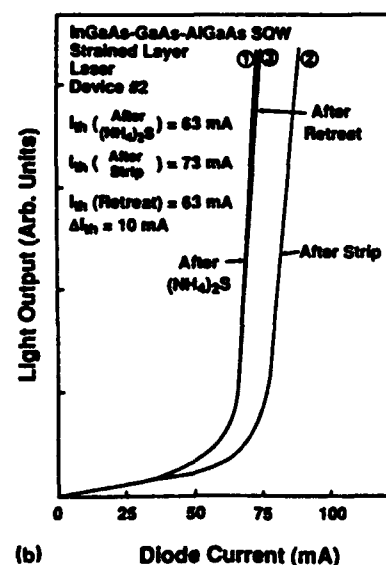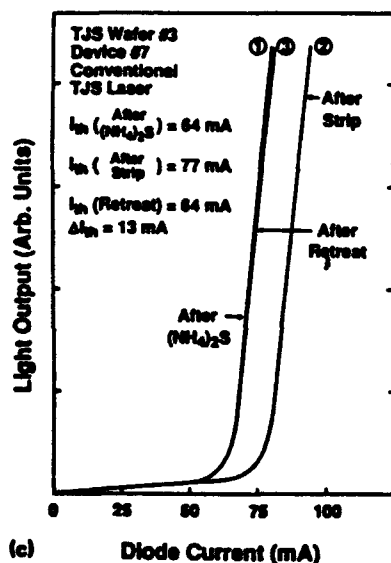
high performance of electronic and optoelectronic devices, but these properties can be dominated by deep levels in the epitaxial layers. The presence of deep levels has led to persistent photoconductivity effects in high electron mobility transistors (HEMT) at low temperatures[21] and high threshold currents in semiconductor lasers.[22,23] Several approaches have been suggested to reduce deep levels in GaAs and AlGaAs epitaxial layers. One approach is to use an isoelectronic doping technique. Incorporation of small amounts of In or Sb has been shown to reduce deep-level concentrations in liquid-encapsulated Czochralski (LEC) GaAs bulk crystals,[24] and in liquid-phase epitaxy (LPE) grown GaAs.[25] Also reported was that the addition of In (0.2%–1.2%) to GaAs grown by MBE reduces the trap concentrations from $1-4 \times 10^{14}/cm^3$ to the order of $1 \times 10^{13}/cm^3$,[26] and that isoelectronic In and Sb doping (up to 7%) reduces deep-level trap concentrations in Si-doped n-GaAs grown by MBE.[27] MBE AlGaAs alloys with low densities of point defects (deep levels less than $2 \times 10^{13}/cm^3$) have been produced by using Sb doping.[28] More recently, the structural and electrical contact properties of LPE-grown GaAs doped with In were reported to have improved Schottky diode characteristics.[29]

The presence of shunting currents (current paths through the AlGaAs confining layers) has been recognized as a primary cause of high threshold currents in TJS lasers. The ratio of the current through active layer (I_A) to that through confining layer (I_C) can be expressed by[30]

$$\frac{I_A}{I_C} = \frac{d}{W} \exp\left(\frac{\Delta E_g}{2kT}\right), \tag{3}$$

where d is the active layer thickness, W is the combined thickness of the two confining layers ($W = W_1 + W_2$, see Fig. 12), k is Boltzmann's constant, and ΔE_g is the effective-energy band-gap difference between the active and confining layers. ΔE_g is given by[31]

$$\Delta E_g = (kT/q) \ln(J_1/J_2) - (J_1 R_1 - J_2 R_2), \tag{4}$$

where J_1 and J_2 are the current densities that flow through each junction, R_1 and R_2 are the series resistances between the electrodes for the unit area of each junction, and 1 and 2 denote the GaAs p-n homojunction (active layer) and the AlGaAs p-n homojunction (confining layer, see Fig. 12), respectively. From the above equations, the layer thicknesses, the Al compositions, and the doping densities of each layer can be optimized to design a TJS laser with a low laser threshold. However, a lot of shunting currents still exist due to the large number of traps associated with the AlGaAs confining layers.

As shown in Fig. 12, TJS lasers can be modeled as AlGaAs p-n junctions (confining layers) and a GaAs p-n junction (active layer) connected in parallel. To simulate the active and confining layers of a TJS laser, leakage current test structures (lateral p-n junctions) are introduced. In order for TJS lasers to have low laser thresholds (with shunting currents reduced or removed), the AlGaAs junctions should remain off, while the GaAs junction is on at operating bias levels. The problems associated with an AlGaAs p-n homojunction are illustrated in Fig. 13. Even though the
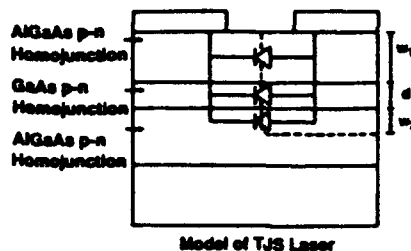

FIG. 12. Current flow model of a TJS laser consisting of a GaAs p-n homojunction (active layer) and AlGaAs p-n homojunctions (confining layers) connected in parallel. Resistance of the layers is not shown.

AlGaAs have a higher-energy band gap than the GaAs, they exhibit nearly the same turn-on voltages once they are processed into lateral p-n junctions. The objective is to find a way to increase the turn-on voltage of the AlGaAs p-n homojunction relative to the GaAs [Fig. 13(a)]. Similar turn-on voltages, as shown in Fig. 13(b), have been obtained from (1) $Al_{0.08}Ga_{0.92}As$ (n^+) and $Al_{0.35}Ga_{0.65}As$ (undoped), both MOCVD grown on undoped GaAs substrates (data not shown here),[32] and (2) $Al_{0.11}Ga_{0.89}As$ ($n^+ \sim 2 \times 10^{18}$) and $Al_{0.34}Ga_{0.66}As$ (undoped), both MOCVD grown on Cr-doped GaAs substrates (data not shown here).[33]

In this section, we report the electrical characterization of Zn-diffused lateral p-n junctions with and without In doping and demonstrate that deep level concentrations in the AlGaAs layer with Zn-diffused lateral p-n junctions are reduced by more than one order of magnitude with isoelectronic In doping.

B. Experimental procedures

For this experiment, three samples were grown by molecular-beam epitaxy (Varian 360). The samples consist of leakage current test structures (LCTS, which are lateral p-n junctions). LCTS No. 1 consists of GaAs:Si ($2 \times 10^{18}/cm^3$, 1.5 μm, 627 °C), an AlAs stop etch layer (undoped, 300 Å, 627 °C), and a GaAs:Si cap layer ($2 \times 10^{18}/cm^3$, 0.5 μm, 627 °C) deposited on a semi-insulating GaAs:Cr substrate. LCTS No. 2 consists of $Al_{0.35}Ga_{0.65}As$:Si ($10^{17}/cm^3$, 3 μm, 686 °C) and a GaAs:Si cap layer ($2 \times 10^{18}/cm^3$, 0.5 μm, 627 °C) deposited successively on a semi-insulating
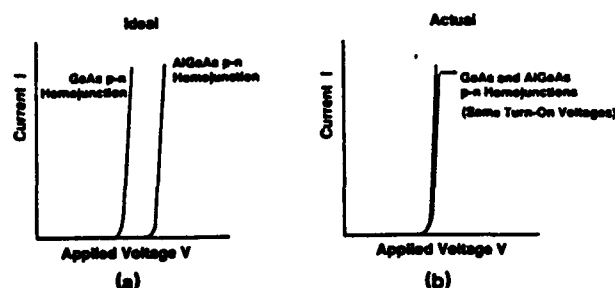

FIG. 13. (a) Ideal current-voltage curves for lateral p-n junctions. An AlGaAs p-n junction should show a higher turn-on voltage than a GaAs p-n junction. (b) Actual I-V curves for GaAs and AlGaAs p-n junctions showing the same turn-on voltages. This often occurs in many TJS lasers.

GaAs:Cr substrate. LCTS No. 3 consists of $Al_{0.35}Ga_{0.65}As:Si$ ($10^{17}/cm^3$, 3 μm, 686 °C) doped with In (~1 at. %) and a GaAs:Si cap layer ($2 \times 10^{18}/cm^3$, 0.5 μm, 627 °C) deposited on a semi-insulating GaAs:Cr substrate.

The same processing steps as described in Sec. II B were performed. Zn was diffused for 1 h and 15 min at 650 °C for all samples. The samples were annealed for 20 min at 850 °C. Two-step diffusion and annealing processes were optimized for LCTS No. 1 and No. 2 to have Zn diffusion fronts close to the substrate. Next, the ohmic contacts were deposited. Au-Ge/Au (350 Å-1500 Å) and Cr-Au (200 Å-1500 Å) were thermally evaporated for n-ohmic and p-ohmic, respectively. Finally, the samples were thinned down to 100 μm and cleaved into bars (cavity length of about 250 μm).

C. Results and discussion

The objective of this study was to find ways to reduce the bulk leakage currents (shunting currents) in Zn-diffused lateral p-n junctions in order to improve the laser thresholds and the temperature dependence of the laser thresholds. For this experiment, different background doping concentrations are used for GaAs (Si: $2 \times 10^{18}/cm^3$, LCTS No. 1) and $Al_{0.35}Ga_{0.65}As$ (Si: $10^{17}/cm^3$, LCTS No. 2 and No. 3) to simulate the active and confining layers of TJS lasers, respectively.

Cross sections of the completed devices are the same as those of devices described in Sec. II B and a schematic diagram is shown in Fig. 2. Current-voltage characteristics for the samples were measured both at room temperature and at 77 K. Current-versus-voltage data for the samples at room temperature and at 77 K are shown in Figs. 14 and 15, respectively. Zn-diffused junction depths (x_j) were measured to be 1.3 μm for LCTS No. 1, 2.6 μm for LCTS No. 2, and 1.3 μm for LCTS No. 3. Ideality factors (n, at room temperature) were measured to be 2.03 for LCTS No. 1, 2.00 for LCTS No. 2, and 1.98 for LCTS No. 3 for the linear regions shown in Fig. 14.

LCTS No. 2 and No. 3 were also characterized by 77-K photoluminescence to compare the optical properties of AlGaAs and In-doped AlGaAs. Full widths at half maximum (FWHMs) of 117 and 71 meV were obtained for AlGaAs and In-doped AlGaAs, respectively. This reduction in FWHM indicates that the optical quality of n-doped AlGaAs can be improved by the addition of In(~1 at. %) to the AlGaAs layer (see also Ref. 34).

In addition, the incorporation of In (~1 at. %) in MBE-grown, Si-doped AlGaAs seems to slow the Zn diffusion. The same slow Zn diffusion was also experienced for MBE-grown a TJS laser structure with In-doped (~1 at. %) AlGaAs confining layers (data not shown here). Slow Zn diffusion in In-doped AlGaAs might be explained in terms of increased Si incorporation by the addition of In to Si-doped AlGaAs during the materials growth. Increased Si incorporation by the addition of In to Si-doped GaAs has been previously reported.[35]

For a p^+-n junction, the total forward current can be approximated by summing the diffusion current and recombination current and expressed as follows:[36]
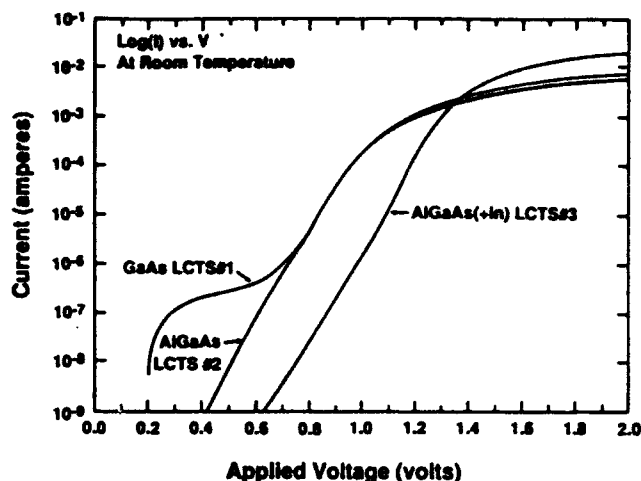

FIG. 14. Current-voltage characteristics measured at room temperature for three leakage current test structures. Improvement in the turn-on voltage by the addition of In in the AlGaAs layer (LCTS No. 3) is shown. However, for GaAs LCTS No. 1 and AlGaAs LCTS No. 2 the turn-on voltages are the same.

$$J_F = q\sqrt{\frac{D_p}{\tau_p}} \frac{n_i^2}{N_D} \exp\left(\frac{qV}{kT}\right) + \frac{qW}{2} \sigma v_{th} N_t n_i \exp\left(\frac{qV}{2kT}\right),$$
(5)

where q is electric charge, D_p is the diffusion coefficient for holes (minority carriers), t_p is the minority-carrier lifetime, n_i is the intrinsic carrier concentration, N_D is the donor impurity concentration, k is Boltzmann's constant, T is the absolute temperature, W is the depletion region width, σ is the capture cross section, v_{th} is the thermal velocity, and N_t is the trap density. The equilibrium hole concentration in the n-type semiconductor is p_{no} and the equilibrium electron concentration in the p-type semiconductor is n_{po}. Equation
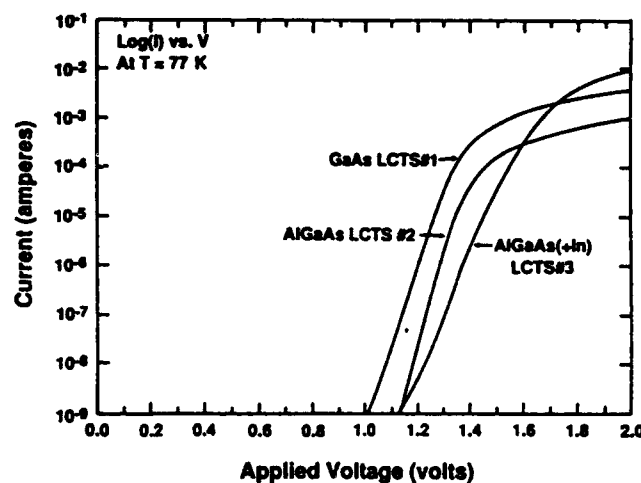

FIG. 15. Current-voltage characteristics measured at 77 K for the same leakage current test structures as shown in Fig. 14. An improvement in turn-on voltage observed by the incorporation of In in AlGaAs in Fig. 14 is seen for AlGaAs without In doping (LCTS No. 2) with a reference to GaAs (LCTS No. 1).

1088   J. Appl. Phys., Vol. 69, No. 2, 15 January 1991

Sin et al.   1088

(5) assumes that p_{so} is much greater than n_{so} and that V is greater than KT/q. The first term of Eq. (5) is the ideal diffusion term while the second term is the recombination term. The ideality factors for all of the samples are approximately 2 as would be expected for wide band-gap semiconductors like GaAs or AlGaAs, so the recombination current dominates the diffusion current. Since the recombination current dominates, the first term of Eq. (5) can be neglected and the total forward current can be approximated as follows:

$$J_F \cong (qW/2)\sigma v_{th} N_t n_i \exp(qV/2kT). \qquad (6)$$

Thus, any differences in junction characteristics can be evaluated by studying the prefactors in J_F. W and n_i can be calculated given that the acceptor (Zn) concentration for sample No. 1, No. 2, and No. 3 is assumed to be around $10^{19}/cm^3$ and that the forward biases needed to have a forward current (I_F) of $10 \mu A$ are 0.845, 0.845, and 1.092 V for LCTS No. 1, No. 2, and No. 3, respectively (from Fig. 14). An improvement of 0.247 V in turn-on voltage ($\Delta V_T = 1.092 - 0.845 = 0.247$ V, where V_T is the turn-on voltage) was obtained from Fig. 14. Forward current (I_F) is the product of forward current density (J_F) and junction cross section (A_j), and A_j is the product of cavity length (L, $250 \mu m$) and junction depth. The built-in potentials (V_0, from Table III) are calculated to be 1.468 V for LCTS No. 1 and 1.804 V for LCTS No. 2 and No. 3, so the use of depletion approximation is justified for the forward-bias levels considered above. Table III summarizes measured and estimated or calculated parameters used to compare trap densities in LCTS No. 2 and No. 3.

The following assumptions are made in comparing N_t of LCTS No. 2 and No. 3:

(1) Bulk recombination current dominates surface recombination current.

(2) The product of σ and v_{th} is the same for all of the samples.

(3) Strain effect introduced by doping $Al_{0.35}Ga_{0.65}As$ with In (1%) for LCTS No. 3 can be neglected.

(4) p-n junctions are one-sided step junctions since junction depths are normally shorter than $3 \mu m$ (shallow junctions in our case).

(5) The Shockley–Read–Hall (SRH) model (single energy level for a trap) can be used as an approximation in low-level injection.

After some straightforward algebra, the following is obtained:

$$\frac{N_t(LCTS\ No.\ 2)}{N_t(LCTS\ No.\ 3)} \cong 50. \qquad (7)$$

The above result means that isoelectronic In doping can reduce the trap density in $Al_{0.35}Ga_{0.65}As$ (Si: $10^{17}/cm^3$) by more than one order of magnitude.

The dramatic reduction of trap density in the AlGaAs layer (confining layer of TJS laser) by isoelectronic In doping might imply that the threshold current of a TJS laser can be reduced in a rather dramatic fashion, too. As shown in Figs. 14 and 15, about 20 times less current flows in LCTS No. 2 (AlGaAs) than in LCTS No. 1 (GaAs) at 77 K (from 10^{-5} to 6×10^{-7} A at 1.27 V), while there is almost no difference in current flows in both samples at room temperature. This can explain why such low threshold TJS lasers are obtained at 77 K even if they do not lase at room temperature (data not shown here).[32] As temperature increases, the leakage current dominates current flow in the wide band-gap junction. Shunting currents as much as 20 times the active region current can be present during room-temperature operation resulting in an elevated threshold current by a similar factor. In Fig. 14, at room temperature, LCTS No. 3 shows ideal characteristics (much higher turn-on voltage in comparison to the other structures) observed with LCTS No. 2 only at 77 K. As a result, shunting currents can be reduced in a dramatic fashion by isoelectronic doping in AlGaAs confining layers (reducing trap density and increasing the turn-on voltage of the AlGaAs p-n homojunction).

Based on the recently demonstrated GaAs-AlGaAs lattice-matched and InGaAs-GaAs-AlGaAs strained-layer MQW TJS lasers and the above arguments on shunting currents of TJS lasers, we anticipate that a further reduction in the threshold current of TJS lasers is possible, making these lasers more desirable for integrated optoelectronic circuits (IOECs).

TABLE III. Measured and estimated or calculated parameters used to compare trap densities in leakage current test structures (GaAs, AlGaAs, and AlGaAs + In).

Parameters	GaAs LCTS No. 1	AlGaAs LCTS No. 2	AlGaAs(+ In) LCTS No. 3
$x_j (\mu m)$	1.3	2.6	1.3
$L(\mu m)$	250	250	250
n	2.03	2.00	1.98
$N_D(Si, cm^{-3})$	2×10^{18}	10^{17}	10^{17}
$N_A(Zn, cm^{-3})$[a]	10^{19}	10^{19}	10^{19}
$n_i(cm^{-3})$[a]	2.46×10^6	863	863
$V_0(V)$[a]	1.468	1.804	1.804
$V(V)$ at $I_F = 10 \mu A$	0.845	0.845	1.092
$W(cm)$[a] at $I_F = 10 \mu A$	2.33×10^{-6}	1.13×10^{-5}	9.76×10^{-6}

[a] Estimated or calculated values.

IV. SUMMARY

Surface treatments of $(NH_4)_2S$ have been demonstrated that reduce surface leakage currents in current injection lasers. After the treatments, around 20 times less current from current-voltage characteristics has been measured with GaAs/AlGaAs multiple-quantum-well TJS lasers at an applied voltage of 0.7 V. The laser thresholds of lattice-matched TJS lasers have been reduced by 12 mA (or 16%) after the chemical treatments. Also, InGaAs-GaAs-AlGaAs strained-layer single-quantum-well stripe-geometry lasers using spin-on-glass film for stripe definition have been treated chemically and a reduction in the laser threshold of 10 mA (or 14%) has been observed. The surface treatments have been effective for 6–7 days, but more detailed lifetime studies are still necessary.

The strong temperature dependence of TJS laser thresholds can be explained by bulk leakage currents in TJS lasers, so the quality of the AlGaAs confining layers is very important to TJS lasers. We have also demonstrated that the idea of isoelectronic In doping of AlGaAs can be applied to reducing the bulk leakage currents in Zn-diffused lateral p-n junctions. The use of this technique is suggested to improve the laser thresholds and temperature dependence of TJS lasers.

ACKNOWLEDGMENTS

[1] H. Kumabe, T. Tanaka, H. Namizaki, S. Takamiya, M. Ishii, and W. Susaki, Jpn. J. Appl. Phys. 18, Suppl. 18-1, 371 (1979).

[2] H. Kumabe, T. Tanaka, H. Namizaki, M. Ishii, and W. Susaki, Appl. Phys. Lett. 33, 38 (1978).

[3] I. Ury, S. Margalit, M. Yust, and A. Yariv, Appl. Phys. Lett. 34, 430 (1979).

[4] R. Kolbas, J. Carney, J. Abrokwah, E. Kalweit, and M. Hitchell, Proc. SPIE 321, 94 (1982).

[5] Y. J. Yang, Y. C. Lo, G. S. Lee, K. Y. Hsieh, and R. M. Kolbas, Appl. Phys. Lett. 49, 835 (1986).

[6] Y. J. Yang, K. Y. Hsieh, and R. M. Kolbas, Appl. Phys. Lett. 51, 215 (1987).

[7] S. D. Offsey, J. M. Woodall, A. C. Warren, P. D. Kirchner, T. I. Chappell, and G. D. Pettit, Appl. Phys. Lett. 48, 475 (1986).

[8] J. Massies, J. Chaplart, M. Laviron, and N. T. Linh, Appl. Phys. Lett. 38, 693 (1981).

[9] R. J. Nelson, J. S. Williams, H. J. Leamy, B. Miller, H. C. Casey, Jr., B. A. Parkinson, and A. Heller, Appl. Phys. Lett. 36, 76 (1980).

[10] C. J. Sandroff, R. N. Nottenburg, J. C. Bischoff, and R. Bhat, Appl. Phys. Lett. 51, 33 (1987).

[11] M. S. Carpenter, M. R. Melloch, M. S. Lundstrom, and S. P. Tobin, Appl. Phys. Lett. 52, 2157 (1988).

[12] J. Fan, H. Oigawa, and Y. Nannichi, Jpn. J. Appl. Phys. 27, L1331 (1988).

[13] J. Fan, H. Oigawa, and Y., Nannichi, Jpn. J. Appl. Phys. 27, L2125 (1988).

[14] B. J. Skromme, C. J. Sandroff, E. Yablonovitch, and T. Gmitter, Appl. Phys. Lett. 51, 2022 (1987).

[15] R. S. Besser, and C. R. Helms, Appl. Phys. Lett. 52, 1707 (1988).

[16] D. Liu, T. Zhang, R. A. LaRue, J. S. Harris, Jr., and T. W. Sigmon, Appl. Phys. Lett. 53, 1059 (1988).

[17] L. A. Farrow, C. J. Sandroff, and M. C. Tamargo, Appl. Phys. Lett. 51, 1931 (1987).

[18] E. Yablonovitch, C. J. Sandroff, R. Bhat, and T. Gmitter, Appl. Phys. Lett. 51, 439 (1987).

[19] C. H. Henry and R. A. Logan, J. Vac. Sci. Technol. 15, 1471 (1978).

[20] H. Kawanishi, H. Ohno, T. Morimoto, S. Kaneiwa, N. Miyauchi, H. Hayashi, Y. Akagi, Y. Nakajima, and T. Hijikata, Proc. SPIE (OE/LASE), 1219 (1990).

[21] M. I. Nathan, Solid-State Electron. 29, 167 (1986).

[22] V. Swaminathan and W. T. Tsang, Appl. Phys. Lett. 38, 5 (1981).

[23] W. T. Tsang and V. Swaminathan, Appl. Phys. Lett. 39, 6 (1981).

[24] W. C. Mitchel and P. W. Yu, J. Appl. Phys. 57, 623 (1985).

[25] H. Beneking, P. Narozny, and N. Emeis, Appl. Phys. Lett. 47, 828 (1985).

[26] P. K. Bhattacharya, S. Dhar, P. Berger, and F. Y. Juang, Appl. Phys. Lett. 49, 470 (1986).

[27] A. Z. Li, H. K. Kim, J. C. Jeong, D. Wong, T. E. Schlesinger, and A. G. Milnes, J. Appl. Phys. 67, 3497 (1988).

[28] T. M. Kerr, T. D. Mclean, D. I. Westwood, J. D. Medland, S. R. Blight, and C. E. C. Wood, J. Vac. Sci. Technol. B 4, 521 (1986).

[29] J. F. Chen and C. R. Wie, J. Electron. Mater. 17, 501 (1988).

[30] H. C. Casey, Jr. and M. B. Panish, *Heterostructure Lasers*, Part B (Academic New York, 1978), pp. 229–230.

[31] H. Namizaki, IEEE J. Quantum Electron. QE-11, 427 (1975).

[32] R. M. Kolbas (unpublished).

[33] Y. K. Sin and R. M. Kolbas (unpublished).

[34] A. Uddin and T. G. Andersson, J. Appl. Phys. 65, 3101 (1989).

[35] M. K. Lee, T. H. Chiu, A. Dayem, and E. Agyekum, Appl. Phys. Lett. 53, 2653 (1988).

[36] S. M. Sze, *Physics of Semiconductor Devices*, 2nd ed. (Wiley, New York, 1981), p. 92.

InGaAs-GaAs-AlGaAs strained-layer laser with heavy silicon doping

Y. K. Sin, K. Y. Hsieh, J. H. Lee, Y. Hwang, and R. M. Kolbas
*Department of Electrical and Computer Engineering, North Carolina State University,
Raleigh, North Carolina 27695-7911*

Photoluminescence characteristics of uniformly silicon- and beryllium-doped pseudomorphic
InGaAs-GaAs-AlGaAs single- and multiple-quantum-well heterostructures grown by
molecular-beam epitaxy are studied. Red shifts in the photoluminescence peaks are obtained
from uniformly silicon-doped single-quantum-well samples with respect to undoped
samples. Uniformly beryllium-doped InGaAs-GaAs multiple quantum wells totally intermix
during materials growth. Also, the effect on laser performance (laser thresholds and
emission spectra) by silicon doping is demonstrated with an InGaAs-GaAs-AlGaAs
strained-layer laser (grown by molecular-beam epitaxy) with a heavily silicon-doped quantum
well. The low laser threshold, kink in light versus current, shift in emission wavelength,
and two emission peaks are observed, and these characteristics are believed to be due to heavy
silicon doping.

I. INTRODUCTION

Strained-layer InGaAs-GaAs-AlGaAs current injection lasers have been extensively investigated in recent years. For example, a low threshold current InGaAs strained-layer ridge waveguide laser[1] operating at 1 μm and a high-power phase-locked InGaAs strained-layer laser array[2] with an emission wavelength of 1.03 μm have been reported. Our group has recently reported the materials growth, materials characterization, device fabrication, device results, and modeling of strained-layer InGaAs-GaAs-AlGaAs photopumped and current injection quantum-well (QW) lasers.[3] These experimental reports demonstrate that as with the GaAs-AlGaAs lattice-matched system, desirable characteristics (low threshold current, high-power operation, etc.) are possible with InGaAs strained-layer quantum-well lasers.

Previous research efforts have focused on undoped InGaAs quantum-well heterostructures. Recently, both experimental and theoretical evidence have indicated that doping the quantum wells in a semiconductor laser can improve laser performance. These improvements include reducing the laser threshold and noise enhancement factor with n-type doping (InGaAs/InP),[4] and increasing the relaxation oscillation corner frequency and 3-dB cutoff frequency with p-type doping (InGaAs/AlGaAs on GaAs and InGaAs/InAlAs on InP, or GaAs/AlGaAs).[5,6] Also, the enhanced carrier collecting capability of a degenerately Sn-doped GaAs quantum well due to positive donors that attract the photoexcited electrons was reported.[7] In addition, threading dislocations have been reported to have less effect on GaAs/AlGaAs multiple-quantum-well (MQW) structures with doped QWs than on those with undoped QWs.[8]

In this paper we present the photoluminescence characteristics of n- and p-type pseudomorphic InGaAs-GaAs-AlGaAs single- and multiple-quantum-well heterostructures and injection laser results from an InGaAs-GaAs-AlGaAs single quantum well (SQW) with heavy Si doping.

II. EXPERIMENT

A. Photoluminescence samples

All of the photopumped laser samples used in this study were grown by molecular-beam epitaxy (MBE, Varian 360). Pseudomorphic single-quantum-well (SQW) or multiple-quantum-well (MQW) laser samples for photopumping were grown as follows. A 0.5-μm-thick undoped $Al_{0.3}Ga_{0.7}As$ lower confining layer was deposited on a 100-oriented GaAs ($n \approx 3 \times 10^{18}$, Si) substrate. For the SQW samples, an active region consisting of a single $In_xGa_{1-x}As$ quantum well (undoped, Si doped, or Be doped) sandwiched between 450-Å-thick undoped GaAs barriers was deposited. For the MQW samples, the active region consists of four $In_xGa_{1-x}As$ QWs (undoped, Si doped, or Be doped) separated by 600-Å-thick undoped GaAs barriers. The growth conditions used for the SQW or MQW samples such as In flux and Si or Be cell temperatures are given in Table I. Finally, a 0.5-μm-thick undoped top confining layer of $Al_{0.3}Ga_{0.7}As$ was deposited. The lower AlGaAs confining layer was grown at 686 °C followed by a stop growth (around 4 min under As overpressure) during which the temperature was lowered to 550 °C to deposit the active region. The top confining layer was grown while ramping the temperature up to 686 °C.

In preparation for 77-K photoluminescence (PL) measurements, small sections of the samples were pressed into a layer of indium on a copper plug[9] and cooled to 77 K in a liquid-nitrogen dewar. An argon laser beam ($\lambda = 5145$ Å) was focused on the sample surface, and the luminescence was measured using a 0.5-m spectrometer and a cooled S-1 photomultiplier.

B. Laser diodes

The growth conditions for the laser structure were as follows. First, a 1-μm-thick GaAs buffer layer ($n \approx 2 \times 10^{18}$/cm^3, Si) was deposited on a 100-oriented GaAs ($n \approx 3 \times 10^{18}$, Si) substrate at 627 °C followed by a 1.5-μm-thick $Al_{0.35}Ga_{0.65}As$ confining layer ($n \approx 10^{17}$, Si).

0021-8979/91/020568-06$03.00

TABLE I. Photoluminescence results and growth conditions used for InGaAs-GaAs-AlGaAs SQW or MQW heterostructures. Un, Si, and Be denote undoped, Si-doped, and Be-doped samples, respectively. $\Delta\lambda = \lambda_{PL}$ (Si or Be) $- \lambda_{PL}$ (un).

Structure number	Sample	L_z (Å)	In flux $(\times 10^{-7})$ (Torr)	T_{Si} or T_{Be} (°C)	λ_{PL} (Å) (77 K)	$\Delta\lambda$ (Å)	FWHM (meV)	Comments
	18 A	65 (un)	2.5	...	9270	...	33	$In_{0.22}Ga_{0.78}As$
18	18 B	65 (Si)	2.5	1174	9600	+330	46	
(SQW)	18 C	65 (Si)	2.6	1096	9500	+230	40	
	18 D	65 (Be)	2.5	980	9630	+360	48	
	19 A	65 (un)	2.1	...	8680	...	14	$In_{0.12}Ga_{0.88}As$
19	19 B	65 (Si)	2.1	1175	9110	+430	74	
(SQW)	19 C	65 (Si)	2.1	1064	9040	+360	24	
	19 D	65 (Be)	2.1	980	9140	+460	15	
20	20 A	40 (un)	2.4	...	8740	...	7	$In_{0.19}Ga_{0.81}As$
(SQW)	20 B	40 (Si)	2.4	1175	8820	+80	45	
	27 A	65 (un)	2.4	...	8950	...	10	$In_{0.16}Ga_{0.84}As$
27	27 B	65 (Si)	2.3	1189	9000	+50	88	
(MQW)	27 C	65 (Si)	2.3	1098	9140	+190	19	4QWS
	27 D	65 (Be)	2.4	1004	8330	−620	50	

The active region consisting of 450 Å of undoped GaAs, 45 Å of InGaAs (estimated to be greater than $5 \times 10^{18}/cm^3$, Si), and 450 Å of undoped GaAs was then deposited. The growth rate for the InGaAs QW was 3.6 Å/s and the Si cell temperature (T_{Si}) used to dope the QW was 1174 °C. From characterization of $In_xGa_{1-x}As$ bulk samples (Table II), the net carrier concentration can be estimated to be greater than $5 \times 10^{18}/cm^3$ since almost the same T_{Si} with the same In flux was used to dope the InGaAs QW for the current injection laser sample. Finally, a 1.5-μm-thick top confining layer of $Al_{0.35}Ga_{0.65}As$ ($p \approx 2 \times 10^{18}$, Be) and a 0.5-$\mu$m-thick GaAs cap layer ($p \approx 3 \times 10^{18}$, Be) were deposited. The lower AlGaAs confining layer was grown at 686 °C followed by a stop growth (around 4 min under As overpressure) during which the temperature was lowered to 550 °C to deposit the active region. The top confining layer was grown while ramping the temperature back up to 686 °C.

The following processing steps were performed to obtain spin-on glass (SOG) stripe geometry laser diodes. Only two steps (spinning and curing) were necessary to prepare the SOG films. The film uniformity (after being cured; 400 °C, 30 min) was better than 1.6% across a 2-in. silicon wafer. The thickness and refractive index of the cured film (spin speed of 5 krpm and spin time of 40 s)

were 1386 Å and 1.374, respectively. Pinhole density ($< 1/cm^2$) in the film was small, and adhesion of Cr/Au (for p Ohmic contact) to the film was good. The dielectric breakdown behavior of a 1386-Å-thick SOG film was studied, and no current was detected ($< 1 \mu$A) with an applied voltage of more than 150 V. Standard photolithography was employed to define stripe patterns and the film was etched to form stripes by reactive ion etching (RIE) with a mixture of CF_4 and O_2. The substrate was thinned down to about 100 μm and the Ohmic contacts were deposited. AuGe-Au (350 Å-1500 Å) and Cr-Au (200 Å-1500 Å) were thermally evaporated for n and p Ohmic contact, respectively. The n Ohmic contact was annealed at 425 °C for 2.5 min. Finally, laser dice were prepared by cleaving (250 μm) and sawing (200 μm).

III. RESULTS AND DISCUSSION

A. Photoluminescence

The 77-K photoluminescence (PL) results and growth conditions used (In flux and Si or Be cell temperatures T_{Si} or T_{Be}) for the photopumped laser samples are summarized in Table I. Throughout this experiment, the samples with the same structure number were grown sequen-

TABLE II. Hall-measurement results and growth conditions used for InGaAs bulk layers grown by MBE on GaAs substrates. $N_{A,D} - N_{D,A}$ denotes the net carrier concentration.

Sample	In flux $(\times 10^{-7}$ Torr$)$	Ga flux $(\times 10^{-7}$ Torr$)$	T_{Si} or T_{Be} (°C)	Thickness (μm)	Hall mobility (cm^2/V s)	$N_{A,D} - N_{D,A}$ $(\times 10^{18}$ cm$^{-3})$
8-0927A	2.2	5.6	1167 (Si)	1	1507	5.6 (n)
9-0519C	2.0	5.7	1170 (Si)	3.4	2435	2.7 (n)
9-0519D	0.5	5.7	977 (Be)	1	135	2.0 (p)
9-1103D	2.0	5.6	1176 (Si)	1	1593	2.9 (n)
9-1103F	2.0	5.6	990 (Be)	1	94	4.4 (p)
9-1106A	2.4	5.6	1176 (Si)	1	1766	3.9 (n)

tially on the same day under identical conditions to insure the highest degree of repeatability possible. Structures 18, 19, and 20 are SQW samples, whereas structure 27 is a MQW sample.

The InGaAs bulk samples were employed to calibrate the net carrier concentration versus T_{Si} or T_{Be} for the InGaAs QWs. The room-temperature Hall-measurement results and growth conditions used (In flux and T_{Si} or T_{Be}) for the six InGaAs bulk layers (1 or 3.4 μm thick) grown on semi-insulating GaAs substrates are summarized in Table II. The growth temperature for the samples was fixed at 550 °C and the growth rate was 3.6 Å/s. Experimental data on the net carrier concentration versus T_{Si} or T_{Be} have been reported for n- or p-doped In$_{0.53}$Ga$_{0.47}$As on InP substrate,[10] but not for an n- or p-doped InGaAs lattice mismatched to GaAs substrate. Thus, the data presented here should be useful for the design of InGaAs strained-layer lasers with doped QWs assuming that allowances are made in regard to the incorporation rate versus strain and carrier trapping due to defects from the lattice mismatch.

The InGaAs bulk layers on GaAs substrates, undoped and heavily Be-doped (Be: approximately 4.4×10^{18}, 9-1103F), were characterized by both PL and x-ray diffraction. The fact that the In compositions of undoped and Be-doped bulk samples with the same In flux (2.0 $\times 10^{-7}$ Torr) measured from x-ray diffraction were both 18%, demonstrates that the doping effect on the PL peak shifts observed in this study is due to doping the QWs and not due to material growth problems such as In concentration variations during the InGaAs QW growth. The 77-K PL peak at 9650 Å was obtained for the undoped InGaAs bulk sample. An In composition of 15% is obtained for the undoped reference sample from E_g (In$_x$Ga$_{1-x}$As, bulk, 77 K) = 1.5076 − 1.63X + 0.53X^2 (see Ref. 3). Residual n-type impurities in unintentionally doped InGaAs layers grown by MBE can be responsible for the difference between these two measurements. Unintentionally doped MBE-grown InGaAs was reported to be n-type (about 10^{16}/cm^3) mainly due to impurities from the In source.[11,12]

Red shifts in the PL peaks (not blue shifts due to Moss–Burstein shifts) were observed from the Si-doped SQW samples of structures 18, 19, and 20. For each structure, an undoped sample was used as a reference. Red shifts with both Si and Be doping were seen from the SQW samples of structures 18 and 19. The impurities (Si or Be) were uniformly doped (not spike doped) in the InGaAs quantum wells. Red shifts with the Si doping in the InGaAs QWs are in marked contrast to other experimental reports with Sn-doped (n type) In$_{0.53}$Ga$_{0.47}$As bulk layers (blue shifts observed) on InP substrates grown by liquid-phase epitaxy (LPE),[13] and with a spike Si-doped In$_{0.16}$Ga$_{0.84}$As MQW grown by MBE.[14] Si and Be dopants were reported to be donors and acceptors in an In$_{0.53}$Ga$_{0.47}$As on InP substrate, respectively.[11,12] Also, as seen in Table II, Si and Be dopants behaved as donors and acceptors in In$_x$Ga$_{1-x}$As ($x < 0.53$) bulk layers on GaAs substrate, respectively.

The following can be observed from Table I. The amount of red shifts increases as the Si doping density increases from 5×10^{17} to 4×10^{18} for a fixed In composition ($x = 0.12$ or 0.22) and QW thickness. This can be due to a narrower band gap (thus longer λ_{PL}) in a more heavily Si-doped sample. The difference of 10 meV in red shifts from samples 19-B (Si: around 4×10^{18}) and 19-C (Si: around 5×10^{17}) has been measured by PL. This measured value is close to the difference of 13 meV in band-gap shrinkages calculated from $\Delta E_g = -1.6 \times 10^{-8}p^{1/3}$ for a p-doped GaAs bulk layer with ΔE_g in eV and p in cm^{-3}.[15]

Acceptorlike behavior of the Si impurities (red shifts) in the InGaAs QWs can be explained by the amphoteric nature of Si. One group observed the amphoteric character of Si in an In-doped GaAs bulk layer.[16] They found that Si impurities were acceptors in an In-doped (around 1.5 at. %) GaAs that had been annealed with a silicon nitride cap, and attributed the formation of Si$_{As}$ (acceptors, the Si atoms at the As sites) to a reduced density of V_{Ga} (the Ga vacancies) caused by the In$_{Ga}$ atoms (the In atoms at the Ga sites) whose large ionic radii alter the point defect energies on the entire Ga sublattice.[16] The fact that the amphoteric character of Si was observed from InGaAs QW samples (Table I), but not from InGaAs bulk samples (Table II) can be explained by the different growth processes for the QW and bulk samples. The growth of the 0.5-μm-thick upper Al$_{0.3}$Ga$_{0.7}$As confining layer and 450-Å-thick upper GaAs barrier on the Si-doped InGaAs QW (in situ annealing during the growth with the QW buried) could have the same effect as the silicon nitride capping and annealing on the amphoteric character of Si impurities. The Si impurities (the most widely used n-type dopants in MBE crystal-growth technology) uniformly doped in the InGaAs QWs being acceptors suggests that other dopants be investigated to be employed as donors for the InGaAs QWs.

A blue shift was observed from a heavily Be-doped (Be > 5×10^{18}/cm^3) MQW sample (sample 27-D). For the Si-doped SQW samples of structures 18 (18-B and 18-C) and 19 (19-B and 19-C), the amount of red shifts increased as the Si doping density increased. However, for the Si-doped MQW samples (27-B and 27-C), the amount of red shifts was reduced as the Si doping density was increased. To explain the different PL peak shifts from the MQW samples with respect to the SQW samples, the Si and Be cell temperatures used to dope the InGaAs QWs (Si and Be doping densities) need to be considered (see Table I). T_{Be} for 18-D and 19-D (SQW samples) was 980 °C, while 1004 °C was used for 27-D (MQW sample). T_{Si} for the heavily Si-doped SQW samples of 18-B, 19-B, and 20-B was 1174–1175 °C, while 1189 °C was used for the MQW sample (27-B). Thus, the MQW samples (27-B and 27-D) were more heavily Si or Be doped than the SQW samples. The λ_{PL} of 8330 Å observed from the heavily Be-doped MQW sample corresponds to a p-doped GaAs at 77 K. In other words, the InGaAs QWs were almost completely disordered as the Be cell temperature increased by only 24 °C from 980 °C (Be: around 2

Strained Layer Laser
InGaAs-GaAs-AlGaAs
SQW SCH (Heavily Si - Doped)
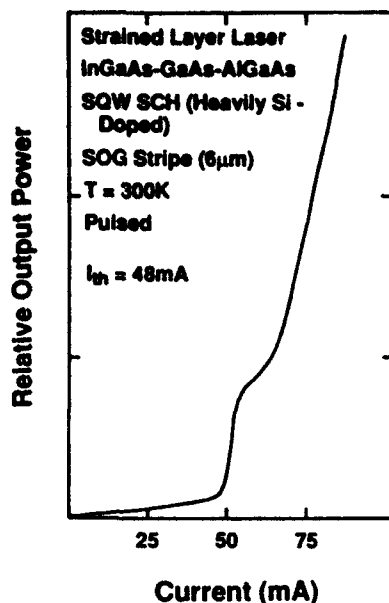**SOG Stripe (6μm)**
T = 300K
Pulsed
I_{th} = 48mA

FIG. 1. Light vs current characteristic for a strained-layer InGaAs-GaAs-AlGaAs single-quantum-well laser diode with a 45-Å-thick heavily Si-doped quantum well.

$\times 10^{18}/cm^3$) to 1004 °C (Be: around $8 \times 10^{18}/cm^3$). This is consistent with other experimental reports for GaAs,[17,18] but no reports for InGaAs. For heavily Be-doped GaAs/AlGaAs superlattices, the threshold for fast Be diffusion (or for the total layer intermixing) was between $2 \times 10^{19}/cm^3$ and $5 \times 10^{19}/cm^3$.[18] The surface accumulation of Be during the growth (rather than the Be diffusion) could be responsible for the disordering of the heavily Be-doped InGaAs MQW grown at 550 °C (sample 27-D) like GaAs/AlGaAs superlattices grown at 540 °C.[19] In addition, the red shift observed from the heavily Si-doped MQW sample can be explained by a low In-Ga interdiffusion coefficient of Si. A smaller red shift from the more heavily Si-doped sample (sample 27-B) compared to sample 27-C demonstrates that the Si dopants at T_{Si} = 1189 °C enhance the In-Ga layer disordering during the materials growth.

B. Laser diodes

The optical quality of the injection laser sample was first studied by fabricating broad-area lasers (200×250 μm^2). A threshold current density of 0.73 kA/cm² from the heavily Si-doped SQW sample compares favorably to other undoped QW samples (threshold current density of 1.1–1.3 kA/cm² obtained, data not shown here). The low laser threshold current density from the heavily Si-doped SQW laser sample is believed to be due to doping effects on the optical gain as predicted theoretically.[4]

Next, stripe geometry lasers using a spin-on glass (SOG) film for stripe definition were processed. Comparable laser diode results have been obtained from lasers with a SOG film and traditional oxide (data not shown here).[20] The stripe width was 6 μm and the size of a completed laser diode was 200×250 μm^2. The laser diode had

a series resistance of approximately 5 Ω, and a reverse breakdown voltage of around 6 V.

The light versus current (L-I) characteristic (threshold at 48 mA) is shown in Fig. 1. This laser threshold is remarkably low considering that it is a gain guided laser with a simple separate confinement heterostructure (SCH) SQW active region, not a graded index (GRIN) SCH structure. In addition, this threshold value compares favorably with a proton-bombarded stripe laser (strained undoped InGaAs SQW GRIN SCH laser).[21] A kink in the light versus current was observed. Note that a similar kink in the light versus current was also observed by another group using a highly p-doped (Be = $10^{19}/cm^3$) GaAs/AlGaAs MQW laser.[6] Several factors have been identified for kinks in the light versus current for the double-heterostructure (DH) lasers including defects in the junction region, which can produce lasing in filaments, and lateral mode changes in lasers with weak lateral mode guiding.[22-24] Since defects manifest themselves as spikes in the L-I curve,[23] they are probably not responsible for the smooth kink observed in Fig. 1. Kinks in the L-I curves of DH lasers can be eliminated by employing a narrow stripe width (about 8 μm) to prevent lasing mode shifts,[25] and by introducing a refractive index guiding to stabilize horizontal transverse modes.[26] The reasons we believe that the kink observed in Fig. 1 is due to doping the InGaAs QW, and not due to processing are as follows: (i) A kink in the L-I curve was observed from both broad-area lasers (data not shown here) and stripe geometry lasers (Fig. 1); (ii) the kinks in the L-I curves were not observed from our series of undoped strained-layer InGaAs-GaAs oxide and spin-on glass stripe lasers with the stripe width of around 6 μm (data not shown here); and (iii) the kinks were not observed for a conventional DH laser with a heavily compensated GaAs active region (1000 Å, Si: around 2×10^{18}, Be: around 3×10^{18}, data not shown here).

An indium composition of 14% was estimated from growth conditions (In flux of 2.2×10^{-7} Torr, see Table I). The transition energy of 1.346 eV (= 9230 Å) (taking into account quantum-size effect as well as strain effect) is expected for a 45-Å-thick undoped $In_{0.14}Ga_{0.86}As$ QW with GaAs barriers from our model.[3] However, the transition energy of 1.395 eV corresponding to the emission wavelength of 8907 Å from Fig. 2(a) was obtained from the 45-Å-thick heavily Si-doped $In_{0.14}Ga_{0.86}As$ quantum well. In addition, from a 40-Å-thick heavily Si-doped (about $5 \times 10^{18}/cm^3$) $In_{0.19}Ga_{0.81}As$ SQW, the amount of red shift was measured to be 80 Å (structure 20, see Table I). Thus, an emission wavelength of about 9330 Å (= 9230 Å + 100 Å, where 100 Å is from the red shift) was roughly expected for the 45-Å-thick heavily Si-doped $In_{0.14}Ga_{0.86}As$ QW without taking the layer intermixing effect into account. But the InGaAs-GaAs layer intermixing enhanced by the Si impurities in an InGaAs quantum well as observed from the sample 27-B needs to be considered. The redistribution of the Si dopants into the upper GaAs barrier due to uniform doping (doping the edges) could be responsible in part for the enhancement of the InGaAs-GaAs layer intermixing by Si.[27] In this case, a
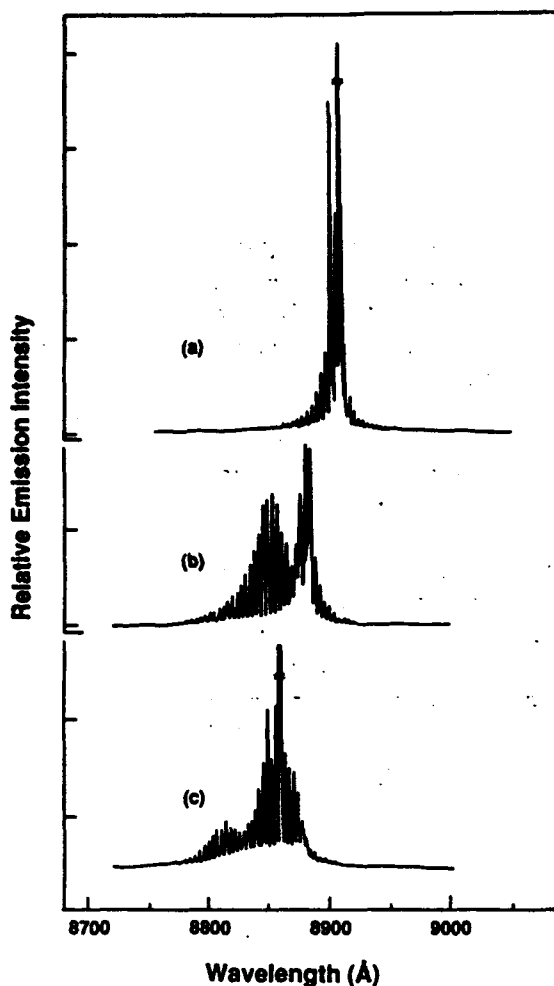
FIG. 2. Emission spectra for a strained-layer laser diode with a 45-Å-thick heavily Si-doped quantum well for three different injection current levels: (a) $I = 1.4I_{th}$; (b) $I = 2.0I_{th}$; and (c) $I = 2.7I_{th}$.

blue shift of around 400 Å (= 9330 Å − 8907 Å) was attributed to the impurity-enhanced layer disordering during the crystal growth. Another group observed the same amount of shift in the lasing wavelength (400 Å) from an undoped InGaAs GRIN SCH SQW laser after an LPE cycle.[28]

The emission spectra are shown in Fig. 2 for three different injection current levels ($I = 1.4I_{th}$, $2.0I_{th}$, and $2.7I_{th}$). First, multiple longitudinal modes were shown as in Fig. 2(a) (lasing peak at 8907 Å, $I = 1.4I_{th}$). But as the current increased ($I = 2.0I_{th}$), the modes at lower wavelengths ($\lambda = 8852$ Å) became comparable to the original modes [$\lambda \approx 8880$ Å, Fig. 2(b)]. At $I = 2.7I_{th}$, the higher-energy modes dominated the lower-energy modes and almost a single longitudinal mode was observed at 8858 Å [Fig. 2(c)]. Photopumped lasers (see Ref. 29) were also made from the sample with a 45-Å-InGaAs (Si: around 5×10^{18}) QW sandwiched between 100-Å-thick undoped GaAs carrier collection layers separated by 0.5-μm-thick undoped $Al_{0.35}Ga_{0.65}As$ confining layers. Two emission peaks were also observed from the quantum well of the photopumped lasers at 77 K, one at 8550 Å (1.453 eV) and the other at 8600 Å (1.445 eV), (data not shown

here). The separation between the two peaks was 50 Å (8 meV) which was very close to that for the injection laser sample (peaks at 8907 and 8858 Å, 1.403 eV − 1.395 eV = 8 meV, see Fig. 2). The fact that two emission peaks were obtained from both photopumped and current injection lasers suggests that they are related to the doping.

IV. SUMMARY

Moss–Burstein shifts (blue shifts with respect to undoped samples) in the photoluminescence peaks were not observed from uniformly Si-doped pseudomorphic InGaAs-GaAs-AlGaAs single-quantum-well samples as expected. Instead, red shifts were observed from the Si-doped samples, and silicon dopants being acceptors was explained in terms of the amphoteric character of Si. The Si impurities (the most widely used n-type dopants in MBE crystal-growth technology) being acceptors suggests that other dopants be studied to be used as donors for the InGaAs QWs. The nearly total intermixing of the InGaAs-GaAs layers was observed from the heavily Be-doped MQW sample (at T_{Be} of 1004 °C) during materials growth, and this limits the Be doping density in the In-GaAs quantum wells.

The effect on laser performance (laser thresholds and emission spectra) by Si doping was demonstrated with an MBE-grown InGaAs-GaAs-AlGaAs strained-layer laser with a heavily Si-doped quantum well. The low threshold current of 48 mA and kink in the light versus current curve were observed from a gain-guided spin-on glass stripe laser. The shift in emission wavelength and two emission peaks were also observed. A much lower laser threshold is expected to be obtained with the introduction of index guiding such as impurity-induced layer disordering. The data presented in this paper should be important in the design of InGaAs-GaAs strained-layer lasers with doped quantum wells.

[1] S. E. Fischer, D. Fekete, G. B. Feak, and J. M. Ballantyne, Appl. Phys. Lett. 50, 714 (1987).
[2] J. N. Baillargeon, P. K. York, C. A. Zmudzinski, G. E. Fernandez, K. J. Beernink, and J. J. Coleman, Appl. Phys. Lett. 53, 457 (1988).
[3] R. M. Kolbas, N. G. Anderson, W. D. Laidig, Y. Sin, Y. Lo, K. Hsieh, and Y. Yang, IEEE J. Quantum Electron. QE-24, 1605 (1988).
[4] K. J. Vahala and C. E. Zah, Appl. Phys. Lett. 52, 1945 (1988).
[5] I. Suemune, L. A. Coldren, M. Yamanishi, and Y. Kan, Appl. Phys. Lett. 53, 1378 (1988).
[6] K. Uomi, T. Mishima, and N. Chinone, Appl. Phys. Lett. 51, 78 (1987).
[7] N. Holonyak, Jr., B. A. Vojak, H. Morkoc, T. J. Drummond, and K. Hess, Appl. Phys. Lett. 40, 658 (1982).
[8] Y. J. Mii, R. P. G. Karunasiri, K. L. Wang, and G. Bai, J. Vac. Sci. Technol. B 7, 341 (1989).
[9] N. Holonyak, Jr., and D. R. Scifers, Rev. Sci. Instrum. 42, 1885 (1971).

[10] R. A. Hamm, M. B. Panish, R. N. Nottenburg, Y. K. Chen, and D. A. Humphrey, Appl. Phys. Lett. 54, 2586 (1989).

[11] Y. Nashimoto, S. Dhar, W. P. Hong, A. Chin, P. Berger, and P. K. Bhattacharya, J. Vac. Sci. Technol. B 4, 540 (1986).

[12] A. S. Brown, G. W. Wicks, and L. F. Eastman, J. Vac. Sci. Technol. B 4, 543 (1986).

[13] Y. K. Su, M. C. Wu, C. H. Huang, and B. S. Chiu, J. Appl. Phys. 64, 2211 (1988).

[14] N. G. Anderson, Y. C. Lo, and R. M. Kolbas, Mater. Res. Soc. Symp. Proc. 77, 437 (1987).

[15] G. Borghs, K. Bhattacharyya, K. Deneffe, P. van Mieghem, and R. Mertens, J. Appl. Phys. 66, 4381 (1989).

[16] C. A. Warwick, H. Ono, M. Kuzuhara, and J. Matsui, Jpn. J. Appl. Phys. 26, L1398 (1987).

[17] Y. Pao, T. Hierl, and T. Cooper, J. Appl. Phys. 60, 201 (1986).

[18] F. Chambers and B. Vojak, Mater. Res. Soc. Symp. Proc. 77, 41 (1987).

[19] M. Kawabe, N. Shimizu, F. Hasegawa, and Y. Nannichi, Appl. Phys. Lett. 46, 849 (1985).

[20] Y. K. Sin and R. M. Kolbas (unpublished).

[21] G. A. Vawter, D. R. Myers, T. M. Brennan, B. E. Hammons, and J. P. Hohimer, Electron. Lett. 25, 243 (1989).

[22] H. C. Casey, Jr. and M. B. Panish, Heterostructure Lasers (Academic, New York, 1978), Part B, p. 256.

[23] H. Kressel and J. K. Butler, Semiconductor Lasers and Heterojunction LEDs (Academic, New York, 1977), p. 476.

[24] H. Kressel, Semiconductor Devices for Optical Communication, 2nd ed. (Springer, Berlin, 1982), p. 36.

[25] R. W. Dixon, F. R. Nash, R. L. Hartman, and R. T. Hepplewhite, Appl. Phys. Lett. 29, 372 (1976).

[26] K. Kobayashi, R. Lang, H. Yonezu, Y. Matsumoto, T. Shinohara, I. Sakuma, T. Suzuki, and I. Hayashi, IEEE J. Quantum Electron. QE-13, 659 (1977).

[27] A. A. Reeder, A. M. Mercy, and B. D. McCombe, IEEE J. Quantum Electron. QE-24, 1690 (1988).

[28] L. E. Eng, T. R. Chen, S. Sanders, Y. H. Zhuang, B. Zhao, A. Yariv, and H. Morkoc, Appl. Phys. Lett. 55, 1378 (1989).

[29] N. Holonyak, Jr., R. M. Kolbas, R. D. Dupuis, and P. D. Dapkus, IEEE J. Quantum Electron. QE-16, 170 (1980).

Enhanced/suppressed interdiffusion of lattice-matched and pseudomorphic III–V heterostructures by controlling Ga vacancies

R. M. KOLBAS, Y. L. HWANG, T. ZHANG, M. PRAIRIE, K. Y. HSIEH, U. K. MISHRA

Department of Electrical and Computer Engineering.
Center for Advanced Electronic Materials Processing.
North Carolina State University, Raleigh, NC 27695–7911, USA

Data are presented showing that the interdiffusion of Ga and Al (AlGaAs–GaAs) and of Ga and In (pseudomorphic InGaAs–GaAs) at a heterojunction can be significantly enhanced or suppressed by controlling group III vacancies and interstitials. High-resistivity low-temperature GaAs which contains excess As is shown to accelerate the interdiffusion process. The emission wavelength from monolayer-thick quantum wells can remain relatively unchanged even after annealing for 200 h at 850°C.

1. Introduction

The stability of lattice-matched [1–5] and lattice-mismatched [6–10] quantum well heterostructures is of interest for fundamental studies, the detrimental effects of intermixing during device processing and the application of intermixing to the development of new device structures. Intermixing can be enhanced with impurity-induced diffusion disordering or impurity-free vacancy-induced disordering, or intermixing can be suppressed by minimizing the free vacancies. Vacancies can be introduced by implantation, application of a selectively permeable mask or with overpressure in a closed ampule.

High-resistivity low-temperature GaAs (LT-GaAs) buffer layers [11] are becoming increasingly important, but their influence on the stability of heterojunctions is not well established. Monolayer-thick quantum wells [12, 13] are finding their way into increasing numbers of devices, but the impact of intermixing on monolayer-thick layers is not well documented. This work addressed these issues through experimental measurements and theoretical calculations. Vacancies (group III) were introduced by controlling the As overpressure in a sealed ampule and by the introduction of As-rich LT-GaAs, and vacancies were minimized using Ga overpressure.

2. Experimental methods

High-resistivity low-temperature GaAs materials used in this study were grown by molecular beam epitaxy on (100)-oriented GaAs substrates. The lattice-matched $Al_{0.31}Ga_{0.69}As$–GaAs single quantum well samples (9.5 nm) were grown at 640°C on undoped semi-insulating

---

substrates and the pseudomorphic $In_yGa_{1-y}As$–GaAs–AlGaAs ($y = 0.057, 0.113$ and 0.15) single quantum well samples (8.7 to 10.0 nm) were grown at 550°C for the InGaAs and 640°C for the AlGaAs on Si-doped substrates. The details of the growth condition and cross-sectional dark-field transmission electron microscope images of the samples can be found elsewhere [5, 14]. The details of the growth of the monolayer-thick quantum well samples and the LT-GaAs can also be found elsewhere [12, 13, 15, 16].

The samples were prepared for annealing by ultrasonic cleaning in trichloroethane, acetone, methanol and deionized water. The samples were placed in cleaned and etched (HF:HNO₃:H₂O = 1:1:1) quartz ampules (approximately 3.5 to 4cm³) and sealed under a vacuum of 0.13 mPa. Sufficient As (5 to 20 mg) or Ga (5 to 20 mg) was included to provide an excess overpressure of group V or group III atoms.

The amount of interdiffusion was determined based on the shift of the photoluminescence peak by solving the Schrödinger equation assuming an error function composition profile [17]. The photoluminescence spectra were taken at 77 K using a cavity-dumped Ar-ion laser ($\lambda = 514.5$ nm, 8 ns pulse at 3.8 MHz).

3. Determination of the interdiffusion coefficient

A very small amount of intermixing can produce a measurable shift in the photoluminescence peak from a quantum well heterostructure. The shift in the photoluminescence peak can be related to the intermixing by assuming that the as-grown quantum well is a square well and that the composition changes during interdiffusion according to $C(z) = C_0\{1 + 0.5 \, \mathrm{erf}\, [(z - L_z/2)/2(Dt)^{1/2}] - 0.5 \, \mathrm{erf}\, [(z + L_z)/2(Dt)^{1/2}]\}$, where C_0 is the initial Al composition in the cladding layer, L_z is the well thickness layer, t is the annealing time and erf (x) is the error function [18, 19]. The bound state and optical transition energies associated with the intermixed quantum well can be found by solving the Schrödinger equation numerically for the potential calculated from the composition profile. Although this is much more tedious than the closed-form approximations previously used, the numerical approach has been shown to be necessary for certain cases (e.g. small amounts of interdiffusion) which are of interest here [17]. In this work we followed the general ideas described by Hsieh [17] and have improved (in speed and accuracy) upon his approach by including a 'Richardson deferred approach to the limit, [20] to extrapolate the answer to the case of a zero step size in approximating the potential with small square steps.

4. Influence of overpressure conditions

The 77 K photoluminescence spectra from a 9.5 nm thick GaAs quantum well sandwiched between 0.5 μm thick $Al_{0.31}Ga_{0.69}As$ barriers is shown in Fig. 1a before and after annealing for 3 h at 950°C under various overpressure conditions. Note that the As overpressure condition (20 mg, As) results in a much greater shift than the Ga overpressure condition (20 mg, Ga). Also note that the photoluminescence peaks are only slightly broadened in spite of the high annealing temperatures. The interdiffusion coefficients and activation energies for this sample (and also a 7.3 nm sample) are shown in Fig. 1b. Note that Ga can significantly inhibit the interdiffusion, consistent with the model proposed by Deppe et al. [4]. When In overpressure is substituted for Ga overpressure the same general trends are observed, although the In is slightly less efficient in suppressing the interdiffusion in AlGaAs–GaAs samples. This supports the idea that group III vacancies and interstitials play an important role in the interdiffusion process.
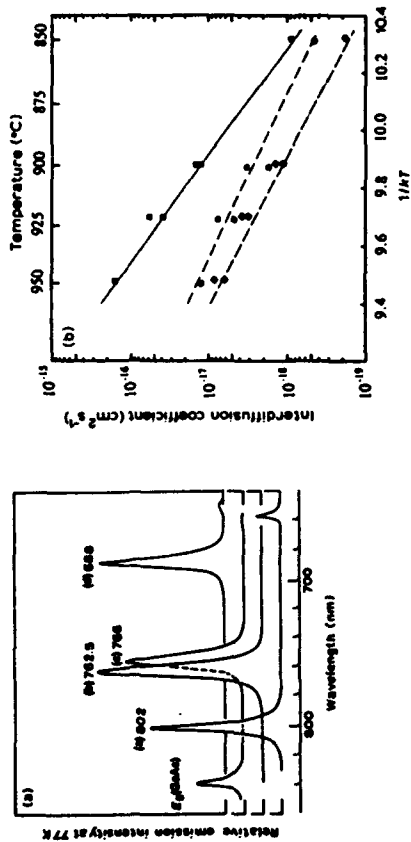
The effects of Ga (20 mg), As (20 mg) and no overpressure on the interdiffusion (850°C for 3 h) of InGaAs–GaAs–AlGaAs pseudomorphic quantum wells are shown in Fig. 2a. Again the most rapid intermixing occurs with As overpressure ($\Delta E = 101$ meV shift in photoluminescence peak), followed by no overpressure ($\Delta E = 68$ meV shift) and finally the least intermixing occurs with Ga overpressure ($\Delta E = 38$ meV shift). The interdiffusion of In and Ga at a pseudomorphic InGaAs–GaAs interface, however, is also dependent on the In alloy composition as shown in Fig. 2b. The data indicate that for higher In compositions the disordering is enhanced with As overpressure but, in contrast, under Ga overpressure the disordering is suppressed with increasing In composition [14]. These results can be understood in part using the ideas that the diffusion rate of group III atoms will be proportional to the group III defects [21] and that the diffusion of group III atoms can be enhanced by moving along the dislocations created by strain relaxation [9]. The calculated values of the activation energies for the case of $In_{0.15}Ga_{0.85}As$–GaAs in the range of $810 < T < 925°C$ are $E_{As} = 3.3$ eV, $E_{Ga} = 2.23$ eV and (not shown in Fig. 2b) $E_{none} = 1.56$ eV.

5. Effects of a low-temperature GaAs buffer layer

GaAs grown at a low temperature (200°C) by molecular beam epitaxy (LT-GaAs) has been shown to be highly resistive and optically inactive, which is attributed to the incorporation of excess As [22]. LT-GaAs has found wide applications in the improvement and development of electronic and optoelectronic devices [11, 16, 22]. Applications of LT-GaAs include electrical and optical isolation in integrated optoelectronic circuits. It is important to know how an LT-GaAs layer will influence the properties of the adjacent layers during elevated growth and device processing temperatures. Single GaAs quantum well samples were prepared on undoped (100)-oriented GaAs substrates by depositing a 0.5 μm LT-GaAs buffer layer at 200°C followed by 0.5 μm $Al_{0.3}Ga_{0.65}As$ ($T_s = 686°C$). 8.7 nm GaAs ($T_s = 628°C$) and finally 0.5 μm $Al_{0.35}Ga_{0.65}As$ ($T_s = 686°C$). Two sets of samples were prepared and differ only in that one set was *in situ* annealed at 580°C for 10 min under As overpressure immediately after the LT-GaAs layer was deposited (to help to stabilize the excess As). The sample cleaning, annealing conditions and testing procedures were as described previously except that the quantity of excess As or Ga was 5 mg and the annealing time was fixed at 4 h.

The 77 K photoluminescence data from the as-grown 8.7 nm single quantum well samples and the same samples subjected to various annealing ambients at 850°C are shown in Fig. 3a (with stabilization annealed LT-GaAs) and b (without stabilization annealing of the LT-GaAs). The photoluminescence line widths of the as-grown samples are comparable with those of samples grown without the LT-GaAs buffer layer (not shown), indicating that high-quality optical layers can be grown on top of LT-GaAs. Again, as in all previous cases, the least amount of intermixing occurs for the Ga overpressure case. In contrast, the extent of intermixing for the As and no overpressure case is reversed. This can be understood based on the fact that the magnitude of the intermixing in As overpressure is parabolic in nature [23]. The excess As in the ampule provides an overpressure of about 100 kPa which is less than the overpressure needed to reach the minimum. The LT-GaAs below the quantum well provides additional As which drives the system closer to the minimum than the no overpressure condition. A quantitative measurement of the effective As overpressure provided by the LT-GaAs was not performed.

The calculated values of the interdiffusion coefficient D are shown in Fig. 4a and b. Note that the intermixing is always less for the samples with the stabilization-annealed LT-GaAs
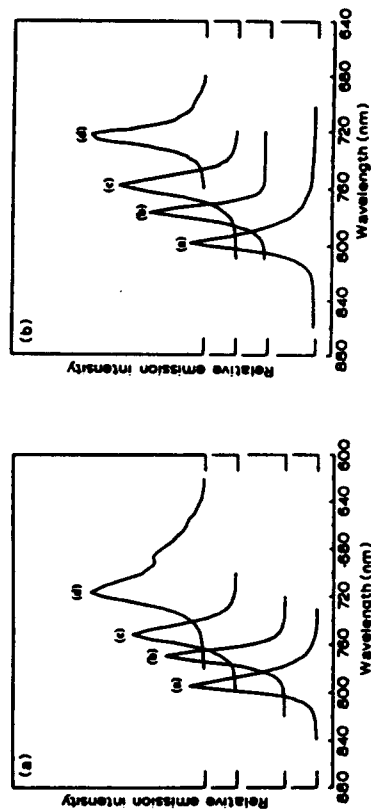
Figure 1 (a) Photoluminescence spectra (77 K) from an AlGaAs–GaAs single quantum well (9.5 nm) before and after thermal annealing (950°C for 3 h) in different overpressure environments: curves (a) not annealed, (b) Ga overpress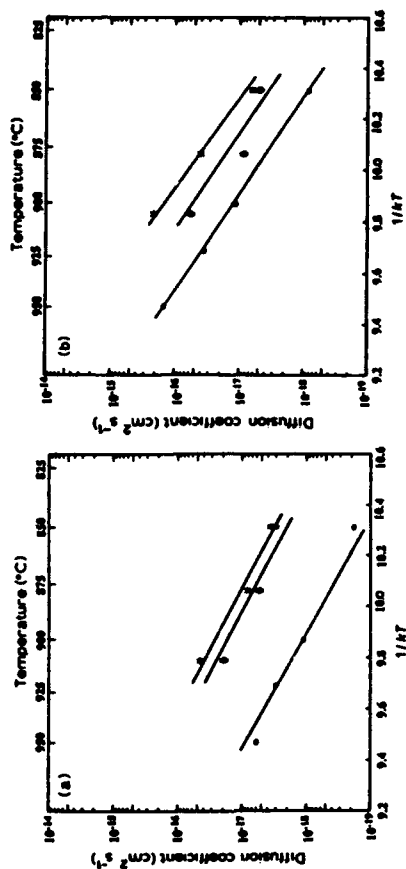ure, (c) no overpressure and (d) As overpressure. (b) Interdiffusion coefficients from a 9.5 nm well (open data points) and a 7.3 nm well (closed data points). The activation energies were 6.2, 4.38 and 4 eV for the As (□), Ga (◇) and no (○) overpressure conditions, respectively.
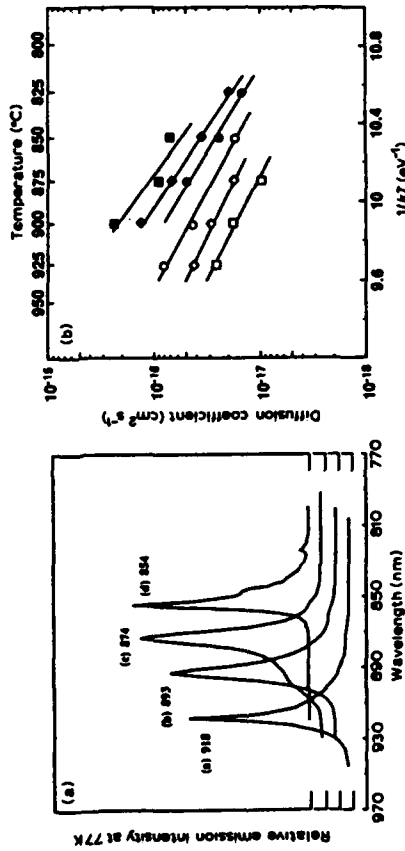
Figure 2 (a) Photoluminescence spectra (77 K) of an InGaAs–GaAs single quantum well (8.7 nm) before and after annealing (850°C for 3 h) in different overpressure environments: curves (a) not annealed, (b) Ga overpressure, (c) no overpressure and (d) As overpressure. Note that the line widths are preserved and the largest shift occurs for the As case. (b) Arrhenius plots of the interdiffusion coefficients for different In compositions: 15% (squares), 10% (diamonds) and 5.7% In (circles); Ga overpressure (open symbols) and As overpressure (closed symbols); $L_z = 10$ nm. Note the difference in the magnitude and dependence of D on the In composition for the As and Ga overpressure conditions.
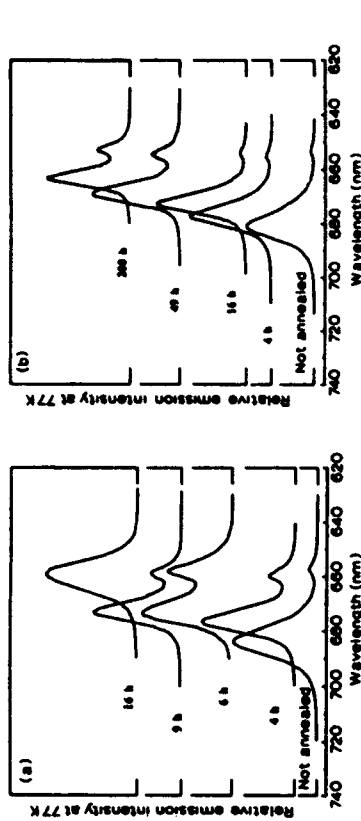
Figure 5 Photoluminescence spectra (77 K) from a 3ML thick AlGaAs–GaAs quantum well before and after annealing (850°C) in (a) an As overpressure and (b) a Ga overpressure. Note the relatively small shift in the emission wavelength after 200 h of annealing at 850°C in Ga overpressure.

exhibit the largest shifts in emission wavelength [24], although it is not necessary to invoke well-width-dependent exciton energies to explain the phenomena.

The sample used in this study consisted of a symmetric separate-confinement single quantum well heterostructure $Al_{0.6}Ga_{0.4}As–Al_xGa_{0.9}As$–GaAs of thickness 600 nm–50 nm–3 monolayers (ML), respectively, where 1 ML = 0.28267 nm. The low threshold laser performance of this same 3ML has been reported previously [12]. The 77 K photoluminescence peaks versus annealing time at 850°C in excess As (5 mg) and excess Ga (5 mg) overpressure are shown in Fig. 5a and b, respectively. Again, the mixing in an As overpressure is quite rapid whereas the mixing in a Ga overpressure is significantly slower. The total shift after 200 h in Ga overpressure is only about 15 nm, which is relatively small compared with the large shifts observed for other samples with thicker quantum wells. In fact, the maximum theoretical shift for this 3ML quantum well is approximately 20 nm,
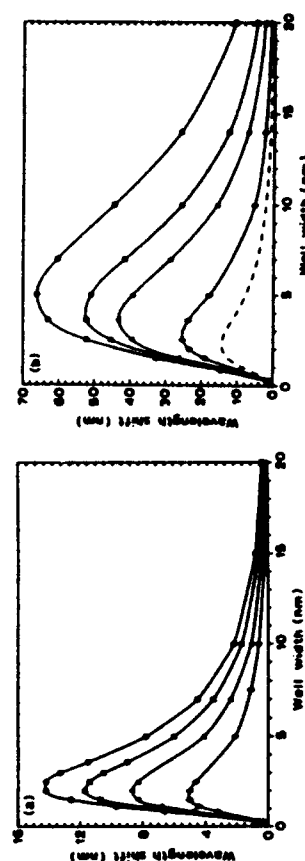

Figure 6 Calculated wavelength shift as a function of well width for different times and temperatures at (a) 850°C ($D = 8.5 \times 10^{-19} \text{cm}^2 \text{s}^{-1}$) and (b) 950°C ($D = 1.3 \times 10^{-18} \text{cm}^2 \text{s}^{-1}$). Note that thin wells (<1 nm) and thick wells (>10 nm) are relatively insensitive compared with wells in the 2 to 10 nm range. (a) 60 (○), 45 (□), 30 (▲) and 15 min (○); (b) 10 (○), 5 (□), 3 (▲) and 1 min (○), and 60 min at 950°C (−−−).

Figure 3 Photoluminescence spectra (77 K) for an AlGaAs–GaAs single quantum well sample with an LT-GaAs buffer layer (a) with *in situ* stabilization annealing and (b) without stabilization annealing, before and after thermal annealing at 850°C for 4 h in different overpressure ambients: curves (a) as grown, (b) Ga overpressure, (c) As overpressure and (d) no overpressure.

Figure 4 Interdiffusion coefficients of the group III atoms under (a) Ga and (b) As overpressure for the two samples in Fig. 3 (annealed (■) and unannealed (●) buffer) and an identical sample without an LT-GaAs buffer (○).

buffer layer, owing to the reduction of mobile As (or its related defects) after *in situ* annealing. Even with stabilization annealing the intermixing is more rapid than in samples without LT-GaAs. Hence, it will be necessary to improve the stabilization-annealing process or to find ways to prevent the outdiffusion of As (or it related defects) in order to realize fully the benefits of LT-GaAs [16].

6. Intermixing of monolayer-thick quantum wells

On first thought one would expect the intermixing problem to get worse for thin quantum wells. However, it has been demonstrated experimentally that wells of intermediate width

which corresponds to complete intermixing with the $Al_xGa_{1-x}As$ confining layers. The shift in emission wavelength can be quite small for ultrathin quantum wells because the $n = 1$ bound state is already close to the top of the well.

The calculated wavelength shift versus well width for a series of different times and temperatures is shown in Fig. 6a (850°C) and b (950°C). The value $D = 8.5 \times 10^{-19}$ cm² s⁻¹ is based on the work of Hsieh [17] for the As overpressure condition. These curves predict that the wavelength shift for thick wells (> 10 nm) and ultrathin wells (< 1 nm) is much less than for wells of intermediate thickness (1 to 5 nm). The worst-case well thickness with respect to intermixing is not fixed but increases slightly (Fig. 6b) as the time or the diffusion coefficient is increased. these curves can be generalized to other values of D by realizing that they are really only dependent on the product Dt, and are thus applicable to a variety of thermal and rapid thermal annealing conditions if D is known.

7. Summary

Interdiffusion at AlGaAs–GaAs and InGaAs–GaAs heterojunctions can be enhanced or suppressed by controlling the group III vacancies and interstitials. The interdiffusion coefficient for pseudomorphic $In_xGa_{1-x}As$–GaAs heterojunctions increases with increasing In composition under As overpressure but decreases with increasing In composition under Ga overpressure. High-quality quantum wells can be grown on top of LT-GaAs, but more rapid intermixing occurs in the presence of a LT-GaAs buffer layer. Finally, calculations consistent with the experimental thermal annealing data, indicate that quantum wells in the range 1 to 5 nm are the most sensitive to shift in the emission wavelength, whereas ultrathin and very thick wells are the least sensitive.

References

1. L. L. CHANG and A. KOMA, *Appl. Phys. Lett.* 29 (1976) 138.
2. W. D. LAIDIG, N. HOLONYAK, JR, M. D. CAMRAS, K. HESS, J. J. COLEMAN, P. D. DAPKUS and J. BARDEEN, *ibid.* 38 (1981) 776.
3. W. D. LAIDIG and N. HOLONYAK, JR, *J. Electron. Mater.* 11 (1982) 1.
4. D. G. DEPPE, L. J. GUIDO and N. HOLONYAK, JR, *Materials Research Society meeting*, April, Reno Nevada, 1988.
5. K. Y. HSIEH, Y. C. LO, J. H. LEE and R. M. KOLBAS, International Symposium on GaAs and Related Compounds, Atlanta, Georgia, Sept. 1988, Institute of Physics Conference Series vol. 96 (Institute of Physics, Bristol, 1988) p. 393.
6. M. D. CAMRAS, N. HOLONYAK, JR, K. HESS, M. J. LUDOWISE, W. T. DIETZE and C. R. LEWIS, *Appl. Phys. Lett.* 42 (1983) 185.
7. J. S. MAJOR, JR, L. J. GUIDO, K. C. HSIEH, N. HOLONYAK, JR, W. STUTIUS, P. GAVRILOVIC and J. E. WILLIAMS, *ibid.* 54 (1989) 913.
8. K. J. BEERNINK, P. K. YORK, J. J. COLEMAN, R. G. WATERS, J. KIM and C. M. WAYMAN, *ibid.* 55 (1989) 2167.
9. J. S. MAJOR, JR, L. J. GUIDO, N. HOLONYAK, JR, K. C. HSIEH, E. J. VESELY, D. W. NAM, D. C. HALL, J. E. BAKER, P. GAVRILOVIC, K. MEEHAN, W. STUTIUS and J. E. WILLIAMS, *J. Electron. Mater.* 19 (1990) 59.
10. J. S. MAJOR, JR, D. C. HALL, L. J. GUIDO, N. HOLONYAK, JR, P. GAVRILOVIC, K. MEEHAN, J. E. WILLIAMS and W. STUTIUS, *Appl. Phys. Lett.* 55 (1989) 271.
11. F. W. SMITH, A. R. CALAWA, C. L. CHEN, M. J. MANFRA and L. J. MAHONEY, *IEEE Electron. Device Lett.* EDL-9 (1988) 77.
12. J. H. LEE, K. Y. HSIEH, Y. L. HWANG and R. M. KOLBAS, *Appl. Phys. Lett.* 56 (1990) 626.
13. J. H. LEE, K. Y. HSIEH and R. M. KOLBAS, *Phys. Rev.* B41 (1990) 7678.
14. K. Y. HSIEH, Y. L. HWANG, J. H. LEE and R. M. KOLBAS, *J. Electron. Mater.* 19 (1990) 1417.
15. Y. L. HWANG, K. Y. HSIEH, J. H. LEE, T. ZHANG, U. K. MISHRA and R. M. KOLBAS, in Proceedings of the 6th International Conference on Semi-insulating III–V Compounds, Toronto, Canada (1990) (IOP Publishers Ltd) p. 77.
16. L. W. YIN, Y. L. HWANG, J. H. LEE, R. M. KOLBAS, R. J. TREW and U. K. MISHRA, *IEEE Electron. Device Lett.* 11(12) (1990) 561.
17. K. Y. HSIEH, PhD thesis, North Carolina State University (1989).
18. J. CRANK, 'The Mathematics of Diffusion' (Oxford University Press, London, 1957).
19. J. CIBERT, P. M. PETROFF, D. J. WERDER, S. J. PEARTON, A. C. GOSSARD and J. H. ENGLISH, *Appl. Phys. Lett.* 49 (1986) 223.
20. W. H. PRESS, B. P. FLANNERY, S. A. TEUKOLSKY and W. T. VETTERLING, 'Numerical Recipes, the art of Scientific Computing' (Cambridge University Press, Cambridge, 1988).
21. D. G. DEPPE and N. HOLONYAK, JR, *J. Appl. Phys.* 64 (1988) R93.
22. M. KAMINSKA, Z. LILIENTAL-WEBBER, E. R. WEBBER, T. GEORGE, J. B. KORTRIGHT, F. W. SMITH, B. Y. TSAUR and A. R. CALAWA, *Appl. Phys. Lett.* 54 (1989) 1881.
23. L. J. GUIDO, N. HOLONYAK, JR, K. C. HSIEH, R. W. KALISKI, W. E. PLANO, R. D. BURNHAM, R. L. THORNTON, J. E. EPLER and T. L. PAOLI, *J. Appl. Phys.* 61 (1987) 1372.
24. B. ELMAN, E. S. KOTELES, P. MELMAN and C. A. ARMIENTO, *ibid.* 66 (1989) 2104.

Enhanced/Suppressed Interdiffusion of InGaAs-GaAs-AlGaAs Strained Layers by Controlling Impurities and Gallium Vacancies

K. Y. HSIEH and Y. L. HWANG

Department of Materials Science and Engineering
North Carolina State University, Raleigh, NC 27695-7907

J. H. LEE and R. M. KOLBAS

Department of Electrical and Computer Engineering
National Science Foundation Engineering Research Centers
for Advanced Electronic Materials Processing
North Carolina State University, Raleigh, NC 27695-7911

The interdiffusion of In and Ga at an InGaAs-GaAs interface subjected to different annealing temperatures, times, and environments is demonstrated. The interdiffusion coefficients and activation energies are determined by correlating the shift in the photoluminescence peaks with the calculated quantum well transition energies based on an error function composition profile. The results indicate that a higher In composition $In_xGa_{1-x}GaAs$ single quantum well (SQW) leads to a higher interdiffusion coefficient of In and Ga in an As overpressure annealing condition. Also, As overpressure increases the interdiffusion, whereas Ga overpressure reduces the interdiffusion. The thermal activation energies for different In composition InGaAs-GaAs SQW's ($x = 0.057$, 0.10, 0.15) range from 3.3 to 2.6 eV for an As overpressure environment and from 3 to 2.23 eV for the Ga overpressure situation. With respect to impurity induced disordering by Zn using a Ga or As overpressure significantly effects the depth of the Zn diffusion front but significant mixing does occur in either case when the impurity front reaches the quantum well.

Key words: In-Ga interdiffusion, thermal annealing, quantum well structure, impurity diffusion, diffusion induced disordering

INTRODUCTION

There is a strong interest in the optoelectronic properties of strained layer quantum well heterostructures (QWH's) resulting from the relaxation of the lattice-match constraint and the introduction of strain which produces new and useful properties.[1-4] The stability of lattice-matched[5-9] and lattice-mismatched[10-14] QWH's to thermal- or diffusion-induced compositional disordering is of great interest for fundamental material studies and possible problems in the fabrication and reliability of devices. High performance strained layer InGaAs-GaAs quantum well lasers have also been reported.[13,15-17] In spite of the strain, strained layer InGaAs-GaAs QWH's wells are almost as stable as lattice-matched AlGaAs-GaAs QWH's to thermal disordering.[13] However, very few reports mention the diffusion coefficient and activation energy of the In and Ga in the InGaAs-GaAs strained layer interfaces. Only Joncour et al.[18] have reported the interdiffusion coefficient D_{In-Ga} of InGaAs-GaAs strained-layer superlattice (SLS) at 850° C measured by x-ray diffraction. In this work, we report

the systematic study of the thermal interdiffusion (In and Ga) and impurity enhanced disorder at the quantum well heterointerface under the influence of the annealing environment. The relationships between the interdiffusion coefficient D_{In-Ga} and the In mole fraction of the InGaAs-GaAs strained layer QWH's are also addressed.

CRYSTAL GROWTH AND DIFFUSION

All the InGaAs-GaAs SQW's for this experiment were grown by molecular beam epitaxy (Varian 360) on Si-doped (100)-oriented GaAs substrates. The growth temperature for the InGaAs-GaAs layers was 550° C, and for the AlGaAs layers, the temperature was fixed at 640° C. During the growth of the AlGaAs-GaAs interfaces, stop growth was carried out while the temperature was decreased from 640 to 550° C or while it was increased from 550 to 640° C.

Two different SQW structures were studied. The first has 0.5-μm thick $Al_xGa_{1-x}As$ ($x = 0.35$) cladding layers surrounding two 1500Å thick GaAs confining layers and an 87- to 100Å $In_xGa_{1-x}As$ ($x = 0.057$, 0.113, 0.15) well centrally located between the two GaAs confining layers. In the second structure, there were no AlGaAs cladding layers. The samples

were grown by first depositing a 0.5-μm GaAs layer, then a 100Å $In_xGa_{1-x}As$ (x = 0.15) well, and finally another 1200 or 600Å GaAs cap layer. To improve the interface quality a brief (<1 sec) interruption of the growth is carried out at the InGaAs-GaAs interface.

For both thermal annealing (impurity-free) and Zn diffusion experiments, the samples were ultrasonically cleaned in trichloroethane, acetone, and methanol, and washed in distilled water. The samples were placed in cleaned and etched ($HF:HNO_3:H_2O$ = 1:1:1) quartz ampoules (approximately 3.5–4 cm^3) and sealed under a vacuum of 10^{-7} Torr. Sufficient As (20 mg) or Ga (20 mg) or Zn was included to provide an excess overpressure. For the thermal annealing, the annealing temperatures and times varied in the range from 750 to 925° C and from 3 to 5 hours. Samples keep their mirror like surface after thermal annealing in both the As and Ga overpressure environments. However, for a temperature exceeding 700° C significant surface degradation was observed for samples in the no over pressure environment. With respect to low temperature Zn diffusion, the diffusion time employed was 1 hour for all cases and the diffusion temperature was 600 to 650° C.

To study the effects of thermally-induced or impurity-induced disordering in a SQWH, photopumping was employed and the change in photoluminescence emission energy was recorded. The photoluminescence spectra were taken with the samples cooled to 77 K and photoexcited with a cavity-pumped argon-ion laser (λ = 5145Å, 8-ns pulse at 3.8 MHz). The spectra were recorded using a 0.5-m spectrometer and an S-1 photomultiplier.

STRUCTURE ANALYSIS AND THERMAL DISORDERING

A cross-sectional dark field TEM (Transmission Electron Microscopy) image of the $In_xGa_{1-x}As$-GaAs (x = 0.15) single quantum well is shown in Fig. 1(a). Both the absence of dislocations at the interfaces as seen in the TEM image and a sharp peak in the photoluminescence spectrum (Fig. 1(b)) indicate that the 100Å InGaAs SQW is of high crystalline quality.

Before annealing the SQWH can be modeled as a finite square-well potential. The potential well depth is determined from the conduction and val ... oand discontinuities for the electrons and holes, respectively. The carrier mass used in the Schrödinger wave equation is the carrier effective mass in GaAs for the barrier regions and in the $In_xGa_{1-x}As$ for the quantum well. The thermal annealing process changes the composition profile across the quantum well structure through the solid state diffusion of In and Ga. The composition profile will then determine the potential energy profile confining the carriers. The spatial profile of the In composition C, across a well centered at z = 0 is described by[19,20]
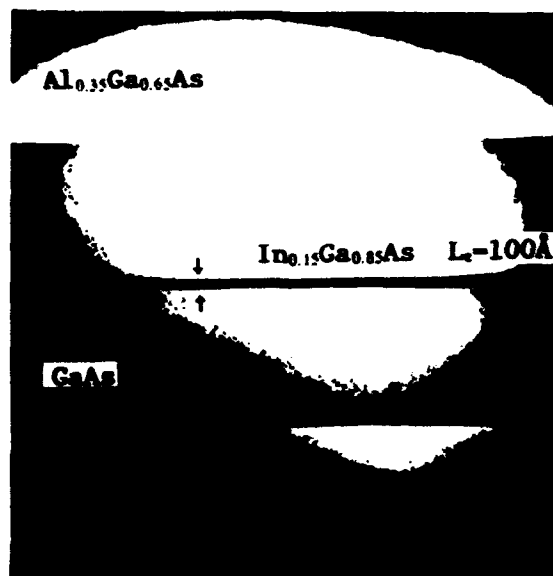
(a)
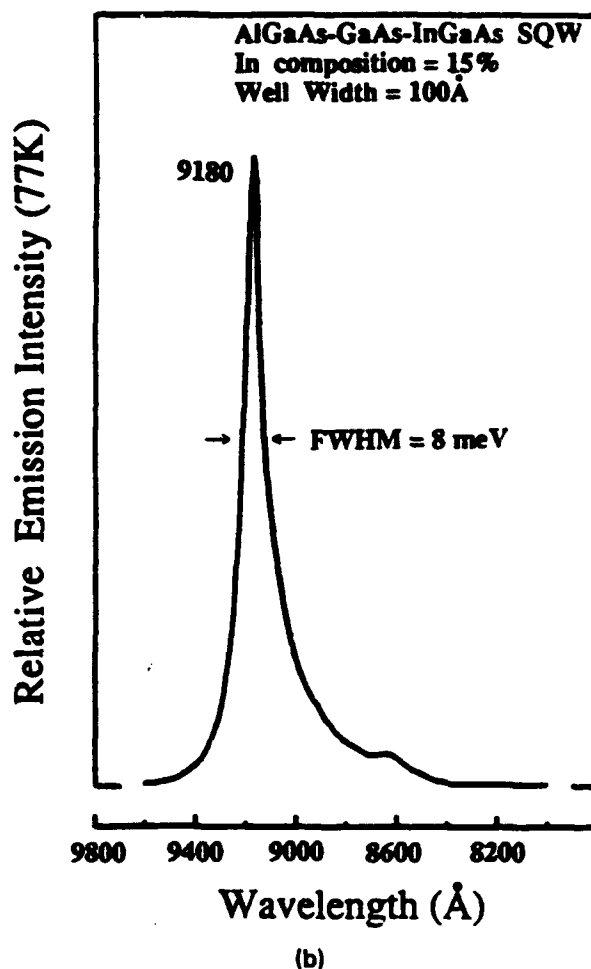
(b)

Fig. 1 — (a) Cross-sectional dark field TEM photomicrograph of a 100Å $Al_{0.35}Ga_{0.65}As$-GaAs-$In_{0.15}Ga_{0.85}As$ SQW. (b) Photoluminescence spectrum (77K) of the SQW. The absence of dislocations at the interfaces and the sharp PL peak indicate a high quality SQW crystal.

$$C(z) = C_o \left[1 + \frac{1}{2} erf\left(\frac{z - L_z/2}{\sqrt{2Dt}}\right) \right.$$

$$\left. - \frac{1}{2} erf\left(\frac{z + L_z/2}{\sqrt{2Dt}}\right) \right] \qquad (1)$$

where C_o is the initial In composition in the quantum well, L_z is the well thickness, D_{In-Ga} is the interdiffusion coefficient, t is the annealing time, and $erf(z)$ is the error function. If the initial well width is known, the shift in the quantum well emission after thermal annealing will depend on the values of D_{In-Ga} and t. The interdiffusion coefficient D_{In-Ga} can be determined by varying D_{In-Ga} until a match is obtained between the experimental and calculated transition energies. The bound state energy transition levels of an annealed SQWH are found using a potential profile that is calculated using Eq. (1) and the dependence of the bandgap on the In mole fraction x.[31] Given the electron and heavy hole effective masses, $m_e^* = 0.0665 - 0.0435x$ and $m_{hh}^* = 0.45 - 0.04x$, respectively, and the band offsets[22] of $\Delta E_c = 0.7E_g$ and $\Delta E_v = 0.3\Delta E_g$, the bound state energies can be calculated using iterative techniques. Calculation of the radiative transition energy consists of adding the electron sub-band energy, the heavy hole sub-band energy, and the energy gap corresponding to the In concentration at the well center.

The 77K photoluminescence spectra from an $In_{0.15}Ga_{0.85}As$ SQW are shown in Fig. 2 for samples processed as follows: (a) as grown, (b) Ga overpressure, (c) As overpressure, and (d) no overpressure. The annealing temperature was 850° C and the annealing time was 3 hours. The largest shift in wavelength (9180 to 8540Å) or energy ($\Delta E = 101$ meV)
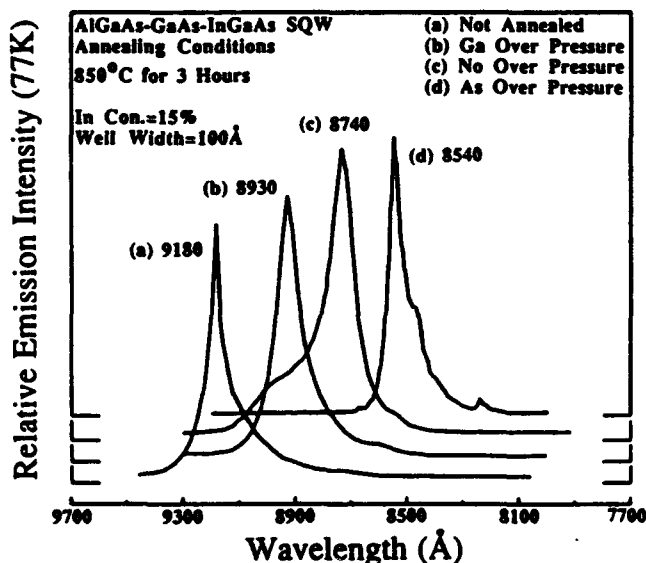
corresponds to the greatest In-Ga interdiffusion which occurs when the sample is annealed with an As overpressure. In contrast, the least interdiffusion (9180 to 8930Å, $\Delta E = 38$ meV) occurs with Ga overpressure. These results indicate that the compositional disordering process is significantly affected by the overpressure conditions for thermal disordering (i.e., when no impurity-induced disordering occurs). These results are consistent with those observed for the AlGaAs-GaAs lattice-matched system.[9]

The calculated values of the diffusion coefficients D_{In-Ga} for the $In_{0.15}Ga_{0.85}As$-GaAs are plotted versus $1/kT$ ($810 < T < 925°$ C) in Fig. 3. A least-squares fit of the data yields activation energies of $\Delta E_{(As-rich)} = 3.3$eV, $\Delta E_{(no\ overpressure)} = 1.56$eV, $\Delta E_{(Ga-rich)} = 2.23$eV. To our knowledge, this is the first study of the influence of Ga overpressure on the interdiffusion of In and Ga in InGaAs. In addition this is the first report of the activation energies of In and Ga interdiffusion under different annealing environments.

The interdiffusion coefficient of In and Ga in the InGaAs is not only affected by the annealing environment but also related to the In concentration in the InGaAs alloy. The relation between the interdiffusion coefficient and the In concentration in the InGaAs SQW is shown in Fig. 4. The data indicate that for high In compositions in the InGaAs well the disordering process is enhanced with As overpressure. On the contrary, under Ga overpressure the disordering process is suppressed with increasing In composition. These results will be discussed later.

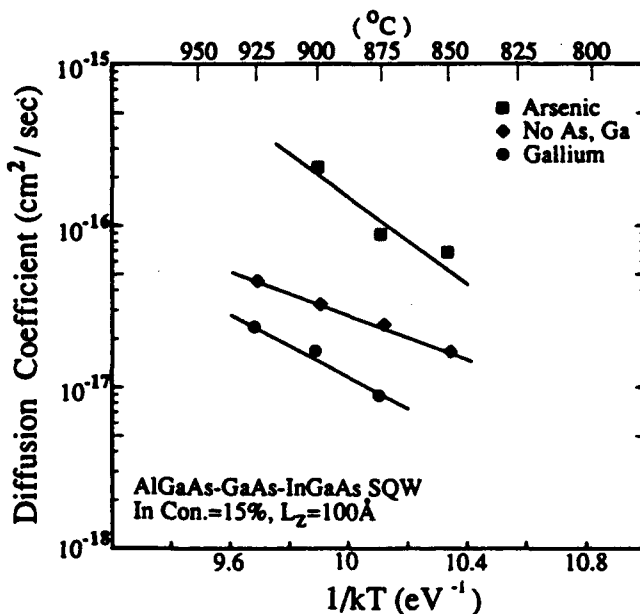Both AlGaAs-GaAs-InGaAs SQW and GaAs-

Fig. 2 — Photoluminescence spectra (77K) of the SQW samples, before and after thermal annealing at 850° C for 3 hr in different overpressure environments. Note the large difference between the As and Ga curves with respect to the shift in the emission peaks.

Fig. 3 — Plot of the interdiffusion coefficient of In and Ga in an $Al_{0.3}Ga_{0.7}As$-GaAs-$In_{0.15}Ga_{0.85}As$ SQW, for different overpressure environments as function of $1/kT$. A least-squares fit to the data yields activation energies of $\Delta E_{(As\ rich)} = 3.3$ eV, $\Delta E_{(Ga\ rich)} = 2.23$ eV, and $\Delta E_{(no\ overpressure)} = 1.56$ eV.
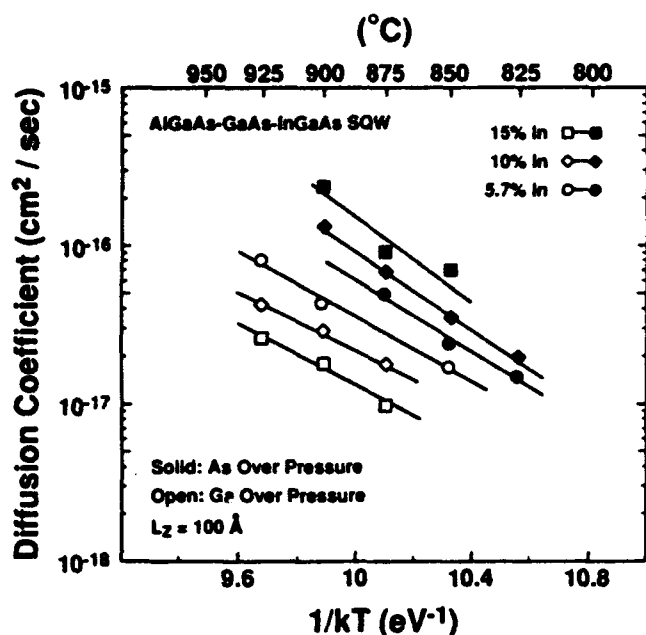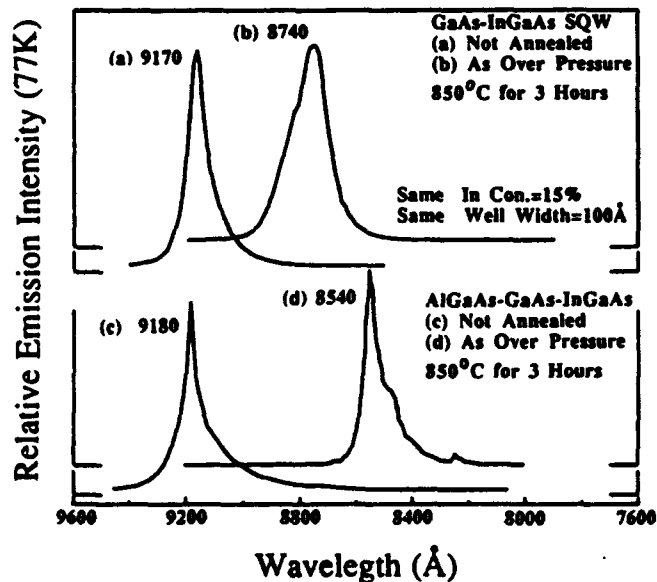
Fig. 4 — Arrhenius plots of the diffusion coefficients to fit the interdiffusion of different In composition $Al_yGa_{1-y}As$-GaAs-$In_xGa_{1-x}As$ SQW ($y = 0.35$; $x = 0.057$, 0.10, 0.15) in As overpressure and in Ga overpressure conditions. Note that the interdiffusion coefficients increase with increasing In concentration in an As overpressure environment and reduce with increasing In composition in a Ga overpressure condition.

InGaAs SQW samples were evaluated. The well width ($L_z = 100$Å) and the In concentration ($x = 0.15$) in the well are the same for these two different SQW samples. The photoluminescence spectra for these two samples, as-grown and after annealing (850° C, 3 hours, As overpressure), are shown in Fig. 5. For the samples which had $Al_xGa_{1-x}As$ cladding layers, the peak shift is larger than the sam-

ples that only had GaAs barrier layers. Following the same technique presented above, the interdiffusion coefficient and the activation energy were determined. The results show that samples with AlGaAs layers have a larger interdiffusion coefficient D_{In-Ga} (Fig. 6). Since the AlGaAs-GaAs-InGaAs SQW crystal has AlGaAs cladding layers, the diffusion between Ga and Al atoms at the AlGaAs-GaAs interface should also occur during annealing. The photoluminescence spectrum only provides the bound state energy information from the InGaAs well. Hence we don't know what is happening at the AlGaAs-GaAs interfaces. However, by comparing the shift in the photoluminescence peak of the two samples we observe more rapid disordering of the InGaAs well in the samples with AlGaAs cladding layers. To investigate this further, additional samples with the same basic structure but with 200Å (rather than 1500Å) GaAs confining layers were evaluated. Subjecting these new samples to the same annealing conditions resulted in larger shifts in the photoluminescence peaks (150Å difference). Hence, the closer proximity of the AlGaAs-GaAs heterojunction enhances the intermixing. This could be due to the presence of Al atoms that diffuse to the InGaAs-GaAs interface or a modification of the concentration and movement of point defects due to the adjacent of AlGaAs.

Deppe et al.[23] suggested that the diffusion rate of the Column III lattice atom will be proportional to the concentration of the Column III point defects. Major et al.[13] also pointed out that the diffusion of the Column III atom can be enhanced by moving along the dislocation created through strain relaxation. We can apply both ideas below to explain the
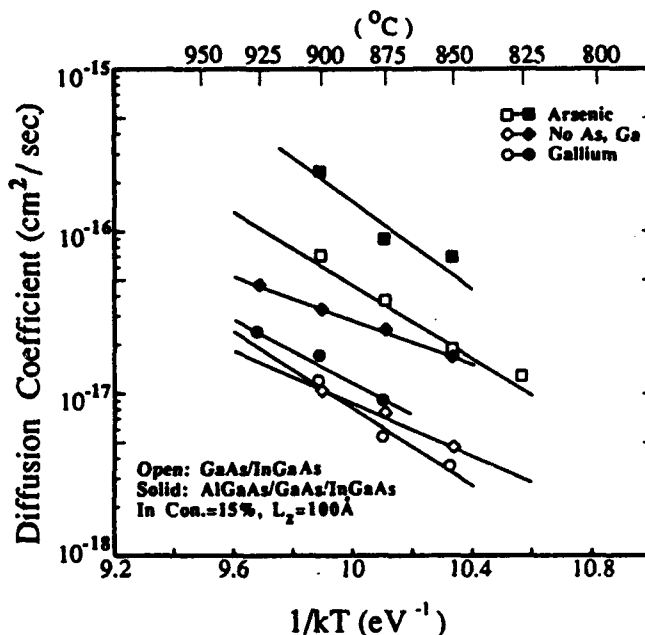

Fig. 5 — Photoluminescence spectra (77K) of the SQW samples, before and after thermal annealing at 850° C for 3 hr in an As overpressure condition. The sample with a separate confinement structure (AlGaAs-GaAs-InGaAs) had a larger shift in the emission peak.

Fig. 6 — Plot of the interdiffusion coefficient of In and Ga in the $Al_{0.35}Ga_{0.65}As$-GaAs-$In_{0.15}Ga_{0.85}As$ SQW and the GaAs-$In_{0.15}Ga_{0.85}As$ SQW for different overpressure environments as a function of 1/kT. Interdiffusion always occurs faster in the separate confinement heterostructure.

In-Ga interdiffusion as a function of overpressure and In concentration.

The relation between the interdiffusion and the In concentration in the InGaAs SQW has already been shown in Fig. 4. Note that the interdiffusion coefficient D_{In-Ga} increases with increasing In mole fraction in the InGaAs alloy in an As overpressure condition. On the contrary, under Ga overpressure the InGaAs-GaAs well with high In composition is more stable than that with low In composition.

There are at least two factors that determine the behavior of the interdiffusion of In and Ga at the InGaAs-GaAs interfaces. One is the strain which can produce dislocations during annealing when the lattice relaxes[13] and the other is the Ga vacancy concentration controlled by the over pressure conditions. For the In atoms to pass through the interface and exchange with Ga atoms they need to find a vacancy on a neighboring site. An As overpressure provides a high Ga vacancy concentration. This condition provides enough driving force to enhance the disordering process. Simultaneously, the strain can create a dislocation network during the strain relaxation[13] and then provide a diffusion vehicle for the Column III atoms. Since a high In fraction is associated with a high strain, it will generate more dislocations. Both conditions help the disordering process to proceed faster. In contrast Ga overpressure dramatically reduces the Ga vacancy concentration resulting in fewer sites into which the In or Ga atoms can jump across the interface and settle. In this case even if the strain relaxation provides diffusion pipes[13] for the Column III atoms, limited

Ga vacancies slowed down the diffusion process. Hence the speed of interdiffusion of the Column III atoms across the interface is reduced. Based on this model, we would expect an $In_xGa_{1-x}As$ SQW to have a larger interdiffusion coefficient in an As overpressure compared to a Ga overpressure, and a high interdiffusion coefficient for a higher In composition in an As overpressure which are observed experimentally. The model is not sufficiently robust to explain why high In composition interface are more stable in a Ga overpressure.

An important result to note is that for low In composition $In_xGa_{1-x}As$-GaAs SQW's ($x = 0.057$), the thermal disordering process was not sensitive to the annealing environment. The 77K photoluminescence spectra from $In_xGa_{1-x}As$/GaAs SQW's ($x = 0.057$) after 3 hours at 850° C in different overpressure conditions are shown in Fig. 7. The shifts in the photoluminescence peaks were nearly the same for both Ga and As overpressure conditions for the low In composition samples. In contrast, the interdiffusion coefficient for the high In composition ($x = 0.15$) SQW in an As overpressure condition is almost one order magnitude larger than in a Ga overpressure condition.

IMPURITY INDUCED DISORDERING

A lot of work has been done on compositional disordering with Zn impurity diffusion in lattice-match[5–9] and lattice-mismatched[10,24] QWH. In order to better understand the role of Ga and As overpressure in controlling the interdiffusion process, we also performed the Zn impurity induced disordering experiments in various overpressure conditions.
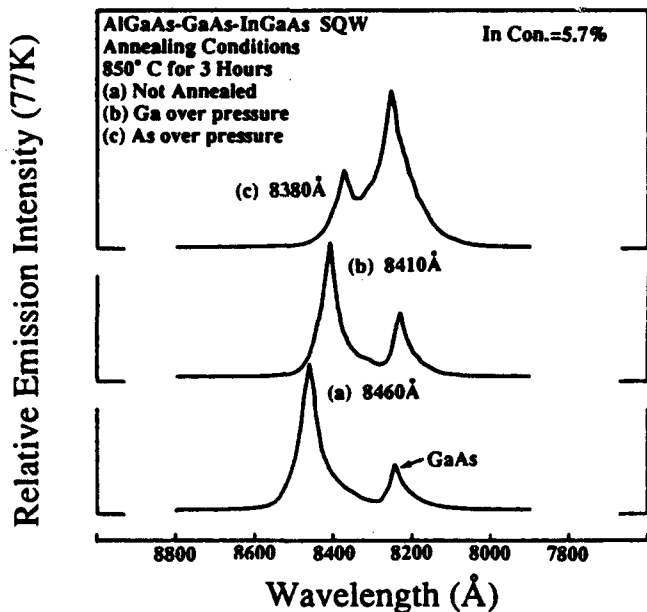

Fig. 7 — Photoluminescence spectra (77K) from a set of $Al_{0.36}Ga_{0.65}As$-GaAs-$In_{0.057}Ga_{0.943}As$ SQW samples cleaved from a single wafer, before and after thermal anneling at 850° C for 3 hr in different overpressure environments. Note the small difference between the As and Ga curves with respect to the shift in the emission peaks. This result indicates for the low In composition SQW's, the interdiffusion process was not sensitive to the overpressure condition.
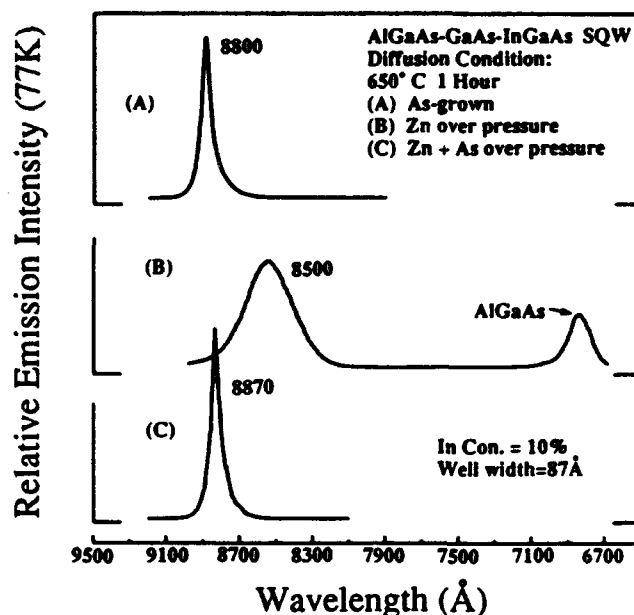

Fig. 8 — 77K photoluminescence spectra for $Al_{0.36}Ga_{0.65}As$-GaAs-$In_{0.1}Ga_{0.9}As$ SQW following impurity diffusion with different overpressure conditions. The emission peak did not shift in an As and Zn overpressure condition due to a shallow diffusion front.

The 77K photoluminescence spectra from an $In_{0.1}Ga_{0.9}As$ SQW are shown in Fig. 8 for samples processed as follows: (a) as grown, (b) Zn overpressure, (c) Zn and As overpressure. The annealing temperature was 650° C and the annealing time was 1 hour. With Zn overpressure, the photoluminescence spectrum broadens and the peak shifts to shorter wavelengths indicating partial mixing due to the impurity diffusion. During annealing if we also put extra As into the ampoule with the Zn source, the heterointerfaces are not mixed and the photoluminescence is the same as the as-grown samples (Fig. 8(c)). Shih[26] reported that the diffusion of Zn in GaAs was affected by the Ga vacancy concentration, which in turn was governed by the As pressure. We observed that the diffusion profile changed gradually as extra As was added. Compositional disordering will not take place until the Zn diffusion front passes through the interfaces. For the sample annealed under Zn and extra As ambient, the Zn diffusion front did not reach the well. Hence the photoluminescence measurement was the same as the unannealed samples.

A thin SQW is good for measuring a slight amount of interdiffusion, while a thick SQW is appropriate for conditions that produce rapid interdiffusion. Hence a sample with several SQW's with different thicknesses would be useful to gauge a wide range of disordering mechanisms. A sample with three $In_{0.15}Ga_{0.85}As$ SQW's of different well widths (L_z = 50, 85, and 200Å) separated by 2000Å GaAs barriers was used to evaluate the effect of Zn impurity diffusion. The 77K photoluminescence spectra are shown in Fig. 9 for the as-grown sample, (a), and for samples diffused for 1 hour at 600° C with (b)

$ZnAs_2$ and (c) $ZnAs_2$ and Ga. With $ZnAs_2$ overpressure the two thin wells were almost completely mixed leaving only the 200Å well peak. Compared with the as-grown sample, the 200Å well photoluminescence peak (Fig. 9(b)) shifted 160Å (9400 to 9240Å). For the $ZnAs_2$ with extra Ga annealing condition, the peaks from the 50 and 85Å wells also disappeared and the 200Å well peak shifted 240Å from 9400 to 9160Å. The degree of disordering was larger than in the $ZnAs_2$ annealing condition. For the $ZnAs_2$ with extra As ambient, the result was the same as the Zn with As overpressure condition. In the case of impurity-induced disordering, Ga overpressure could not suppress the interdiffusion of In and Ga while As overpressure did retard the disordering process by slowing the diffusion front.

The diffusion coefficient of Zn is function of $[Zn_i]$ the interstitial concentration and $[Zn_s]$ the substitutional concentration.[25] In the As overpressure condition, the Ga vacancy concentration increases. Most of the interstitial Zn atoms will fall into the Ga vacancies and become substitutional Zn impurities. With the Zn_i interstitial concentration reduced then, the diffusion process will be dominated by substitutional diffusion. With respect to the Ga overpressure, the situation is totally reversed. The extra Ga reduces the As vapor pressure and the Ga vacancy concentration also decreases. Therefore the Zn_i concentration will be maintained and the diffusion process proceeds faster. For these two reasons the speed of the Zn diffusion front is controlled by the Ga vacancy concentration. This explains why the SQW did not intermix under the Zn and As overpressure condition but is subject to easy compositional disordering in an Ga overpressure environment. These results confirm the interstitial substitutional mechanism of interdiffusion and in the case of Zn impurity induced disordering neither Ga or As overpressure is effective in substantially slowing the intermixing (unless the Zn diffusion front is prevented from reducing the QW).

Fig. 9 — Low temperature (77K) photoluminescence spectra for GaAs-$In_{0.15}Ga_{0.85}As$ MQW (L_z = 50, 85 and 200Å) following $ZnAs_2$ impurity diffusion with different overpressure environments at 600° C for 1 hr. The degree of disordering in a $ZnAs_2$ + Ga overpressure condition is larger than in a $ZnAs_2$ overpressure condition.

CONCLUSION

The interdiffusion coefficient and activation energies have been determined for the interdiffusion of In and Ga under the conditions of excess Ga, excess As or no excess overpressure. These results were obtained by measuring the shifts in the photoluminescence peaks and correlating the data with a solution to Schrödinger's equation with the potential determined by an error function composition profile of the In mole fraction. The interdiffusion coefficient of In and Ga is a function of In composition, annealing environments and layer structure. In the As overpressure case, the higher In concentration in the SQW exhibits a larger diffusion coefficient. On the contrary, high In composition InGaAs-GaAs is more stable under Ga overpressure annealing. Even the highest interdiffusion rate associated with Ga overpressure is still less than the diffusion rate associated with As pressure. Samples with a clad-
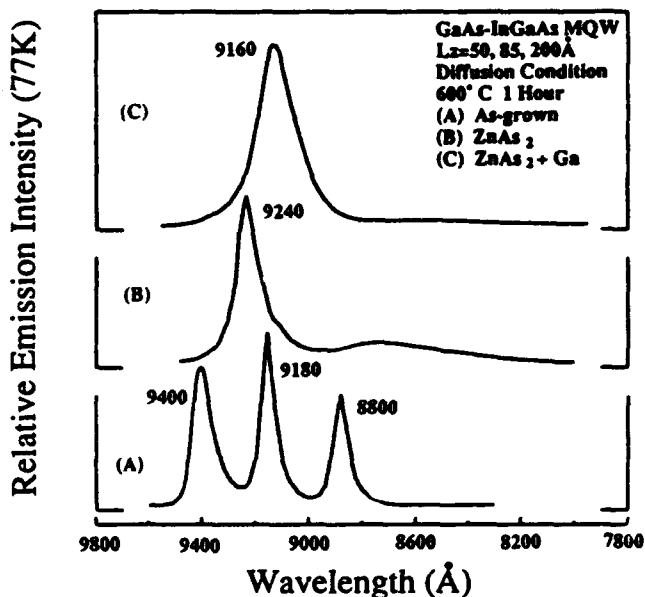
ding layer (AlGaAs) also show a higher interdiffusion coefficient of In and Ga. With respect to the impurity-induced disordering of InGaAs-GaAs by Zn (elemental or $ZnAs_2$ source). It was not possible to substantially slow the interdiffusion with a Ga or As overpressure (unless the overpressure condition prevented the Zn diffusion front from reaching the quantum well). It is encouraging that the pseudomosphic strained layer heterostructure can be preserved at high growth/processing temperature without requiring the deposition of encapsulants if the appropriate overpressure conditions are provided.

REFERENCES

1. J. W. Matthews, A. E. Blakeslee, J. Cryst. Growth. 27, 118 (1974); 29, 273 (1975); 32, 265 (1976).
2. J. W. Matthews, A. E. Blakeslee and S. Mader, Thin Solid Films 33, 253 (1976).
3. G. C. Osbourn, J. Appl. Phys. 53, 1586 (1982).
4. G. C. Osbourn, J. Vac. Sci. Technol. 21, 469 (1982).
5. L. L. Chang and A. Koma, Appl. Phys. Lett. 29, 138 (1976).
6. W. D. Laidig, N. Holonyak, Jr., M. D. Camras, K. Hess, J. J. Coleman, P. D. Dapkus and J. Bardeen, Appl. Phys. Lett. 38, 776 (1981).
7. W. D. Laidig and N. Holonyak, Jr., J. Electron. Mater. 11, 1 (1982).
8. D. G. Deppe, L. J. Guido and N. Holonyak, Jr., MRS meeting, Reno Nevada (1988).
9. K. Y. Hsieh, Y. C. Lo, J. H. Lee and R. M. Kolbas, 1988 Int. Symp. GaAs and Related Compounds, Atlanta, Georgia (Inst. Phys. Conf. Ser. NO. 96 p393).
10. M. D. Camras, N. Holonyak, Jr., K. Hess, M. J. Ludowise, W. T. Dietze and C. R. Lewis, Appl. Phys. Lett. 42, 185 (1983).
11. J. S. Major, Jr., L. J. Guido, K. C. Hsieh, N. Holonyak, Jr., W. Stutius, P. Gavrilovic and J. E. Willams, Appl. Phys. Lett. 54, 913 (1989).
12. K. J. Beernink, P. K. York, J. J. Coleman, R. G. Waters, J. Kim and C. M. Wayman, Appl. Phys. Lett. 55, 2167 (1989).
13. J. S. Major, Jr., L. J. Guido, N. Holonyak, Jr., K. C. Hsieh, E. J. Vesely, D. W. Nam, D. C. Hall, J. E. Baker, P. Gavrilovic, K. Meehan, W. Stutius and J. E. Williams, J. Electron. Mater. 19, 59 (1990).
14. J. S. Major, Jr., D. C. Hall, L. J. Guido, N. Holonyak, Jr., P. Gavrilovic, K. Meehan, J. E. Williams and W. Stutius, Appl. Phys. Lett. 55, 271 (1989).
15. D. F. Welch, W. Streifer, C. F. Schaus, S. Sun and P. L. Gourley, Appl. Phys. Lett. 56, 10 (1990).
16. J. S. Major, Jr., W. E. Plano, A. R. Sugg, D. C. Hall, N. Holonyak, Jr. and K. C. Hsieh, Appl. Phys. Lett. 56, 105 (1990).
17. W. Stutius, P. Gavrilovic, J. E. Williams, K. Meehan and J. H. Zarrabi, Electron. Lett. 24, 1493 (1988).
18. M. C. Joncour, M. N. Charasse and J. Burgeat, J. Appl. Phys. 58, 3373 (1985).
19. J. Crank, The Mathematics of Diffusion (Oxford University, London, 1957).
20. J. Cibert, P. M. Petroff, D. J. Werder, S. J. Pearton, A. C. Gossard, and J. H. English, Appl. Phys. Lett. 49, 223 (1986).
21. N. G. Anderson, Ph.D. dissertation. North Carolina State University (1988).
22. Y. Marzin, M. N. Charasse and B. Sermage, Phys. Rev. B31, 8298 (1985).
23. D. G. Deppe and N. Holonyak, Jr., J. Appl. Phys. 64, R93 (1988).
24. W. D. Laidig, J. W. Lee, P. K. Chiang, L. W. Simpson and S. M. Bedair, J. Appl. Phys. 54, 6382 (1983).
25. R. L. Longini, Solid St. Electron 5, 127 (1962).
26. K. K. Shih, J. W. Allen and G. L. Pearson, J. Phys. Chem. Solids 129, 379 (1968).

Diffusion of Zinc into GaAs Layers Grown by Molecular Beam Epitaxy at Low Substrate Temperatures

Y. K. SIN, Y. HWANG, T. ZHANG and R. M. KOLBAS

Department of Electrical and Computer Engineering
North Carolina State University, Raleigh, N.C. 27695-7911

We report the diffusion of zinc into low temperature (LT) GaAs grown by MBE at 200° C, the problems associated with using a silicon nitride film directly deposited on the LT GaAs as a Zn diffusion mask, and several schemes to avoid the problems. The Zn diffusion coefficient is measured (sealed-ampoule technique) to be about one order of magnitude higher in the LT GaAs than in normal GaAs, attributed to a large quantity of defects including arsenic antisites (As_{Ga}) in the LT GaAs. The effectiveness of silicon nitride as a Zn diffusion mask depends if the mask is deposited directly on the LT GaAs. The failure of the nitride directly deposited on the LT GaAs to stop the Zn is attributed to arsenic atoms outdiffusing from the As-rich LT GaAs (about 1 at. % excess As) into the nitride. Several structures are introduced including a 100-Å thick GaAs layer on the LT GaAs that are effective in preserving the diffusion mask properties of the silicon nitride.

Key words: Zn diffusion, LT GaAs, Si_3N_4, MBE

1. INTRODUCTION

In recent years, GaAs layers grown by molecular beam epitaxy (MBE) at low substrate temperatures (200° C, LT GaAs) have found an increasing number of applications both in electronics and optoelectronics. The LT GaAs layers have been employed as buffer layers for GaAs metal-semiconductor field-effect transistors (MESFET's).[1-3] GaAs MESFET's with a low temperature buffer layer (LTBL) exhibited reduced sidegating effects, increasing the packing density of transistors. Sidegating is the reduction in the drain-source current of a FET as a result of a bias applied to an adjacent device.[4,5] More recently, a substantial enhancement of the breakdown voltage of a GaAs MESFET has been demonstrated by using LT GaAs surface layers.[6] LT GaAs has also been used in optoelectronic devices such as photoconductors and a very high-speed photoconductive response was observed.[7-9]

Some remarkable features of the LT GaAs include (1) very weak photoluminescence (PL),[1,2] (2) very high resistivity,[1,2] (3) an As-rich stoichiometry ($GaAs_{1.01}$),[10] (4) a large quantity (greater than $10^{19}/cm^3$) of an EL2-like deep level (probably As_{Ga}),[10-12] and (5) a density of $10^{17} - 10^{18}/cm^3$ of arsenic precipitates.[13]

This paper reports the diffusion of zinc into LT GaAs grown by MBE at 200° C. We also investigate the use of a silicon nitride film directly deposited on the LT GaAs as a Zn diffusion mask and offer several schemes to avoid problems associated with using such a film.

2. EXPERIMENTAL METHODS

The samples used in this study were all grown by molecular beam epitaxy (MBE, Varian 360). The control sample (sample A) was an undoped liquid-encapsulated Czochralski (LEC) GaAs substrate. The LT GaAs samples were grown at 200° C and the growth rate was about 1 μm/hr. The growth temperature was measured accurately using a thermocouple imbedded in the heater block. After the LT GaAs was grown, a stop growth was employed to anneal the sample at 580° C for 10 min under As overpressure and then the next layers were grown successively. Four samples were grown as follows. Sample B – a 3-μm thick LT GaAs layer on an undoped GaAs substrate, sample C – a 1-μm thick GaAs layer on a 3-μm thick LT GaAs layer grown on a Si-doped GaAs substrate, sample D – an 87-Å GaAs quantum well sandwiched by 0.5-μm thick $Al_{0.3}Ga_{0.7}As$ layers on a 0.2-μm thick LT GaAs layer grown on an undoped GaAs substrate, and sample E – a 100-Å thick GaAs layer on a 2-μm thick LT GaAs layer grown on a Si-doped GaAs substrate.

The silicon nitride was deposited by plasma enhanced chemical vapor deposition (PECVD). The deposition temperature was fixed at 350° C for all of the samples throughout this experiment. The refractive index and thickness of the silicon nitride films were about 2.0 and 1500 Å, respectively. Standard photolithography was employed to define stripe patterns (windows for Zn diffusion, the width of the stripe was about 150 μm) and the silicon nitride films were etched by reactive ion etching (RIE) with a mixture of CF_4 and O_2. In addition, the LT GaAs layer was etched with deionized (DI) water-diluted clorox (clorox:DI water = 1 : 4) and the etching

rate was about 10 Å/sec at room temperature without agitation.

Zinc was diffused by a sealed-ampoule technique. ZnAs$_2$ was used as a Zn diffusion source, and a weight of about 5 mg of ZnAs$_2$ (to provide an As-overpressure of about 450 Torr, see Ref. 14) was used for an ampoule of about 4 cc. The amount of the source material was kept to about 1 mg/cc, so equal Zn diffusion rates were expected regardless of the size of the samples. Zn was diffused in a furnace at 650° C for 12 hr for all of the samples used in this study. After the Zn diffusion was performed, the sample was cleaved and stained with an A-B etchant,[15] and the Zn diffusion profile was observed with a Nomarski-contrast optical microscope.

In preparation for 77K PL (photoluminescence) measurements, small sections of the samples were pressed into a layer of indium on a copper plug[16] and cooled to 77K in a liquid nitrogen dewar. An argon laser beam ($\lambda = 5145$ Å) was focused on the sample surface, and the luminescence was measured using a 0.5-m spectrometer and a cooled S-1 photomultiplier.

3. RESULTS AND DISCUSSION

3.1 Zn Diffusion Coefficient in LT GaAs

The Zn diffusion profile for sample B is shown in Fig. 1. The left-hand side was etched for the ease of comparing Zn diffusion rates in undoped GaAs and LT GaAs. The two-boundary diffusion model with constant diffusion coefficient was used to calculate the Zn diffusion rates in the LT GaAs and undoped GaAs.[17,18] The Zn diffusion rate in the undoped GaAs could be evaluated in the region where the LT GaAs was completely etched. As shown in the schematic diagram of Fig. 1, the Zn diffused all the way through the 3-μm thick LT GaAs into the undoped GaAs substrate. The Zn diffusion rate in the LT GaAs layer ($D_{Zn} = 1.3 \times 10^{-11}$ cm^2/sec) was calculated to be about nine times faster than that in undoped GaAs ($D_{Zn} = 1.5 \times 10^{-12}$ cm^2/sec). The faster Zn diffusion rate in the LT GaAs is attributed to the presence of a large number of defects including arsenic antisites (As$_{Ga}$) in the GaAs layer grown at the low substrate temperature of 200° C. Zn has been shown to diffuse much faster in GaAs with a lot of defects than in GaAs with fewer defects because the defects provide high diffusivity paths or short circuit paths.[19] The dependence of Zn diffusion rate on the number of defects is also evidenced by the fact that a slower Zn diffusion rate was observed in an In-doped AlGaAs layer compared to AlGaAs,[20] attributed to a reduced defect density (fewer Ga vacancies, for example) made possible by isoelectronic In doping.[21] A similarly slow Be diffusion rate was observed from In-doped AlGaAs.[22]

3.2 Photoluminescence (PL)

The 77K PL data were taken for sample B before and after the Zn diffusion at 650° C for 12 hrs. The
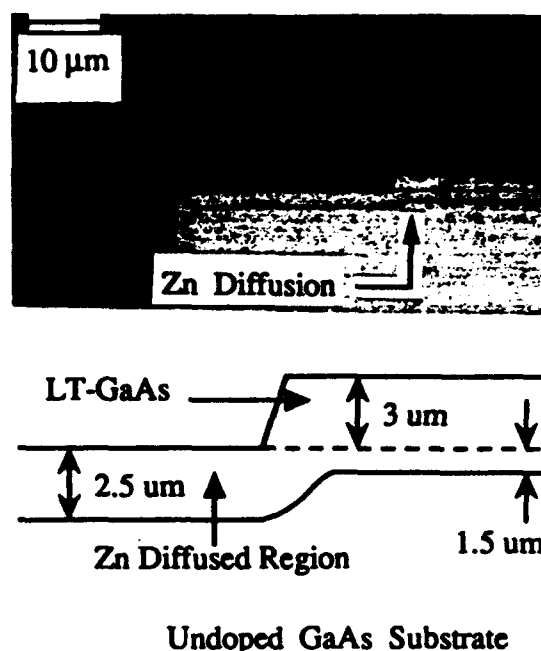

Fig. 1 — Optical photomicrograph of a cleaved and stained cross-section of a sample with a 3-μm thick LT GaAs layer on an undoped GaAs substrate (sample B) after Zn diffusion. On the left-hand side of the sample, the LT GaAs was etched for the purpose of estimating the Zn diffusion coefficient in the LT GaAs. Schematic cross-section is also shown with thicknesses of the layers labeled.

PL peaks were measured at 8500Å (1.462 eV) for both cases. The full widths at half maximum (FWHM's) for the as-grown and Zn-diffused LT GaAs layers were measured to be 307 and 211 meV, respectively. A high input power of 250 mW from the argon ion laser was focused on the surface of the sample to obtain reasonable data, which may account for why we could observe PL and others could not. The PL intensity was about twice as strong from the Zn-diffused sample. For LT GaAs layers grown at 300–450° C, the near band gap PL peak has been measured at approximately 1.5 eV at 5 K.[1] The difference of about 160Å in the wavelength in the PL peaks between two measurements can be explained by more defects in the layers grown at a lower growth temperature of 200° C.

High temperature annealing experiments were also performed on the other LT GaAs samples grown at different times. Annealing was done by the same sealed-ampoule technique under no-, As-, and Ga-overpressure conditions at 850° C for 0 hr. These annealing conditions seem to remove the optical defects responsible for the very weak PL intensity from the as-grown LT GaAs. The 77 K PL peak was observed at 8500Å after an anneal under no overpressure, whereas the 77 K PL peaks were measured at 8280Å after an anneal under As or Ga overpressure. The wavelength of 8280Å corresponds to a slightly p-doped GaAs.

3.3 Electrical Resistivity

Electrical resistivities of the LT GaAs were measured before and after the Zn diffusion of sample B with a four point probe. A reduction in resistivity was observed after the Zn diffusion. Prior to the diffusion the resistivity was too high to accurately measure, but after the Zn diffusion the LT GaAs had a resistivity of 2×10^{-3} Ω-cm that corresponded to a hole mobility of 31 cm^2/V-sec assuming a Zn concentration of 10^{20} cm^{-3} (see Ref. 23). Another group reported no reduction in resistivity from LT GaAs doped with Si (greater than 10^{18}/cm^3) after annealing at 600° C.[24]

3.4 Silicon Nitride as a Zn Diffusion Mask

Cleaved and stained cross-sections of samples A and B after the Zn diffusion are shown in Fig. 2. The samples shown in Fig. 2(b) and (c) underwent the plasma nitride deposition and Zn diffusion at the same time for a fair comparison. As shown in Fig. 2(c), the nitride film on the undoped GaAs substrate was a good Zn diffusion mask. However, as can be seen from Fig. 2(a) and (b), the nitride on the LT GaAs was unable to stop the Zn, and this
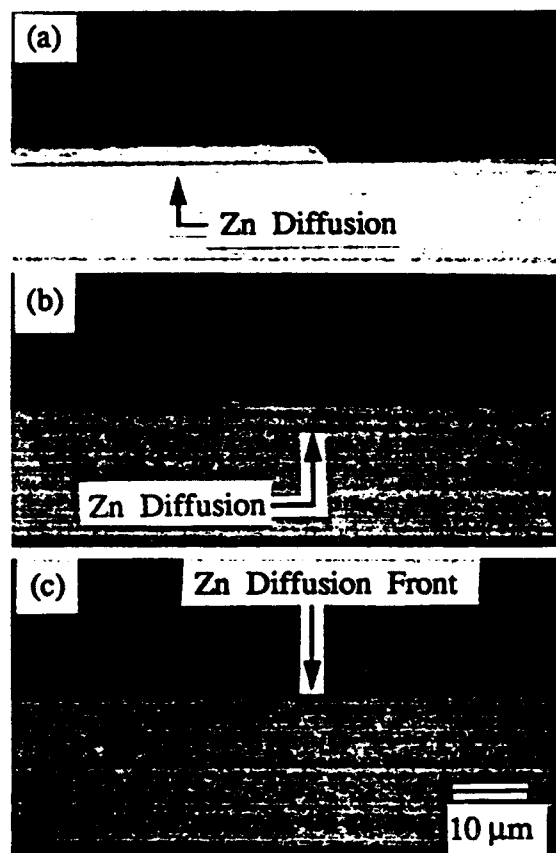
Fig. 2 — Optical photomicrographs of cleaved and stained cross-sections of samples A and B. Sample A is a control sample, an undoped GaAs substrate (Fig. 2(c)). Figure 2(a) and (b) are from sample B with the 3-μm thick LT GaAs layer. Two separate processing runs were performed for (a), and (b) and (c), respectively. The nitride on the LT GaAs was unable to stop the Zn (Fig. 2(a) and (b)), whereas the nitride on undoped GaAs substrate could stop the Zn.

result was observed several times on different wafers with different silicon nitride depositions. A schematic diagram of the Zn diffusion profile for sample B is shown in Fig. 3. The failure of the nitride film on the LT GaAs to stop the Zn is attributed to arsenic atoms outdiffusing from the As-rich LT GaAs (GaAs$_{1.01}$ or about 1 at. % excess arsenic) into the nitride. The outward diffusion of arsenic atoms from the underlying GaAs into the nitride has previously been reported as one of the reasons for the failure of nitride as an encapsulant on stoichiometric GaAs.[25] Adding impurities to dielectrics has profound effects on their diffusion mask characteristics as evidenced by one group's findings that the amount of Zn lateral diffusion could be changed by adjusting the amount of P$_2$O$_5$ added to the silicon oxide film.[26] They found that the lateral diffusion of Zn was typically an order of magnitude larger than the junction depth for all oxide compositions, but showed a marked reduction for oxides with 17-20% P$_2$O$_5$ by weight.

Several methods were tried to find ways to avoid the above problem. Cleaved and stained cross-sections of samples C and D after the Zn diffusion are shown in Fig. 4(a) and (b). As shown in Fig. 4(a), the 1-μm thick GaAs layer deposited on the LT GaAs was effective in preserving the diffusion mask properties of the silicon nitride. Likewise the 1-μm thick AlGaAs layer was also very effective as shown in Fig. 4(b). Schematic diagrams of the Zn diffusion profiles for samples C and D are shown in Fig. 5. A structure with a 100-Å thick GaAs layer on the 2-μm thick LT-GaAs layer (sample E) was also studied (data not shown here). Like samples C and D, the 100-Å layer of GaAs in sample E was also effective in preserving the diffusion mask properties of the silicon nitride. A portion of sample E was etched with a solution of H$_2$SO$_4$:H$_2$O$_2$:H$_2$O = 8:1:100 for 30 sec to remove approximately 250-500 Å from its surface.[27] The samples with and without the top 100-Å thick GaAs layer underwent processing at the same time, and the two samples were compared. The nitride on the sample with the 100-Å thick GaAs layer was effective in stopping the Zn, whereas the
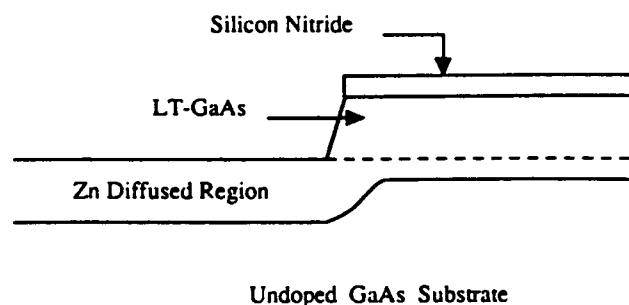
Fig. 3 — Schematic cross-section of the Zn diffused sample with the 3-μm thick LT GaAs layer (Fig. 2(a) and (b)). The diagram illustrates that the nitride on the LT GaAs could not stop the Zn.
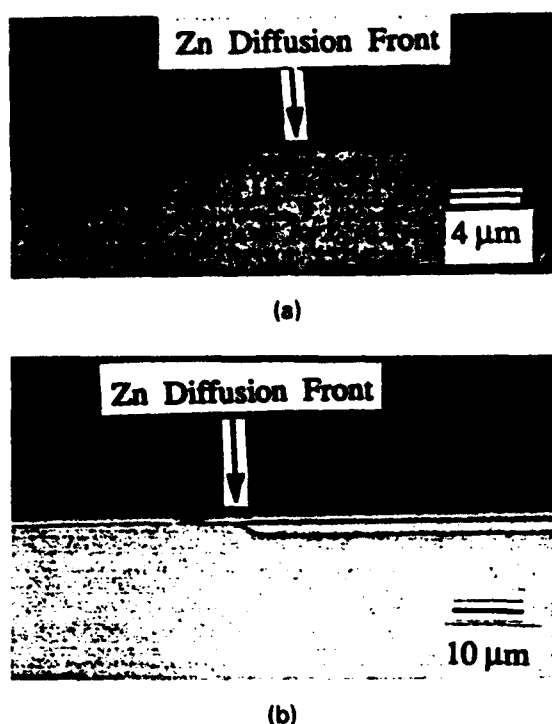
(a)

(b)

Fig. 4 — Optical photomicrograph of cleaved and stained cross-sections of samples C and D. With 1 μm of GaAs on top of 3 μm of LT GaAs (Fig. 4(a), sample C), or an AlGaAs/GaAs hetero-structure on top of 0.2 μm of LT GaAs (Fig. 4(b), sample D). The nitride acts as a good diffusion mask.
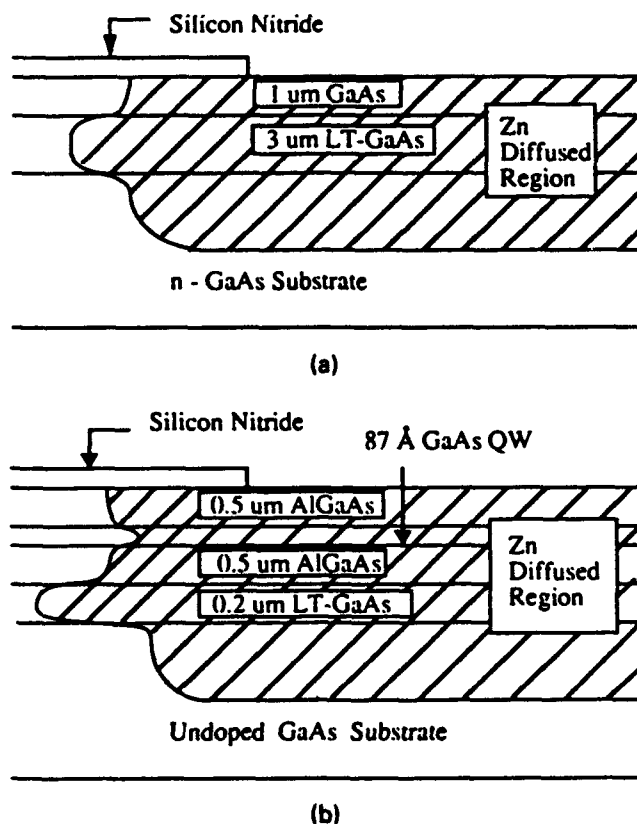

(a)

(b)

Fig. 5 — Schematic cross-sections of the Zn-diffused samples shown in Fig. 4. Figure 5(a) corresponds to sample C (1 μm of GaAs on top of 3 μm of LT GaAs) and Fig. 5(b) corresponds to sample D (an AlGaAs/GaAs heterostructure on top of 0.2 μm of LT GaAs).

nitride on the same wafer but without the 100-Å thick GaAs layer was unable to stop the Zn.

To see if 100 Å of GaAs can make such a big difference consider the self-diffusion coefficient (D) of As which is given by,[28]

$$D = D_0 \exp(-Q/kT)$$

where D_0 is a temperature independent factor and Q is the activation energy for the atomic jump mechanism. For As diffusion in GaAs, D_0 and Q are 0.7 cm^2/sec and 3.2 eV, respectively.[28] The self-diffusion coefficient of As in GaAs is estimated to be 3×10^{-18} cm^3/sec at 650° C from the above equation. Thus, the diffusion length of As in GaAs is about 40 Å after the Zn diffusion at 650° C for 12 hrs. It would appear that allowing the excess As to reach the silicon nitride film severely degrades its usefullness as a Zn diffusion mask.

3.5 Device Applications

Two facts suggest that LT GaAs will be very useful for semiconductor lasers since current confinement and heat dissipation are very critical for a low laser threshold, high modulation speed, and high power operation in these devices. First, a much higher electrical resistivity is obtained from LT-GaAs compared to undoped GaAs.[1] And, secondly, better thermal conductivity[29] and a better thermal expansion coefficient are expected from LT GaAs compared to dielectrics such as silicon nitride or silicon dioxide. Also, a better temperature dependence of laser threshold and lasing wavelength is expected due to a better thermal impedance. We are now in the process of developing laser diodes with the LT GaAs and the results will be published elsewhere.

4. SUMMARY

The Zn diffusion coefficient in LT GaAs has been measured using the two-boundary diffusion model and found to be about one order of magnitude higher than in undoped GaAs. The faster Zn diffusion is attributed to a large quantity of defects including arsenic antisities in the LT GaAs. The 77K photoluminescence data taken before and after Zn diffusion have the same emission peaks at 8500 Å but the diffusion reduces the halfwidth of the emission peak. Electrical resistivities measured before and after the Zn diffusion show a reduction in the resistivity. The failure of the silicon nitride film directly deposited on the LT GaAs to stop the Zn is attributed to arsenic atoms outdiffusing from the As-rich LT GaAs into the nitride film. Several structures were grown including samples with a 100-Å thick GaAs, a 1-μm thick GaAs, and about a 1-μm thick AlGaAs layer separating the LT GaAs from the silicon nitride. All of these layers grown on the LT GaAs were effective in preserving the diffusion mask characteristics of the silicon nitride. This success, with as little as 100 Å of GaAs, is consistent

with the assumption that As outdiffusion is responsible for the failure of the SiN mask.

REFERENCES

1. F. W. Smith, C. L. Chen, G. W. Turner, M. C. Finn, L. J. Mahoney, M. J. Manfra and A. R. Calawa, IEDM, (1988).
2. F. W. Smith, A. R. Calawa, C. L. Chen, M. J. Manfra and L. J. Mahoney, IEEE Electron Device Lett. *EDL-9*, 77 (1988).
3. M. R. Melloch, D. C. Miller and B. Das, Appl. Phys. Lett. *54*, 943 (1989).
4. H. Goronkin, M. S. Birrittella, W. C. Seelbach and R. L. Vaitkus, IEEE Trans. Electron. Devices *ED-29*, 845 (1982).
5. C. Kocot, and C. A. Stolte, IEEE Trans. Electron. Devices *ED-29*, 1059 (1982).
6. L. Yin, Y. Hwang, J. H. Lee, R. M. Kolbas, R. J. Trew and U. K. Mishra, IEEE Electron. Device. Lett. *EDL-11*, 561 (1990).
7. R. P. Marialla, J. D. Morse, R. Aines and C. E. Hunt, Mat. Res. Soc. Symp. Proc. *145*, 325 (1989).
8. A. C. Warren, J. M. Woodall, J. L. Freeouf, D. Grischkowsky, M. R. Melloch and N. Otsuka, Appl. Phys. Lett. *57*, 1331 (1990).
9. S. Gupta, P. K. Bhattacharya, J. Pamulapati and G. Mourou, Appl. Phys. Lett. *57*, 1543 (1990).
10. M. Kaminska, Z. Liliental-Weber, E. R. Weber, T. George, J. B. Kortright, F. W. Smith, B. Y. Tsaur and A. R. Calawa, Appl. Phys. Lett. *54*, 1881 (1989).
11. D. C. Look, D. C. Walters, M. O. Manasreh, J. R. Sizelove, C. E. Stutz and K. R. Evans, Phys. Rev. *B 42*, 3578 (1990).
12. H. Yamamoto, Z. Q. Fang and D. C. Look, Appl. Phys. Lett. *57*, 1537 (1990).
13. M. R. Melloch, N. Otsuka, J. M. Woodall, A. C. Warren and J. L. Freeouf, Appl. Phys. Lett. *57*, 1531 (1990).
14. A. Luque, J. Martin and G. L. Araujo, J. Electrochem. Soc. *123*, 249 (1976).
15. S. K. Ghandhi, VLSI Fabrication Principles, p. 523, Wiley, New York, (1983).
16. N. Holonyak, Jr. and D. R. Scifers, Rev. Sci. Instrum. *42*, 1885 (1971).
17. A. S. Grove, Physics and Technology of Semiconductor Devices, p. 75, Wiley, New York (1968).
18. H. J. Yoo and Y. S. Kwon, J. Electron. Mater. *17*, 337 (1988).
19. D. Shaw, Atomic Diffusion in Semiconductors, ed. D. Shaw, p. 46, Plenum, London (1973).
20. Y. K. Sin, K. Y. Hsieh, J. H. Lee and R. M. Kolbas, J. Appl. Phys. *69*, 1081 (1991).
21. K. H. Chang, C. P. Lee, J. S. Wu, D. G. Liu and D. C. Liou, Appl. Phys. Lett. *57*, 1640 (1990).
22. T. Tomioka, T. Fujii, H. Ishikawa, S. Sasa, A. Endoh, Y. Bamba, K. Ishii and Y. Kataoka, Jpn. J. Appl. Phys. *29*, L 716 (1990).
23. Y. Matsumoto, Jpn. J. Appl. Phys. *22*, 829 (1983).
24. W. Schaff, Workshop on low temperature GaAs buffer layers, San Francisco, CA, April 20, 1990.
25. A. Kiermasz, A. McQuarrie, and J. Bhardwaj, Semicond. Internat. Nov., 107 (1987).
26. B. J. Baliga and S. K. Ghandi, IEEE Trans. Electron. Devices *ED-21*, 410 (1974).
27. H. P. Meier, E. Van Gieson, W. Walter, C. Harder, P. Buchmann, D. Webb and A. Moser, Electron. Lett. *24*, 1123 (1988).
28. H. C. Casey, Jr., Atomic Diffusion in Semiconductors, ed. D. Shaw, p. 417, Plenum, London, (1973).
29. W. Nakwaski, J. Appl. Phys. *64*, 159 (1988).

Monolayer Thick GaSbAs-GaAs Strained Layer Quantum Well Lasers

J.H. Lee, T. Zhang, and R.M. Kolbas

Department of Electrical and Computer Engineering

North Carolina State University

Raleigh, North Carolina 27695-7911

Strained layer GaSbAs-GaAs quantum wells have the potential for longer emission wavelengths than InGaAs-GaAs quantum wells even though E_g(GaSb)>E_g(InAs) and the lattice mismatch is worse. Longer wavelength (lower energy) emission is possible because of the large valence band discontinuity. In this work we report the growth and operation of strained layer GaSbAs-GaAs quantum well lasers.

The energy bands for an AlGaAs-GaAs-GaSb type II heterostructure[1] are shown in Fig. 1. Note that electrons are confined in the GaAs confining layers (or in a shallow GaSbAs well) with relatively small bound state energies while the holes are confined in the GaSb (or GaSbAs) well. Recombination occurs as long as the electron and hole wave functions overlap which is possible even for a staggered real space transition.[2]

The epitaxial layers were deposited by molecular beam epitaxy (MBE) on 100-oriented GaAs substrates as follows: 1) a 5000Å $Al_{0.3}Ga_{0.7}As$ cladding layer (686 °C); 2) 500Å GaAs confining layers grown at 630, 600, or 550 °C. 3) a one monolayer thick GaSb quantum well at 630, 600, 550, or 450 °C, after a 10 minute interruption to decrease the background arsenic to below 10^{-7} Torr; 4) finally, a 5000Å $Al_{0.3}Ga_{0.7}As$ top

cladding layer (686 °C). Details are in reference 2.

Photoluminescence (77K) from samples grown at various substrate temperatures but the same flux ratio F_{Sb}/F_{Ga} (=3) are shown in Fig. 2. The two samples grown at the lowest temperatures exhibit broad and weak luminescence peaks from the quantum well and the GaAs confining layers due to the onset of three dimensional growth or the poor quality of the confining layers grown at too low a temperature. At higher growth temperatures, Fig. 2 (c) and (d), the peaks are much stronger and narrower but the quantum well emission peaks are shifted to higher energies with increasing growth temperature. The shift is due to the incorporation of As in the GaSb layer.

To investigate the source of the As incorporation additional samples were prepared with F_{Sb}/F_{Ga} = 3 or 10 at 600 °C. The photoluminescence from these samples were nearly identical indicating a weak dependence on the F_{Sb}/F_{Ga} ratio (up to 10).[2] Comparison of a number of different growth times and temperatures indicated that diffusion can only account for a small portion of the shift. The As incorporation appears to be due to the fact that GaSb grown at elevated temperatures is Ga-rich and the nonstoichiometric GaSb quantum well incorporates the excess As present when the top GaAs confining layer is deposited.

Spontaneous and stimulated emission (77K) spectra from a platelet[2] taken from a separate confinement single quantum well sample are shown in Fig. 3. At an excitation level of 4.1 kW/cm^2 (J_{eq}=1.7 kA/cm^2) laser modes are clearly evident

(Lee, Zhang, Kolbas)

from the quantum well. At high excitation levels the emission from the well dominates even as the GaAs confining layers begin to lase. Despite the As incorporation the resulting quantum well can support stimulated emission at longer wavelengths than InAs wells of comparable thickness.[2]

High quality monolayer thick strained layer GaAs-GaSbAs quantum well lasers can be prepared in an AlGaAs-GaAs separate confinement heterostructure. Laser thresholds are comparable to other monolayer thick lasers and the emission wavelengths are longer than those from comparable thickness InAs-GaAs quantum wells.

References

1. L.L. Chang, *Heterojunction and Semiconductor Superlattices,* p. 152, edited by G. Allen, G. Bastard, N. Boccara, M. Lannoo, and M. Voose (Springer-Verlag, N.Y., 1986).

2. J.H. Lee, "Carrier Collection and Laser Properties of Monolayer-Thick Quantum Well Heterostructures Grown by Molecular Beam Epitaxy," Ph.D. thesis, North Carolina State University (Aug. 1990).

(Lee, Zhang, Kolbas)

Figure Captions

Figure 1. Energy band diagram for a strained AlGaAs-GaAs-GaSb separate confinement heterostructure. The calculated band discontinuities for the GaAs-GaSb interface are ΔE_v=670meV and ΔE_c=-25meV which results in a type II heterojunction. Note that the quantized electron energy states will be much smaller than those in the InAs-GaAs system.

Figure 2. Photoluminescence spectra (77K) from samples (see Fig. 1) prepared at different growth temperatures. The peaks at 8220Å are from the GaAs confining layers. The shift in the quantum well emission wavelength is attributed to the incorporation of As in the GaSb quantum well.

Figure 3. Spontaneous and stimulated emission spectra (77K) from a one monolayer $GaSb_{1-y}As_y$-GaAs-$Al_{0.3}Ga_{0.7}As$ separate confinement heterostructure. Note that the threshold is quite low considering that the quantum well is much narrower than the scattering path length of an electron or hole. Also, note that the emission wavelength is longer than comparable thickness InAs-GaAs quantum wells.
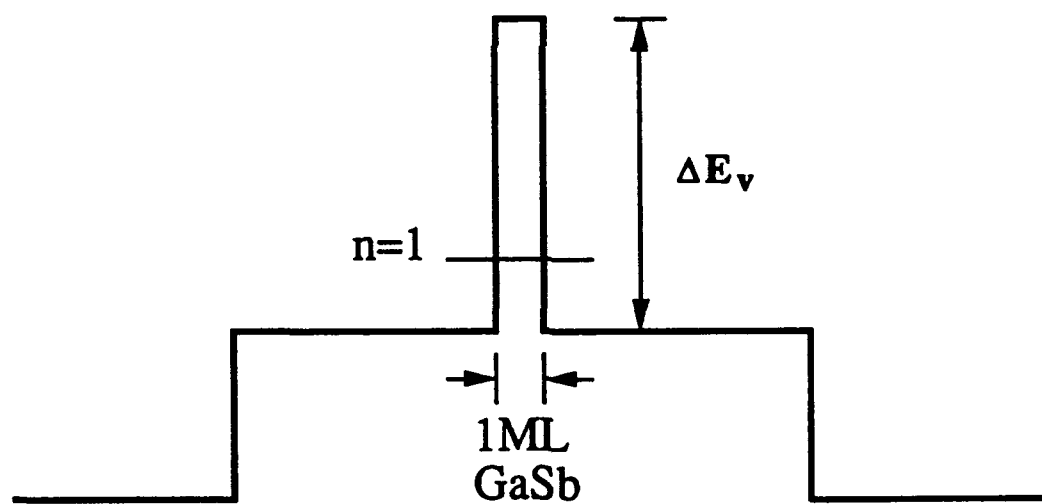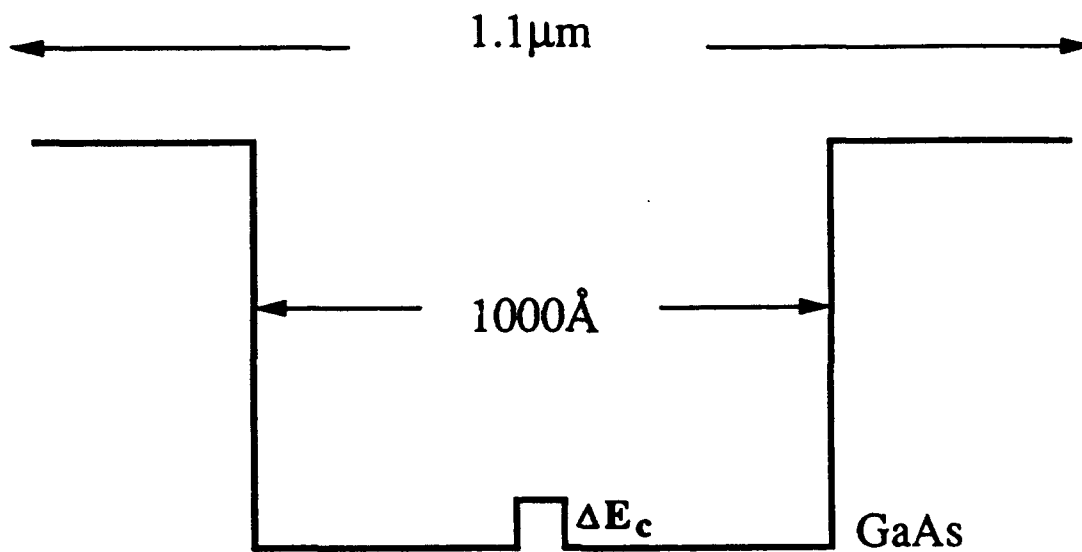
(Lee, Zhang, Kolbas)

$1.1 \mu m$

1000Å

ΔE_c

GaAs

ΔE_v

n=1

1ML
GaSb

686 °C

600 °C

686 °C

Growth
Temperature

GaAs-GaSb$_{1-y}$As$_y$ 1 ML SQW

$F_{Sb}/F_{Ga}=3$

(a) $T_{QW}=450$ °C, $T_{GaAs}=550$ °C

(b) $T_{QW}=550$ °C, $T_{GaAs}=550$ °C

(c) $T_{QW}=600$ °C, $T_{GaAs}=600$ °C

(d) $T_{QW}=630$ °C, $T_{GaAs}=630$ °C

77 K pulsed

(d)

(c)

(b)

(a)

Relative Emission Intensity

Wavelength (Å)
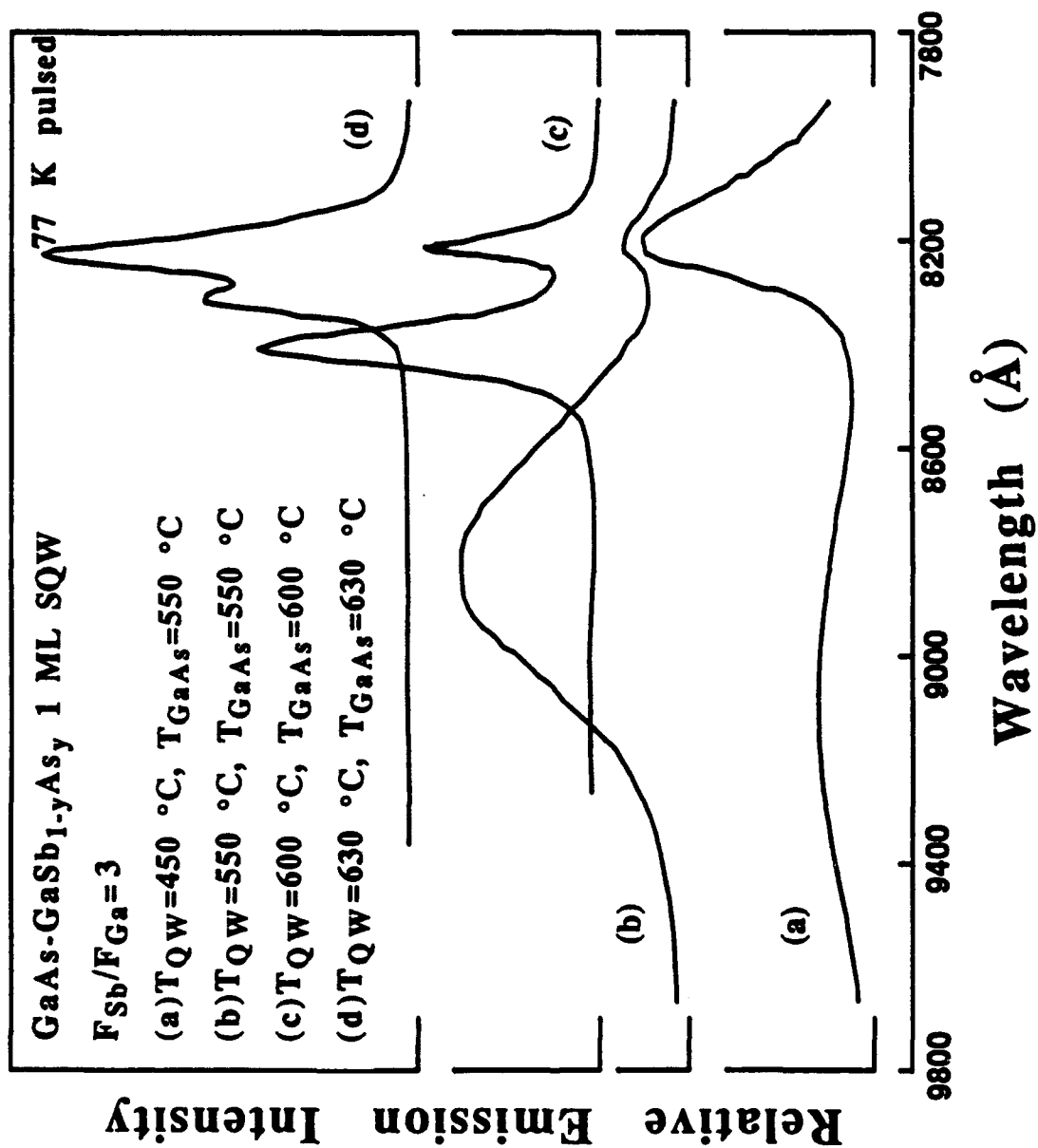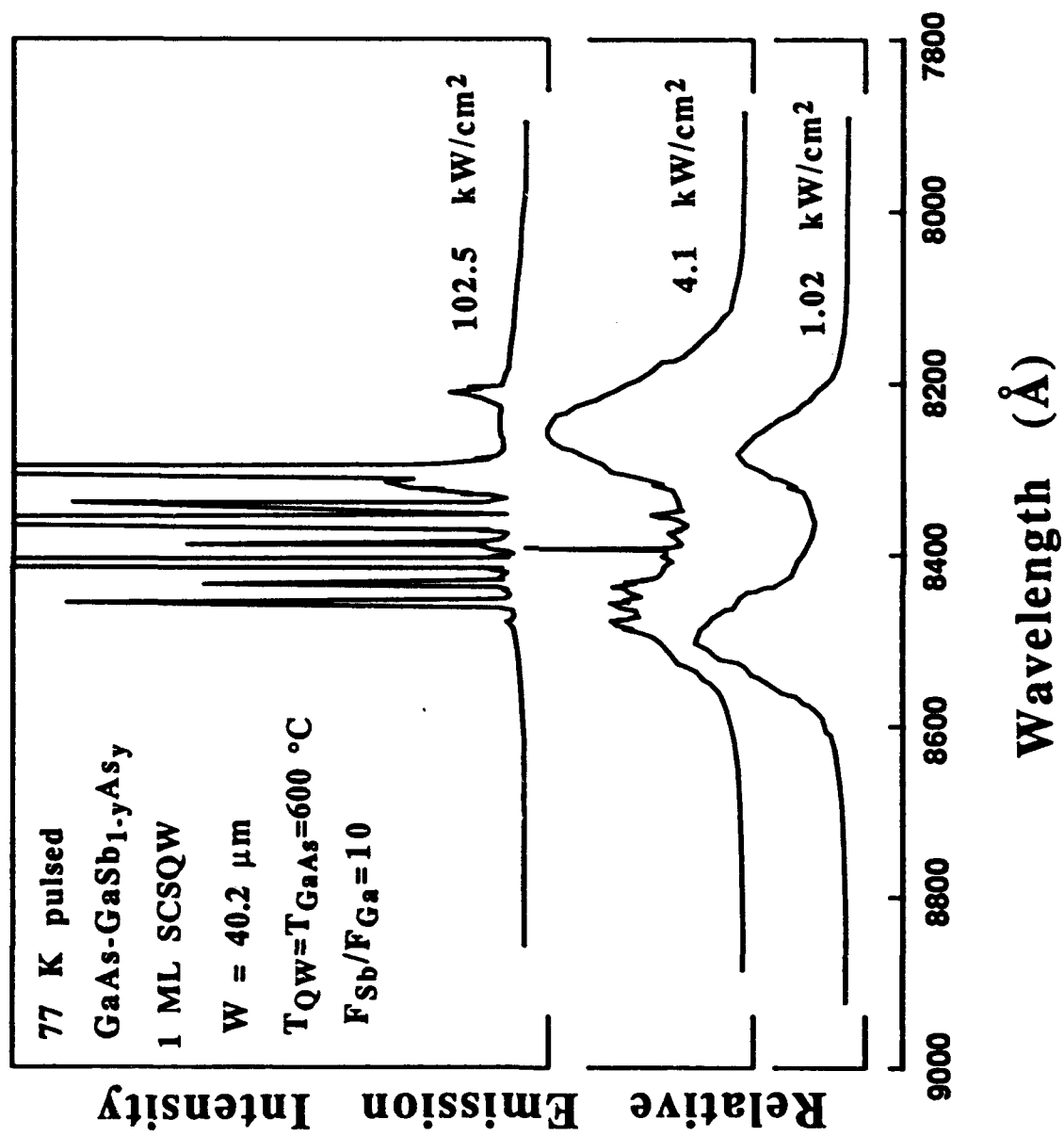
Improved Breakdown Voltage in GaAs MESFET's Utilizing Surface Layers of GaAs Grown at a Low Temperature by MBE

L.-W. YIN, Y. HWANG, J. H. LEE, ROBERT M. KOLBAS, MEMBER, IEEE, ROBERT J. TREW, SENIOR MEMBER, IEEE, AND UMESH K. MISHRA, MEMBER, IEEE

Abstract—A metal-semiconductor field-effect transistor utilizing surface layers of GaAs grown at a low temperature by MBE (LT GaAs) under the gate electrode has been fabricated. The high trap density of LT GaAs reduces the surface fields of the FET, suppresses gate leakage, and increases the gate-drain breakdown voltage without sacrificing current drive capability. An undoped AlAs layer is incorporated between the LT GaAs layer and the channel as a barrier to the diffusion of excess As from the LT GaAs layer to the channel. A 75-μm gate-width device demonstrated an improved breakdown voltage of 34.85 V with a g_m of 144 mS/mm and an I_{dss} of 248 mA/mm.

I. INTRODUCTION

THE major factor limiting the microwave power that can be obtained from GaAs MESFET's is the breakdown voltage between the gate and the drain [1]. The breakdown voltage can be enhanced by a combination of reducing the doping level in the channel and using recess schemes to alleviate the large electric field at the drain edge of the gate [2], [3]. This, however, reduces the available current from the device and hence does not substantially increase the output power. At first suggested by Barton and Ladbrooke [4] and subsequently formalized by Trew and Mishra [5], the electric field parallel to the device surface at the gate edge increases until charge is injected from the gate metal into adjacent surface states in the semiconductor. Trap-assisted conduction along the surface leads to leakage and subsequent breakdown. If the surface semiconductor is replaced by a material which a) has a substantially larger critical field for breakdown, b) has poor surface conductivity, and c) is preferably lattice matched, then the breakdown voltage of the FET should be increased substantially. An excellent candidate for this layer is GaAs grown at a low temperature by MBE (LT GaAs) [6], developed first by Calawa *et al.* at M.I.T. Lincoln Laboratories.

This LT GaAs layer is grown at ~ 200°C by MBE and is stabilized by an *in-situ* anneal at 580°C. The current understanding of the properties of this layer which are relevant to electronic devices are listed below [6]:

1) the LT GaAs grown as stated is a single crystal,
2) it is highly resistive,
3) it has a very high trap density ($N_T > 10^{21}$ cm^{-3}), and
4) the material has approximately 1% of excess arsenic as determined by Auger and TEM studies.

In this work, we report a substantial enhancement of the breakdown voltage of GaAs MESFET's without sacrificing the current drive capability of the device. This was achieved by placing a LT GaAs layer grown by MBE under the gate electrode and extending from the source to the drain of the FET. The LT GaAs has a very high trap density which suppresses gate leakage and alleviates the breakdown caused by the surface fields of the FET.

II. DEVICE STRUCTURE AND FABRICATION

To evaluate the increase in breakdown voltage that is achieved by the LT GaAs surface layers, MESFET's were fabricated on two wafers, one (sample A) with the surface layers and a control wafer (sample C) with no surface layers. Fig. 1 shows a schematic cross section of the MESFET fabricated on sample A. The epitaxial layers were grown by MBE on undoped LEC substrates. First, a 200-nm-thick undoped buffer layer was grown at 580°C followed by a 60-nm-thick active layer doped at 6×10^{17} cm^{-3} and an undoped spacer 20 nm thick. The surface layers consisted of a 20-nm-thick AlAs layer grown at 680°C and a 50-nm-thick LT GaAs layer grown at 200°C. The wafer was annealed at 580°C after growth to stabilize the LT GaAs layer. The doping of the channel was controlled to yield an electron sheet charge and mobility as determined by Hall measurement of 1.77×10^{12} cm^{-2} and 3406 cm$^2 \cdot$ V$^{-1} \cdot$ s^{-1}, respectively, for wafer C. Wafer A had a mobility μ of 2317 cm$^2 \cdot$ V^{-1}s^{-1} and a sheet charge density n_s of 3×10^{12} cm^{-2}. The AlAs was crucial in preventing undesired compensation of the underlying channel by the surface LT GaAs. There are at least two mechanisms that cause this instability. The first is that the excess arsenic and its related defects (e.g., Ga vacancies) within the LT GaAs can diffuse into the
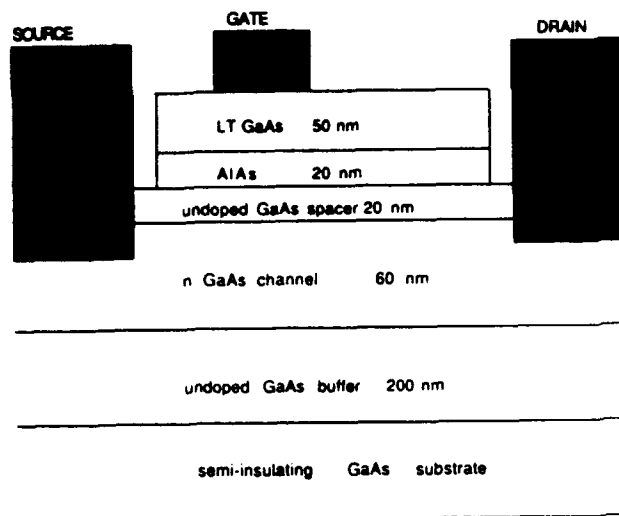
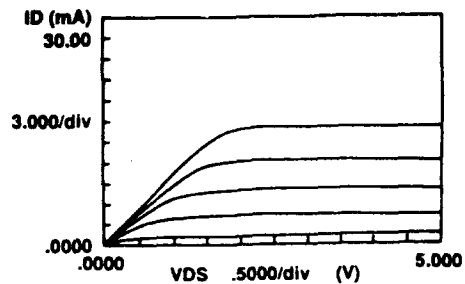Fig. 1.   Device structure with LT GaAs surface layer.

Fig. 2.   Current-voltage characteristics of a device from the control wafer C. The maximum gate voltage is +0.5 V with each gate voltage step being −0.5 V.
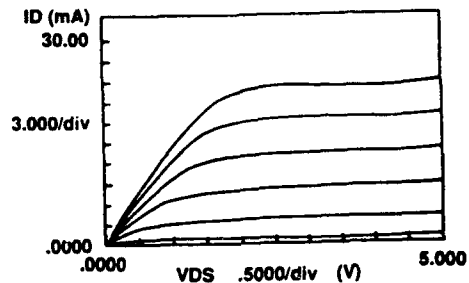

Fig. 3.   Current-voltage characteristics of a device with a LT GaAs surface layer (wafer A). The maximum gate voltage is +0.5 V with each gate voltage step being −0.5 V.
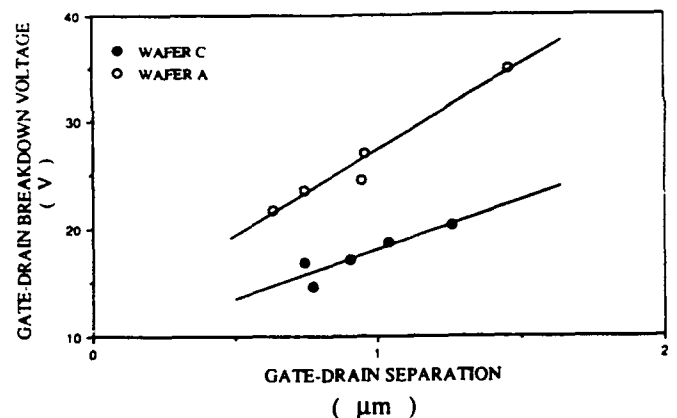

Fig. 4.   Relationship between the gate-drain breakdown voltage and the gate-drain separation for devices from wafers A and C.

channel and compensate doping via the formation of traps such as AsGa anti-sites. The second is that as the temperature is reduced to grow the LT GaAs on top of the GaAs, excess arsenic is adsorbed onto the GaAs surface due to the reduced vapor pressure of arsenic at the lower growth temperature. This uncompensated As is trapped by the overgrown LT GaAs and is forced into the channel by the *in-situ* anneal at 580°C required to stabilize the LT GaAs. Previous work [7] has shown that these problems are substantially corrected by utilizing the AlAs layer and that layers without the AlAs barrier were completely compensated.

Devices with nominal gate lengths of 1.25 μm were fabricated on both wafers using a conventional mesa isolation technique and AuGeNi-based alloyed ohmic contacts. The gate was fabricated by lifting off Ti-Au metal. There was no gate recess used in either case. The nominal gate-source and gate-drain spacings were 0.5 and 1.25 μm with the final values being determined by alignment tolerances. The only difference in the processing of the two wafers was that the surface layers of sample A were etched away prior to evaporating the ohmic contact metals to facilitate formation of ohmic contacts.

III. RESULTS AND DISCUSSION

The I-V characteristics of typical devices from wafers C and A are shown in Figs. 2 and 3, respectively. The maximum gate voltage is +0.5 V and each step of the applied gate voltage is −0.5 V. The device from control wafer C had an I_{dss} of 160 mA/mm and a nominal transconductance g_m of 144 mS/mm. The gate-drain breakdown voltage, measured at a gate current of 1 mA/mm, was 21.32 V. In contrast, the device with the LT GaAs capping layers had a large I_{dss} of 248 mA/mm with a comparable g_m of 144 mS/mm. In addition, the gate-drain breakdown voltage was increased substantially to 34.85 V. This enhancement in breakdown voltage is caused by the surface layers of AlAs and LT GaAs. Past work [8], [9] has shown that utilizing a wide-bandgap material under the gate (typically a 60-nm-thick layer of $Al_{0.4}Ga_{0.6}As$) has enhanced the breakdown voltage of the MESFET by approximately 5 V for comparable struc-

tures. We, therefore, attribute the substantial increase in breakdown voltage primarily to the LT GaAs layer.

Fig. 4 shows the relation between the gate-drain breakdown voltage and the gate-drain separation for devices from wafers A and C. The g_m for devices from wafers A and C range from a minimum of 120 and 128 mS/mm, respectively, to a maximum of 144 mS/mm. For devices from control wafer C, I_{dss} ranges from 192 to 200 mA/mm, whereas the I_{dss} of devices from wafer A ranged from 240 to 260 mA/mm. It can be seen that the devices with the LT GaAs surface layer have a substantially larger gate-drain breakdown voltage without sacrificing current drive.

IV. CONCLUSION

A substantial enhancement of the breakdown voltage of GaAs MESFET's has been achieved without sacrificing the

current drive capability of the device. This was due to the utilization of surface layers of AlAs and LT GaAs extending from the source to the drain and under the gate of the MESFET. The large breakdown voltage achieved with the small gate–drain spacing is very important for self-aligned technologies and may stimulate a major advance in the power handling capability of MESFET's.

REFERENCES

[1] W. R. Frensley, "Power-limiting breakdown effects in GaAs MES-FET's," *IEEE Trans. Electron. Devices*, vol. ED-28, p. 962, 1981.

[2] S. H. Wemple, W. C. Niehaus, H. M. Cox, J. V. DiLorenzo, and W. O. Schlosser,"Control of gate-drain avalanche in GaAs MESFETs," *IEEE Trans. Electron Devices*, vol. ED-27, no. 6, 1980.

[3] Y. Wada and M. Tomizawa, "Drain avalanche breakdown in gallium arsenide MESFET's," *IEEE Trans. Electron Devices*, vol. 35, no. 11, pp. 1765-1770, 1988.

[4] T. M. Barton and P. H. Ladbrooke, "The role of the device surface in the high voltage behavior of GaAs MESFETs," *Solid State Electron.*, vol. 29, no. 8, p. 807, 1986.

[5] R. J. Trew and U. K. Mishra, presented in part at the Device Res. Conf., Univ. of Calif., Santa Barbara, June 25-27, 1990.

[6] F. W. Smith, A. R. Calawa, C.-L. Chen, M. J. Manfra, and L. J. Mahoney, "New MBE buffer used to eliminate backgating in GaAs MESFET's," *IEEE Electron Device Lett.*, vol. 9, no. 2, pp. 77-80, 1988.

[7] Y. Hwang *et al.*, "The elimination of channel depletion caused by surface low temperature GaAs in GaAs MESFET structure," presented at the EMC, Univ. of Calif., Santa Barbara, June 27-29, 1990.

[8] M. Zaitlin, "Reverse breakdown in GaAs MESFET's," *IEEE Trans. Electron Devices*, vol. ED-33, no. 11, p. 1635, 1986.

[9] B. Kim *et al.*, "Millimeter-wave power operation of an AlGaAs/In-GaAs/GaAs quantum well MISFET," *IEEE Trans. Electron Devices*, vol. 36, no. 10, pp. 2236-2242, 1989.

Optoelectronic Properties of GaN, AlGaN and AlGaN-GaN Quantum Well Heterostructures

R. M. Kolbas and S. Krishnankutty
North Carolina State University, Raleigh, NC
27695-7911

The dramatic advances in wide bandgap semiconductors since the mid 1980s have been driven by new developments in growth processes, new requirements for high power and high temperature operation and radiation hardness, and the desire for blue and ultraviolet optoelectronic devices. $Al_xGa_{1-x}N$ has a direct bandgap (3.4-6.2 eV), a large and sharp optical absorption edge, a large radiative recombination coefficient, and is quite hard and stable in chemical environments and at elevated temperatures. Challenges in the continued development of the AlGaN material system are the lack of a native substrate, high n-type carrier concentrations in epitaxial films and controlled p-doping. In this paper we describe the optical properties that have been achieved with MOCVD grown AlGaN on sapphire substrates and the diffusion of zinc into these GaN epitaxial layers.

For GaN samples with carrier concentrations less than $1x10^{18}/cm^3$ a low intensity peak approximately 70 meV down from the main peak (attributed to a TO phonon replica) can be observed as shown in Fig. 1. For GaN samples with a background doping less than $1x10^{17}/cm^3$ features identified as excitonic in nature (A and C in Fig. 1) by Gershenzon and co-workers can be observed at 77K. Typical linewidths are 25 meV at 77K for $Al_xGa_{1-x}N$ (x<0.15).

The photoluminescence spectra from $Al_xGa_{1-x}N$-GaN-$Al_xGa_{1-x}N$ quantum wells of different thicknesses and x values are shown in Fig. 2. Note that the emission from the quantum wells is shifted to higher energies characteristic of a type I heterojunction. However the shifts are more than the calculated quantum effects by an amount (40 meV at x=0.13) that is linearly dependent on the alloy composition. The added shift can be accounted for by including strain induced bandgap shifts for the hexagonally symmetric AlGaN-GaN crystal. Also note that the thicknesses and compositions of these samples are below the Matthews and Blakeslee critical thickness.

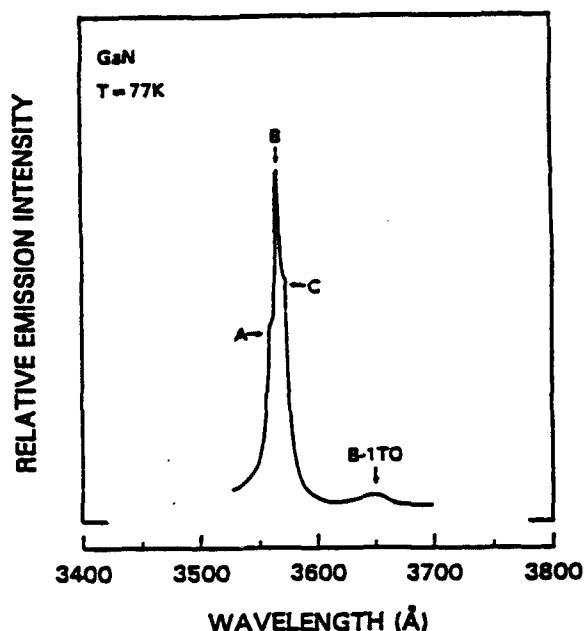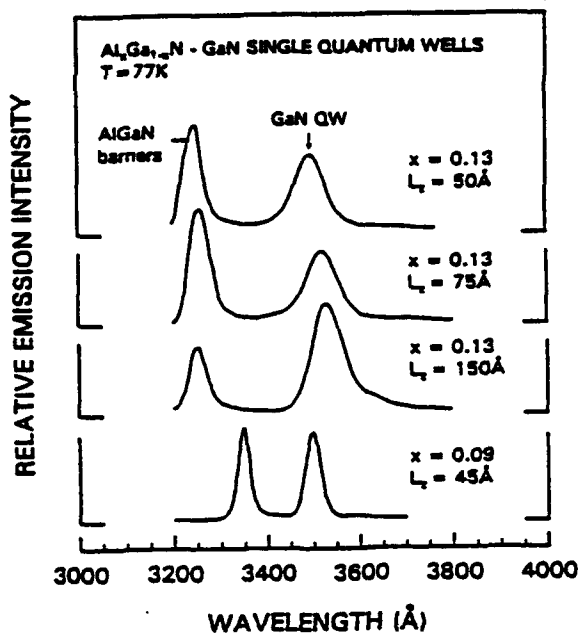During the 1976-1981 time frame researchers tried to diffuse a number of elements into GaN (Mg, Cd, Zn, Li, Be, Si, Ge, and S) to obtain p-type doping but were successful only with Li. Subsequently the post-growth doping of GaN focused on ion implantation. Most recently we have successfully diffused Zn into epitaxial layers of GaN with as grown n-type carrier concentrations of approximately

Figure 1

Figure 2

$5 \times 10^{17}/cm^3$. The successful diffusions were measured by photoluminescence and secondary ion mass spectroscopy. The photoluminescence spectra of GaN before diffusion (a), and after diffusion for various times at 925°C are shown in Fig. 3. The emission peaks are: 1- near band edge transition, 2- TO phonon replica of main peak, 3- a 3775Å peak attributed to a transition from the conduction band to a substitional zinc level, and 4- a 4250Å peak attributed to a transition from the conduction band to a level introduced by a complex associated with substitional zinc impurities.
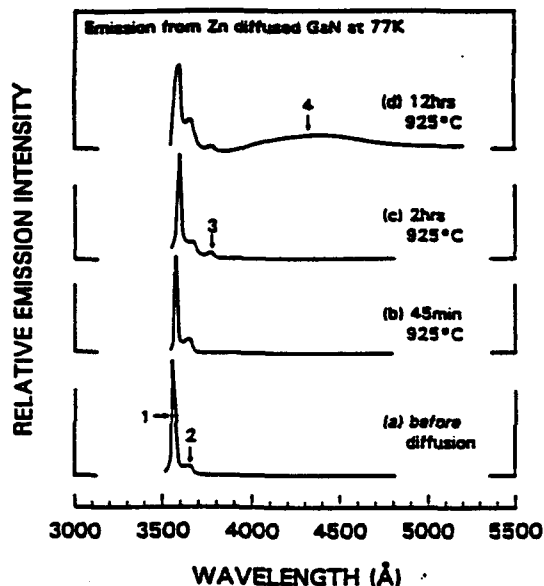
Figure 3

The photoluminescence spectra of GaN after 12 hour Zn diffusions at various temperatures are shown in Fig. 4 where the same peak assignments are applicable. The peak at 3775Å (labeled 3) is 220 meV below the band edge which corresponds closely to the calculated hydrogenic acceptor level in GaN. At higher temperatures or longer diffusion times the Zn concentration increases and the broad peak, labeled 4, appears. The SIMS depth profiles for these samples are shown in Fig. 5. The Zn concentration is based on an ion implanted GaN:Zn calibration sample. The diffusion appears to be an interstitial-substitional process where the interstitial Zn acts as a donor and the substitional Zn acts as an acceptor. The interstitial diffusion coefficient and activation energy were calculated to be 5.7×10^3 cm²/s and 3.8 eV, respectively. The presentation will include details of the diffusion and SIMS

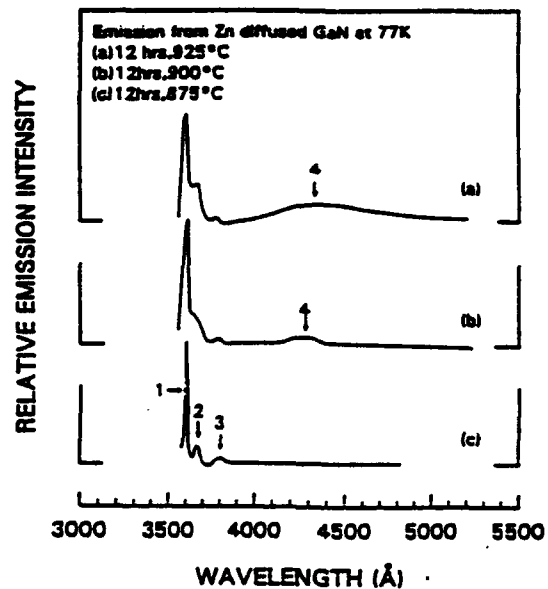data and a brief discussion of the movement of hydrogen in the film during diffusion.
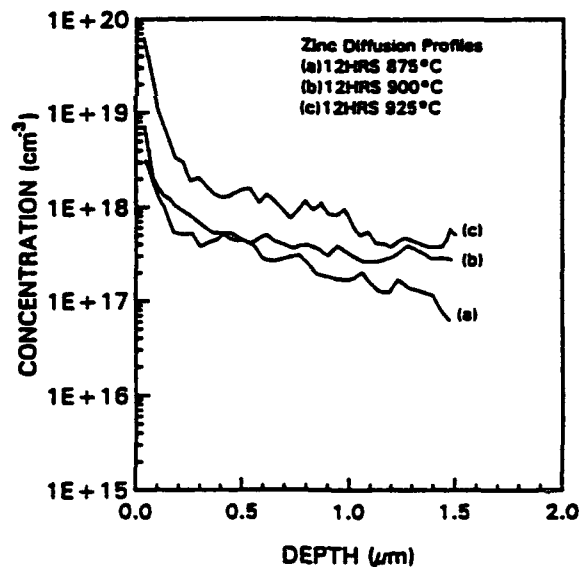

Figure 4

Figure 5

In summary, significant progress is being made to meet the challenges of understanding and controlling the AlGaN material system for optoelectronic devices.

Dose effects in Si FIB-mixing of short period AlGaAs/GaAs superlattices

A.J. Steckl, P. Chen, A. Choo, H. Jackson and J.T. Boyd
University of Cincinnati, Cincinnati, OH

P.P. Pronko and A. Ezis
Universal Energy Systems, Dayton, OH

R. M. Kolbas
North Carolina State University, Raleigh, NC

Abstract

Results are presented on FIB mixing of an $Al_{0.3}Ga_{0.7}As/GaAs$ superlattice with equal 3.5 nm barrier and well widths. Si^{++} was accelerated to 100 kV and implanted parallel to sample normal at doses ranging from 10^{13} to $10^{15}/cm^2$. The level of inter-layer disordering was measured primarily by Auger depth profiling. The mixing effect of RTA-only increased roughly linearly with annealing time at both 950 and 1000°C, with the latter exhibiting a sharper slope. At either temperature, 90 s was sufficient to produce complete mixing within the accuracy of the measurement. An anneal of 10 s at 950°C which was utilized in subsequent post-implantation annealing, resulted in ~ 25% thermally-induced mixing, with a corresponding PL "blue shift" of 6 meV. The level of mixing by an ion dose of $1 \times 10^{14}/cm^2$ yielded a mixing parameter of 0.87, where 1.0 represents complete mixing. This is the lowest ion beam dose necessary for nearly complete mixing reported to date for either FIB or BB implantation. Doubling the dose to $2 \times 10^{14}/cm^2$ results in an increase in mixing by only 0.05 to 0.92. Larger doses produced a diminishing increase in mixing parameter.

Introduction

The introduction of certain species into $Al_{1-x}Ga_xAs/Al_{1-y}Ga_yAs$ superlattice structures by doping or ion implantantion is known [1-3] to result, upon subsequent anneal, in compositional mixing of the superlattice. Focused ion beam (FIB) implantation has been used to locally mix superlattice structures, in order to provide regions with a different band-gap energy and index of refraction. In conjunction with rapid thermal annealing (RTA) , FIB implantation can provide highly localized mixing with a maskless and resistless process. This technique finds applications in the fabrication of optical gratings for semiconductor DBR or DFB lasers, channel waveguides, quantum wires, etc.

Previous results [4,5] on FIB mixing of superlattices used structures with superlattice periods of 50 - 60 nm. In this paper, we present results on FIB mixing of a short-period $Al_{0.3}Ga_{0.7}As/GaAs$ superlattice with equal 3.5 nm barrier and well widths.

Experimental Procedure

The superlattice samples used in this study were grown by molecular beam epitaxy . The substrate was a (100) GaAs, a GaAs buffer layer was grown first, followed by a 1μm $Al_{0.3}Ga_{0.7}As$ cladding layer, a single 30nm GaAs quantum well, a superlattice stack of 29 periods consisting of 3.5 nm GaAs wells and 3.5 nm $Al_{0.3}Ga_{0.7}As$ barriers , and a 50nm $Al_{0.3}Ga_{0.7}As$ cap.

The RTA of the superlattice samples was performed with proximity protection. A graphite pill box was used for preventing As evaporation during high temperature annealing. Inside the pill box, the superlattice samples were sandwiched between two GaAs wafers. The chamber was first pumped down to 8×10^{-3} Torr, followed by RTA at atmospheric pressure in forming gas (96% N_2/ 4% H_2) with a flow rate of about 1 lpm. Experiments to determine optimal annealing conditions were carried out at temperatures of 950 and 1000°C, and annealing times of 10, 30 and 90s.

Photoluminescence characterization was performed at 4.2 and 77°K using an Ar ion laser. Auger electron spectroscopy was employed to measure the atomic composition as a function of depth for the as-grown and processed structures. FIB implantation was performed with a MicroBeam Inc. NanoFab150. Si^{++} ions were accelerated to 100kV and implanted parallel to sample normal at doses ranging from 10^{13} to 3×10^{15} cm^{-2}. The Si^{++} focused ion beam had a current of 25pA and a beam diameter of ~100nm.

Results and Discussion

AES depth profiles of the as-grown superlattice, as well as after RTA-only and after implantation and RTA are shown in Fig.1. The 68eV Al peak was monitor to Al atomic percentage in the various layers of the sample. The profile of the as-grown superlattice (Fig.1a) clearly shows the AlGaAs cap, the superlattice stack, the quantum well, and the AlGaAs cladding layer. RTA for 10 sec at 950°C for 10s results in a very similar depth profile (see Fig. 1b), with only minor mixing of the mixing. The same conclusion applies for samples which underwent RTA-only at 950°C for 30s, and at 1000°C for 10s. However, in samples which have experienced stronger RTA conditions, namely 950°C 10s (shown in Fig.1c), as well as 1000°C for 30s and 90s, the periodic superlattice structure was essentially absent, indicating complete thermal mixing. The AES depth profile measured from a sample FIB-implanted with a Si^{++} dose of 1×10^{14} cm^{-2} and annealed at 950°C for 10s is shown in Fig.1d. By comparing the RTA-only profile of Fig. 1b with the FIB plus RTA profile of Fig. 1d, one can deduce the strong effect of the FIB implantation at this dose.

Low temperature photoluminescence, which is normally used to provide an indication of the structural quality of the material, can also provide evidence of mixing. In Fig. 2a photoluminescence at 4.2°K is shown for an RTA-only sample (950°C, 10s). Two sharp PL peaks are observed, corresponding to emission from the superlattice (1.675eV) and from the GaAs quantum well (1.52eV). After FIB implantation, no emission could be observed since the crystal structure was heavily disordered by ion-crystal collisions.

After RTA, a "blue shift" peak, shown in Fig.2b, was observed at 1.718eV. This new peak represents the AlGaAs bulk material (mixed superlattice) with ~16% Al atomic percentage, which is quite close to the expected average value (15%) of the superlattice. A much reduced signal from regions of the superlattice which remain unmixed is also observed. Similar PL profiles were also obtained from the samples implanted with higher doses, such as 2×10^{14} or 1×10^{15} cm^{-2}. However, the intensity of new peaks from these higher-dose samples were relatively lower, indicating that heavier damage was created in these samples and that it was not completely annealed out during RTA.

A quantitative analysis of the AES depth profiles was performed in order to evaluate the degree of mixing for variety of FIB/RTA processing conditions. The standard deviation of the Al atomic percentage over the superlattice depth is used as the measure of level of mixing. Since the Al deviation is in proportion to the peak-to-valley value of the superlattice, it therefore, reflects the degree of mixing by comparison to the as-grown sample. The calculated standard deviations for various samples were normalized by the standard deviation of the as-grown superlattice material. The normalized standard deviation (NSD) of 1 represents as-grown superlattice, while an NSD of zero indicates complete mixing. For convience, a mixing parameter (MP) was defined as: MP=1-NSD . Based on this definition, an MP of zero corresponds to as-grown material and MP of 1 represents complete mixing.

The mixing effect of RTA-only was estimated along the lines described above. The NSD and MP are shown in Fig.3a as well as PL peak position for same samples measured at 77°K shown in Fig.3b. An anneal of 10s at 950°C resulted in ~25% mixing. A corresponding "blue shift" of PL was 6meV. The level of mixing was found to increase roughly linearly with annealing time at both 950°C and 1000°C, with the latter exhibiting a sharper slope.
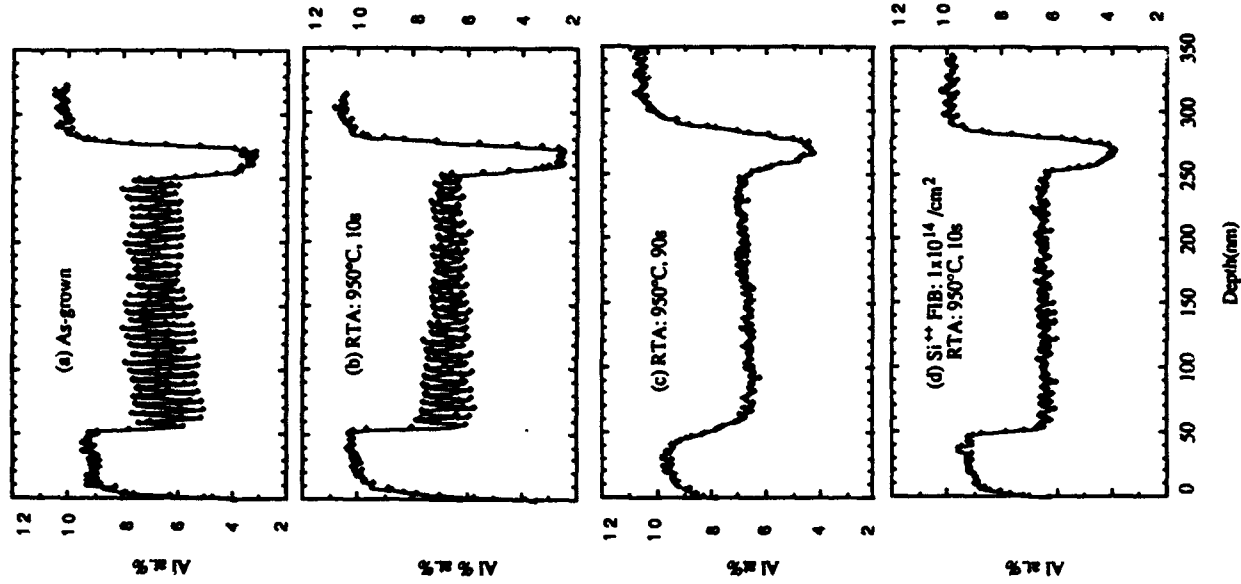
Fig.2 Results of 4.2°K Photoluminescence characterization

(a) RTA: 950°C, 10s

SL

QW

PL Intensity (kcps)

Energy (eV)

(b) Si++ FIB: 1x10^14 cm^-2
RTA: 950°C, 10s

Bulk AlGaAs (Al: 16%)

SL

QW

Fig.1 AES depth profiles of $Al_{0.3}Ga_{0.7}As/GaAs$ superlattice samples after variety of RTA and FIB processing

(a) As-grown

(b) RTA: 950°C, 10s

(c) RTA: 950°C, 90s

(d) Si++ FIB: 1x10^14 /cm^2
RTA: 950°C, 10s

Al at.%

Depth(nm)

The dose dependence of Si FIB-mixing is shown in Fig.4. With low dose of 1×10^{13} cm^{-2}, only a 0.42 mixing parameter was produced. An increase of dose by factor 4 to 4×10^{13} cm^{-2} caused the mixing parameter to increase by 0.36 to 0.78. A dose of 1×10^{14} cm^{-2} induced a mixing parameter of 0.88. This is the lowest ion beam dose necessary for nearly complete mixing reported to date for either FIB or BB implantation. Doubling the dose to 2×10^{14}/cm^2 results in an increase in mixing by only 0.05 to 0.92. Further dose increases produced a diminishing increase in mixing parameter. It is noticed that the dose-NP relation obeys a power law up to a dose of 1×10^{14} cm^{-2}, after which the slope of curve becomes increasingly flat. Although higher dose could produce more complete mixing, the dose of 1×10^{14} cm^{-2} is more suitable for high-resolution device fabrication because it not only produces satisfactory mixing, but also features smaller lateral profile and generates less damage.

Summary and Acknowledgement

In summary, we have investigated Si^{++} FIB-induced mixing of an Al$_{0.3}$Ga$_{0.7}$As/GaAs superlattice structure with a 7 nm period. RTA conditions of 10 sec at 950°C have been determined to remove the ion damage and produce the mixing effect in the implanted regions, while minimizing the purely thermal mixing. A Si^{++} FIB dose of $\sim 10^{14}$ cm^{-2} is sufficient to provide mixing of the superlattice which is close to 90% complete. The combination of short period superlattice structure, low-dose FIB mixing and short-time RTA have great potential for providing a high-resolution technique for optoelectronic device and circuit fabrication.

The authors would like to acknowledge partial support for this work from the Office of Naval Research and the National Science Foundation.

References

[1] J. Kobayashi, M.Nakajima, Y. Bamba, T. Fukunaga, K. Matsui, K. Ishida, H. Nakashima and Koichi Ishida: Jpn J. Appl. Phys.Lett. 25(1986) 385

[2] K. Matsui, J. Kobayashi, T. Fukunaga, Koichi Ishida and H. Nakashima: Jpn J. Appl. Phys. Lett. 25(1986) 651

[3] S. Lee, G. Braunstein, P. Fellinger, K.B. Kahen and G. Rajeswaran: Appl. Phys. Lett. 53(1988) 2531

[4] K. Ishida, E. Miyauchi, T. Morita, T. Takamori, T. Fukunaga, H. Hashimoto: Jpn. J. Appl. Phys. Lett. 26(1987) 285

[5] K. Ishida, K. Matsui, T.Fukunaga, J. Kobayashi, T. Morita and H. Nakashima: Appl. Phys. Lett. 51(1987) 109
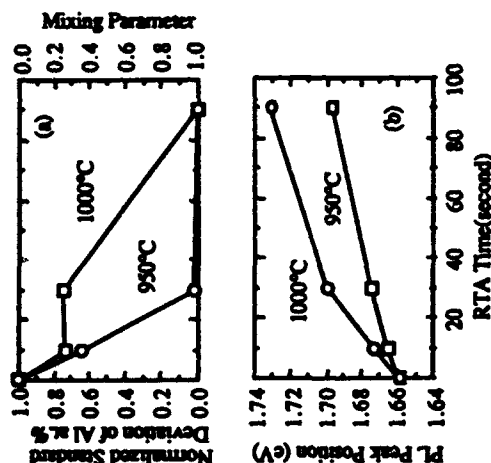
Fig.3 RTA-only mixing effect. (a), Normalized standard deviation and mixing parameter vs RTA conditions. (b) 77°K PL peak position vs RTA conditions.
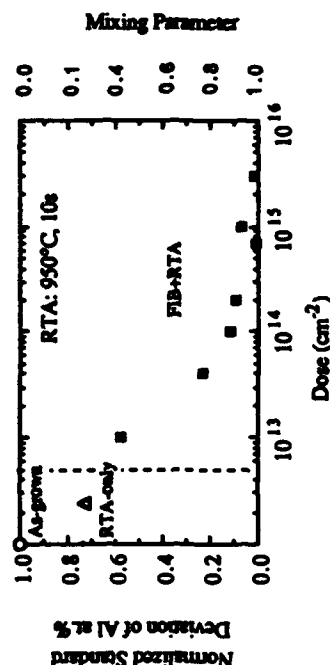

Fig.4 Normalized standard deviation of Al as well as mixing parameter as function of ion dose of Silicon FIB implantation

Monolithically Integrated SQW Laser and HBT Laser Driver Via Selective OMVPE Regrowth

David B. Slater Jr., Paul M. Enquist, James A. Hutchby, Frederick E. Reed, Arthur S. Morris, Robert M. Kolbas, Robert J. Trew, Alexandre S. Lujan, and Jacobus W. Swart

Abstract—An AlGaAs / GaAs Npn HBT laser driver circuit and a pseudomorphic InGaAs / GaAs / AlGaAs graded index SQW laser have been laterally integrated to maintain surface planarity using selective OMVPE regrowth of the HBT. The self-aligned HBT's exhibit a dc current gain of 30 and an f_t (f_{max}) of 45 (60) GHz. The 980 nm lasers exhibit room temperature threshold current densities as low as 420 (320) A / cm^2 for CW (pulsed) operation. The cavities measuring 40 (7) × 500 μm^2 and have less than 1 (2) of series resistance. SPICE simulations of the integrated driver indicate operating speeds over 10 Gb / s are possible.

Introduction

THE majority of optoelectronic research has focused on III-V material structures for discrete devices such as detectors, lasers, modulators, high-speed field effect (FET's) and heterojunction bipolar transistors (HBT's). This research has moved to monolithic integration of the various devices to produce optoelectronic integrated circuits (OEIC's) with greater functionality and speed.

The simplest method of monolithic integration is to produce the photonic device structure epitaxially and produce the electronic devices (FET's) by implantation [1]. Another simple approach is to fabricate photonic and electronic devices from a single epitaxial structure, but this prohibits optimization of the individual structures. A monolithic 9 Gb/s photodiode-HBT receiver with −17.5 dBm sensitivity has been demonstrated using the HBT base-collector for the detector [2]. The thin HBT collector limited the quantum efficiency of the detector diode to 0.35 A/W as compared to a more optimum value of 0.8

A/W resulting in a 3.6 dBm loss of sensitivity. An alternative technique, vertical integration, stacks the epitaxial structures by way of a single growth providing greater flexibility for individual device optimization. Unfortunately, excess surface topography can result which further complicates mesa device processing. This is especially so given that photonic device structures are often several microns thick. Demonstrations employing this technique include a 10 Gb/s p-i-n-HEMT receiver [3] with a sensitivity of −11.7 dBm, a 5 Gb/s p-i-n-HBT receiver with a sensitivity of −18.8 dBm [4], and a laser-HBT transmitter which was operated at 5 Gb/s [5]. To overcome the loss in planarity of this technique, the growth has been done on substrates that were etched to form wells in which the photonic devices were then recessed [1], [6]. The final technique is selective epitaxy which involves multiple growths and allows several devices to be integrated laterally producing a planar surface. This is accomplished by growing the first structure, masking the areas to be preserved with silicon nitride or oxide, etching the surface to a depth equal to the thickness of the next structure to be regrown and subsequently regrowing that structure. Organometallic vapor phase epitaxy (OMVPE) is well suited for this since it can be controlled so that no deposition occurs on the mask. This is in contrast to molecular beam epitaxy, where polycrystalline deposition occurs on the mask and must subsequently be removed. This technique has been used to demonstrate monolithic integration of Npn and Pnp HBT's for various applications [7], [8]. In this paper we report the first monolithic integration via selective OMVPE regrowth of a high quality pseudomorphic InGaAs SQW laser and high speed self-aligned AlGaAs/GaAs HBTs in a laser driver circuit.

Material Growth and Device Fabrication

A cross sectional view of the HBT and laser device structures are given in Fig. 1. The laser structure was grown first which from bottom to top consisted of a 1 μm GaAs cathode contact layer ($n = 2 \times 10^{18}$ cm^{-3}), 50 nm Al$_x$Ga$_{1-x}$As grading ($x = 0$–0.3, $n = 1 \times 10^{18}$ cm^{-3}), 1 μm Al$_{0.3}$Ga$_{0.7}$As cladding ($n = 1 \times 10^{18}$ cm^{-3}), 0.25 μm Al$_x$Ga$_{1-x}$As graded index region ($x = 0.3$–0) which was
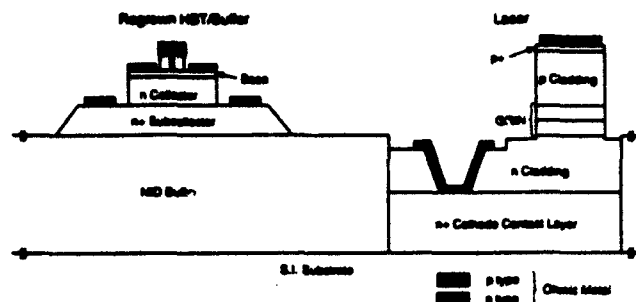
Fig. 1. Cross sectional view of integrated HBT and laser prior to polyimide planarization and interconnect metallization.

Fig. 2. Gummel plot of a two emitter $(2.6 \times 5 \ \mu m^2)$ and one base contact HBT.

not intentionally doped (NID), single 10 nm $In_{.18}Ga_{.82}As$ strained quantum well (NID), 0.25 μm $Al_xGa_{1-x}As$ graded index region $(x = 0-0.3, NID)$, 1 μm $Al_{0.3}Ga_{0.7}As$ cladding $(p = 1 \times 10^{18} \ cm^{-3})$, 50 nm $Al_xGa_{1-x}As$ grading $(x = 0.3-0, p = 1 \times 10^{18} \ cm^{-3})$ and a 50 nm GaAs anode contact layer $(p = 6 \times 10^{19} \ cm^{-3})$. The second growth consisted of a 2 μm NID buffer $(n < 10^{15})$ and the HBT structure. The HBT structure consisted of a 0.6 μm thick GaAs subcollector $(n = 2 \times 10^{18} \ cm^{-3})$, 0.6 μm GaAs collector $(n = 2 \times 10^{16} \ cm^{-3})$, 90 nm GaAs base $(p = 3 \times 10^{19} \ cm^{-3})$, 40 nm Al_3Ga_7As emitter $(n = 5 \times 10^{17} \ cm^{-3})$, 30 nm $Al_xGa_{1-x}As$ grading $(x = 0.3-0, n = 1 \times 10^{18} \ cm^{-3})$ and a 0.25 μm GaAs emitter contact layer $(n = 2 \times 10^{18} \ cm^{-3})$.

Standard optical contact lithography and liftoff metallizations were used. The lasers were located 150 μm from the HBT's. N-type (p-type) onmics were formed by evaporating AuGe/Ni/Au (Ti/Pt/Au). The HBT self-aligned base and laser anode contacts were formed simultaneously, as were the HBT collector and laser cathode contacts. Ti/Au interconnects were deposited over a planarizing polymide layer. The wafer was thinned, and the die were cleaved to form a 500 μm Fabry–Perot cavity.

HBT AND LASER PERFORMANCE

Discrete Npn HBT's located adjacent to the laser-driver circuits were tested to determine their dc and microwave characteristics. Their performance was comparable to Npn HBT's fabricated on SI substrates using the same epitaxial structure used in developing SPICE models. The HBT geometry used throughout the circuit has two emitters $(2.6 \times 5 \ \mu m^2)$, a single self-aligned base contact and a base mesa area of 68 μm^2. The value of f_t (f_{max}) for this geometry was 45 (60) GHz. at a collector-emitter bias of 2 Volts and an emitter current density of $4 \times 10^4 \ A/cm^2$ (11 mA). A typical Gummel Plot is shown in Fig. 2. A typical value of dc current gain was 30 at an emitter current density over $1 \times 10^4 \ A/cm^2$. The base (collector) current ideality factor is 1.3 (1.0) above unity gain indicating the recombination component of the base current is low.

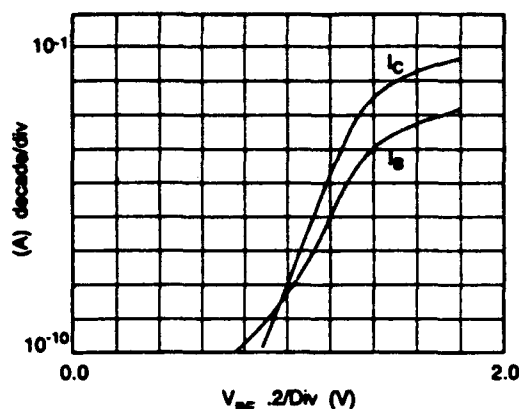High quality pseudomorphic InGaAs/GaAs/AlGaAs graded index single quantum well (PGRINSQW) lasers

were fabricated with 7 and 40 μm wide active areas. Room temperature CW operation of the 40 μm wide laser exhibited single mode emission at a threshold current density, J_{th}, of 420 A/cm^2 and a $J_{th} = 320 \ A/cm^2$ when pulsed. The room temperature CW emission spectra of a 7 μm wide laser is shown in Fig. 3. The measurement was obtained by probing the laser directly thus bypassing the circuitry. The emission is nearly single mode (9733 Å) at 1 mA above threshold (27 mA). The CW optical output power (relative) versus input current is shown in the insert of Fig. 3 for the same device. The average threshold current for the devices tested was 27 mA with the lowest at 25.5 mA. In pulsed mode the threshold current dropped as low as 22 mA. The series resistence of the 7 μm integrated diodes was very low (1–2 Ω).

CIRCUIT PERFORMANCE

A schematic of the circuit containing 26 transistors and a photomicrograph are given in Fig. 4(a) and (b), respectively. Due to the low series resistance of the laser, the circuit is capable of operating with a V_{EE} of -5.2 V. The circuit is immune to stray inductances in either the ground or $-V_{EE}$ leads as a result of layout and topology. The biasing is performed by current sources throughout, and the connections to ground for the circuit and the anode of the laser come from a common pad on the die, and thus eliminate dynamic currents in the supply leads. The anode is connected to this common pad by a crossover in the center of the laser as shown in the micrograph. Separate ground connections for the circuit and the laser anode (i.e., [6]) reduce the high frequency advantages of the differential (current steering) topology. The current source biasing provides a wide common mode range for the input. The I_{bias} current mirror sets the dc operating point of the laser, and the I_{mod} mirror sets the modulation current up to 40 mA each.

Circuits were functionally tested with a dc laser current of 25 mA via I_{bias} (threshold for a 7 μm wide stripe) and with a modulation current of 25 mA. A 10 MHz sinewave was applied to the input and the optical output was
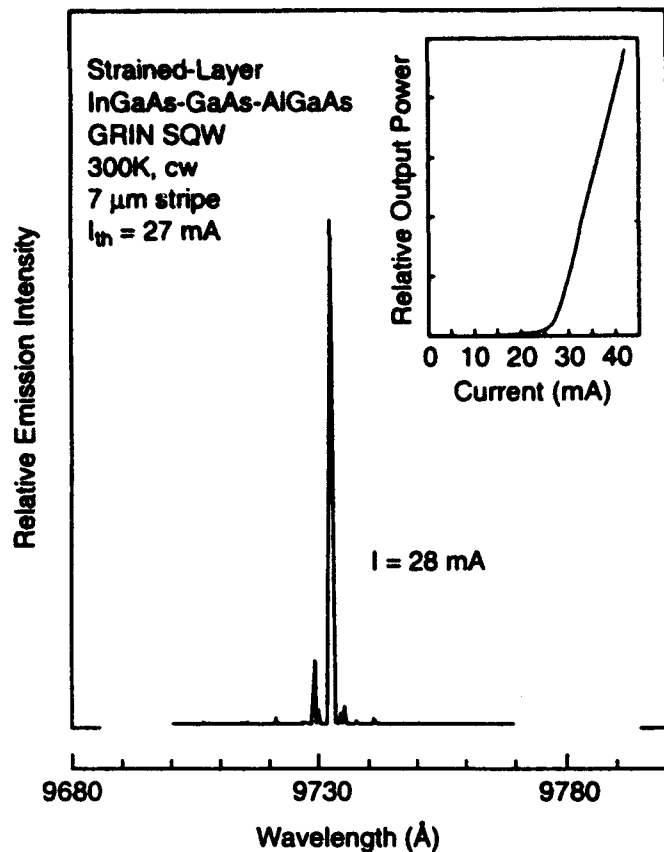
Fig. 3. Spectral plot of relative emission intensity versus wavelength for integrated laser diode and (insert) relative output power versus current.
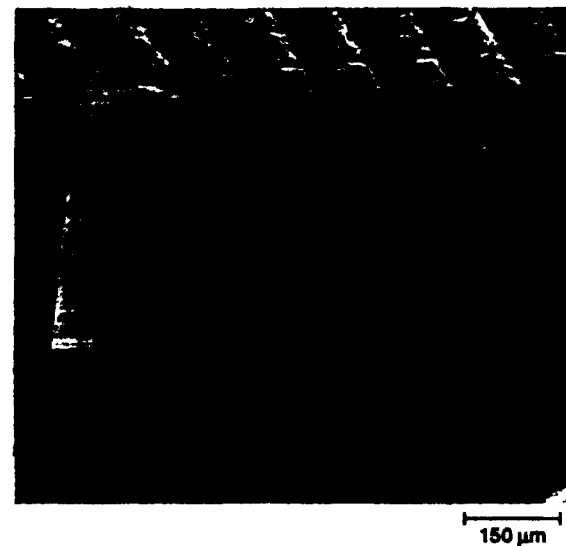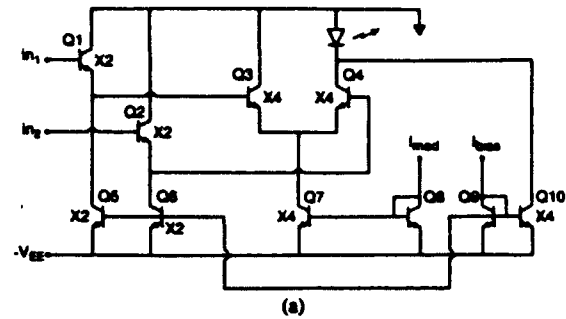

Fig. 4. (a) Schematic of integrated laser driver. (b) SEM photomicrograph of the die with laser (left) and HBT driver (right) measuring $500 \times 850 \ \mu m^2$.

detected using a Si photodiode/transimpedance amplifier and an oscilloscope. Performance tests at high frequencies are limited by the 5 MHz bandwidth of the detector.

Using extracted parameters for the HBT and laser, SPICE simulations were performed to estimate the rise/fall (10–90%) times of the voltage drop across the laser which was modeled as a simple diode with a series resistance of 1.5 Ω and a zero bias junction capacitance of 4 pF. The simulated times for modulation currents of 10 or 30 mA and dc laser bias currents of 10 to 40 mA are given in Fig. 5. Small signal simulations in this same range of operation indicate a minimum bandwidth > 11 GHz. These simulations indicate the circuit has potential for operation above 10 Gb/s. Key factors in obtaining this are the low series diode resistance (low voltage gain) and the small base-collector capacitance of the driver, $Q4$. These factors reduce the impact of Miller multiplication without sacrificing the current sinking capacity of the driver, hence the use of HBT's with two emitters and a single base contact.

Note that the above performance was obtained without considering the relaxation oscillation frequency (f_r) limit which is estimated to be less than 6 GHz [9] for these lasers. Consequently, the speed of the laser would limit the large signal performance of the integrated HBT/laser transmitter. This integration technique could be used to
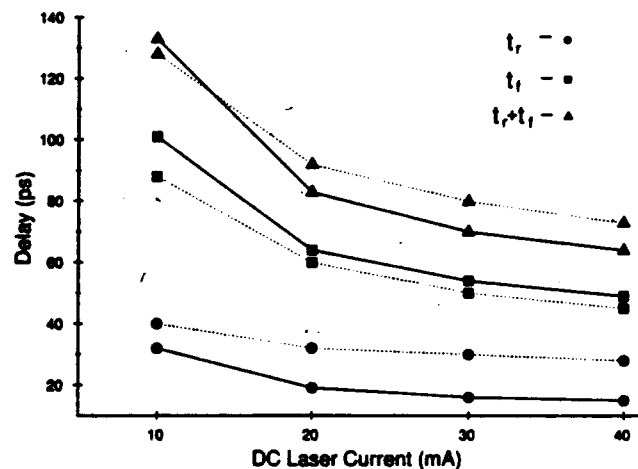

Fig. 5. Plot of rise, fall and total delay times for 10 (30) mA of modulation current versus dc bias current given by the solid (dashed) lines.

combine HBT drivers with low resistance surface emitting lasers that exhibit high f_r, and thus are capable of 10 Gb/s operation [10]. Furthermore, this technique can then be used to realize compact 2-D arrays for aggregate data transmission rates on the order of a Tb/s.

SUMMARY

Monolithic integration of a InGaAs/GaAs/AlGaAs PGRINSQW and an AlGaAs/GaAs HBT driver circuit has been demonstrated using selective OMVPE regrowth. The laser exhibited a low $J_{th} = 420$ (320) A/cm^2 at room temperature in CW (pulsed) mode. This method of integrating dissimilar devices has the distinct advantage of allowing several epitaxial structures to be optimized individually while maintaining a relatively planar surface. Based on circuit simulations, the driver circuit is capable of operating at speeds above 10 Gb/s. This excellent performance is attributed to the low series resistance (1–2 Ω) of the laser, and f_t and f_{max} of the HBT's and low parasitic base-collector capacitance. The integration of 26 high speed HBT's in close proximity to the low threshold laser diode via selective OMVPE represents a substantial improvement in integration density and potential bit rate for monolithic OEIC's.

REFERENCES

[1] R. M. Kolbas, J. Abrokwah, J. K. Carney, D. H. Bradshaw, B. R. Elmer, and J. R. Biard, "Planar monolithic integration of a photodiode and a GaAs preamplifier," *Appl. Phys. Lett.*, vol. 43, pp. 821–823, 1983.

[2] K. D. Pedrotti, R. L. Pierson Jr., R. B. Nubling, C. W. Farley, E. A. Sovero, and M. F. Chang, "Ultra-high-speed PIN/HBT monolithic OEIC photoreceiver," *IEEE Device Res. Conf.*, 1991.

[3] Y. Akahori, Y. Akatsu, A. Kohzen, and J. Yoshida, "10-Gb/s high-speed monolithically integrated photoreceiver using InGaAs p-i-n PD and planar doped InAlAs/InGaAs HEMTs," *IEEE Photon. Technol. Lett.*, vol. 4, pp. 754–756, 1992.

[4] S. Chandrasekhar, A. H. Gnauck, W. T. Tsang, F. S. Choa, and G. J. Qua, "A monolithic 5 Gb/s p-i-n/HBT integrated photoreceiver circuit realized from chemical beam epitaxial material," *IEEE Photon. Technol. Lett.*, vol. 3, pp. 823–825, 1991.

[5] K.-Y. Liou, S. Chandrasekhar, A. G. Dentai, E. C. Burrows, G. J. Qua, C. H. Joyner, and C. A. Burrus, "A 5 Gb/s monolithically integrated transmitter with 1.5 μm multiple quantum well laser and HBT driver circuit," *IEEE Photon. Technol. Lett.*, vol. 3, pp. 928–930, 1991.

[6] W. P. Hong, G. K. Chang, R. Bhatt, J. L. Gimlett, C. K. Nguyen, G. Sasaki, and M. Koza, "High performance $Al_{0.48}In_{0.52}As/Ga_{0.47}In_{0.53}As$ MSM-HEMT receiver OEIC grown by MOCVD on patterned InP substrates," *Electron. Lett.*, vol. 25, pp. 1561–1563, 1989.

[7] P. M. Enquist, D. B. Slater Jr., and J. W. Swart, "Complementary AlGaAs/GaAs HBT I^2L (CHI^{2}L) technology," *IEEE Electron Dev. Lett.*, vol. 13, pp. 180–182, 1992.

[8] D. B. Slater Jr., P. M. Enquist, J. A. Hutchby, A. S. Morris, and R. J. Trew, "Phase matched AlGaAs/GaAs complementary HBTs for push-pull operation," *Electron. Lett.*, vol. 28, pp. 1615–1616, 1992.

[9] S. D. Offsey, W. J. Schaff, L. F. Lester, and L. F. Eastman, "Comparison of single and multiple quantum well strained layer In/Ga/As/GaAs/AlGaAs laser grown by molecular beam epitaxy," in *Proc. Inst. Phys. Conf. Ser.*, vol. 112, pp. 551–554, 1990.

[10] J. Lin, J. K. Gamelin, K. Y. Lau, S. Wang, M. Hong, and J. P. Mannaerts, "Ultrafast (up to 39 GHz) relaxation oscillation of vertical cavity surface emitting laser," *Appl. Phys. Lett.*, vol. 60, pp. 15–17, 1992.